X-ray fluorescence for the determination of gold in vivo

Shakeshaft, John Thomas

Award date:
1992

Awarding institution:
University of Bath

X-RAY FLUORESCENCE FOR THE DETERMINATION OF GOLD *IN VIVO*

Submitted by John Thomas Shakeshaft for the degree
of PhD of the University of Bath 1992

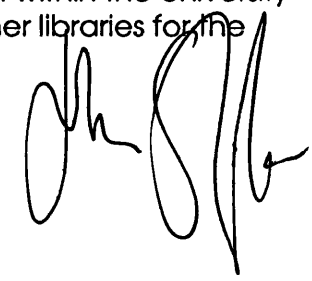

ProQuest LLC
789 East Eisenhower Parkway
P.O. Box 1346
Ann Arbor, MI 48106-1346

Summary

Gold salts have been used in the treatment of rheumatoid arthritis since the early part of this century, and are still in routine use in many centres, although their mode of action is still not fully understood. However it is well established that gold salts are nephrotoxic, which limits their use in the treatment of rheumatoid arthritis. Consequently it is of interest both to researchers in the field of rhuematoid arthritis and to rheumatologists to be able to measure the concentration of gold in various tissues and organs (for example kidneys) of patients who are receiving chrysotherapy, and a technique allowing quantitative measurements of gold *in vivo*, thus eliminating the need for traumatic biopsies would be of value.

After a review of some relevant clinical history of gold, and of some of the other techniques available that have been used for the monitoring of trace elements *in vivo*, the feasibility of using X-ray fluorescence analysis for the determination of gold *in vivo* is considered in detail. The features that occur in a typical spectrum are first discussed, followed by an overview of the factors that will effect the detection limit of gold in a clinical system.

A number of radiation sources are considered in detail, including radio-isotope sources and X-ray generators. The feasibility of using different source/detector geometries and sources both inside and outside the body are considered for the radio-isotope sources.

A Monte Carlo computer model was constructed, and is described, to help predict how sensitivity will vary both with kidney position, and within the kidney itself. The results of the latter study leading to the conclusion that the results from a clinical X-ray fluorescence system need interpreting with some caution.

A filtered ^{153}Gd source was chosen as the system best suited to the local circumstances, and a prototype clinical system was constructed. The gold

content of the right kidney of a number of patients, with widely varying clinical histories, was determined using this system, and the results are presented to demonstrate the effectiveness of the system.

Contents

Acknowledgements

ἀργύριον καὶ χρυσίον οὐχ ὑπάρχει
μοι· ὃ δὲ ἔχω τουτό σοι δίδωμι·

The work contained in this thesis has been financially supported by the UK Medical Research Council, and the Royal United Hospital NHS Trust, Bath, UK. This support is gratefully acknowledged.

My supervisors, Prof SC Lillicrap and Dr RAL Sullivan, played an important rôle in this work, as in any PhD project, and I would like thank them for it. My special thanks go to Prof Lillicrap for many thought provoking conversations, and for providing a department with such a congenial atmosphere to work in.

I must also thank Dr AK Clarke (Consultant Rheumatologist, RNHRD, Bath) and Dr CL Hall (Consultant Nephrologist, RUH, Bath) for referring their patients to us. The clinical measurements would not have been possible without the help of Dr FA Duck (Medical Physics, RUH, Bath), who provided help and tuition for the ultrasound depth determination used to locate the kidney. Thanks for the construction of the prototype clinical system, and all the collimators goes to Mr S Adams.

My thanks also go to Dr SM Smith, Mr R Price and Mr J Scott, for copious notes and advice in the early days explaining how to use the equipment, and what some of the pitfalls were. The work described in chapter 6 would not have been possible without the help and tolerance of Mr M Evans and the staff of the Nuclear Medicine department at the the RUH, Bath.

Finally I would like to express my appreciation to the Medical Physics department at the RUH for many useful conversations, tireless advice and putting up with me for the last three years! So thanks to Carol, David, Francis, Geraldine, Hazel, Helen, Joyce, Lindsay, Martyn, Mike, Peter, Richard, Suzanne and Steve.

Symbols

A	Activity
$\tilde{A}$	Accumulated activity
c	Speed of light *in vacuo*
D	Absorbed dose
D_0	Absorbed dose threshold
d	Denominator
E	Energy
e	Elementary charge
F	Fano factor
G	A fraction (has a value between 0 and 1)
g	A fraction (has a value between 0 and 1)
H	Dose equivalent
H_E	Effective dose
H_T	Equivalent dose
I	Intensity
i	Summing index
j	Summing index
m_e	Rest mass of electron
N	Number of counts
N_P	Number of counts in peak
N_B	Number of counts in background under peak
N_0	$N_P + N_B$
n	Number of photons per disintegration
P	Number of decays
p	Distance
Q	Kinetic energy
q	Distance
R	Radius
r	Radius
r_0	Classical radius of electron
S	Absorbed dose per unit activity
T	A fixed time period
$T_{1/2}$	Half life
t	Time
W_t	Full Width Half Maximum
W_y	Contribution of component y to FWHM
w_R	Radiation weighting factor (w_R=1 for γ-radiation and X-rays)
w_T	Tissue weighting factor
x	Distance
Z	Atomic number
α	Photon energy divided by rest mass energy of electron
β	Angle
Γ	Dose rate constant
δ	Small quantity
ε	Energy required to generate electron hole pair
η	Ratio of intensities

θ	Angle
Λ	Decay constant
λ	Wavelength
μ	Mass attenuation coefficient
μ_E	Energy attenuation coefficient
ρ	Density
σ	Scattering cross-section
Φ	Sensitivity
ϕ	Angle
Ψ	Fading factor
Ω	Solid angle

Preface

ICRP Publication 60

1990 saw the publication of ICRP publication 60 (ICRP, 1990), which contains recommendations of the international commission regarding radiation protection, following a re-analysis of the data from Hiroshima and Nagasaki bombs. The contents of the document have a direct bearing on the results and conclusions of this project, particularly when considering dose calculations.

Therefore, the decision had to be made whether to ignore the contents of this document or take them into account. The decision that was made, was generally to adopt the recommendations contained in this report, since in due course they are likely to become statuatory. However it was not possible to re-analyse all the work that had already been done. The approach that has been adopted with regard to various recommendations is considered in the following paragraphs.

New terms

The commission recommended that the term "effective dose equivalent" should be dropped, and the term "effective dose" be substituted. This has been adopted throughout the thesis. Also the term equivalent dose has been (re)introduced to replace the term "weighted absorbed dose". The radiation quality factor, Q, now becomes radiation weighting factor, w_R.

New radiation weighting factors

The commission recommended that a new set of radiation weighting factors, w_R, (used in calculating equivalent dose, H_T) should be adopted. These have been adopted throughout the thesis. In fact for gamma rays and X-rays this factor remained unchanged at unity.

New tissue weighting factors

The commission recommended that a new set of tissue weighting factors, w_T,

(used in calculating effective dose, H_E) should be adopted. These have been adopted throughout the thesis. Of particular relevance has been the introduction of separate weighting factor for skin (0.01) and the revision of the way "other" organs are handled. Skin dose: In early work skin dose had been considered as the limiting factor, since the following paragraph from the Ionising Radiation Regulations (1985) was interpreted as meaning that skin should be averaged over the area irradiated rather the area of the whole skin surface: *"In assessing the dose quantity to skin whether from contamination or external radiation, the area of skin over which the dose quantity is averaged shall be appropriate to the circumstances but in any event shall not exceed 100cm^2."* However the report by the international commission clearly states that: *"For stochastic effects the equivalent dose can be averaged over the whole skin."* It is stochastic effects that we will always be concerned with, since we are not giving a dose sufficient to cause deterministic effects (0.5Sv y^{-1}).

Therefore the early conclusions drawn on the basis of skin dose are obviously, at least to some extent flawed. However since kidney absorbed dose now becomes the major contribution to effective dose, and for a fixed geometry the absorbed dose to the kidney is related to the skin absorbed dose, this early discussion has been retained.

Chapter 1

Introduction

The reader's attention is drawn to the glossary in Appendix C where many of the clinical terms and abbreviations used in the text of this chapter are defined.

1.1 Clinical History of Gold

Gold has been employed as a panacea for all diseases throughout recorded time: Since the Chinese used gold medicinally (Block and van Goor, 1956) gold has been used as a treatment at various points throughout history, for example, the alchemists attempted to prepare 'an elixir of life' from gold to cure all ills and confer eternal youth. For centuries gold was used as an anti-pruritic. However untoward reactions were reported (Virgil, 19 BC).

Interest in the use of gold as a medicine more recently was initiated by Robert Koch, who observed gold cyanide arrested the growth of tubercle bacilli *in vitro*. However he was unable to demonstrate this effect in infected animals. Despite this gold began to be used for the treatment of tuberculosis and was extended to the treatment of arthritis, as some clinicians around the turn of century believed rheumatoid arthritis to be a tubercular joint disease. At the present time gold salts are employed widely in the treatment of rheumatoid arthritis.

There are two common modes of administration of gold: Either parenterally as aurothiomalate or aurothioglucose, or orally as auranofin. The former is preferred by clinicians as it is administered under controlled conditions. (Auranofin, which is taken in tablet form, by the patient has side effects such as mild diarrhoea, which has led to the patient not taking the whole of the prescribed dose.) A new method of treatment using a new form of gold, gold yeast, has been reported by Vinson (1990). It is claimed that, in rat models, this treatment has shown to be effective with no toxicity. This work, as all work on animals, involves an induced form of rheumatoid arthritis as the disease only

occurs in humans. This model of the disease is usually achieved by injection of mycobacterium or sodium urate into one of the limbs of the animal. The inflammation caused is then thought to be a good model of the symptoms of rheumatoid arthritis.

The use of gold based drugs to treat rheumatoid arthritis is an effective widespread treatment. It has an anti-inflammatory action, but the ability of gold to halt erosive changes in bone has not been proved. However the treatment, using commercially available drugs, although effective is not without side effects, some of which are discussed in the section 1.3. Gold also has some other medical applications including: use in dental alloys; as radioactive isotopes in cancer treatment; as gold leaf for neurosurgical procedures; and for accelerated healing of cutaneous ulcers, however the use of gold as an anti-arthritic drug is by far its most widespread use.

1.2 Mode and Site of Action of Gold

Despite its widespread use, the mode of action of gold is still unclear (Bacon and Salmon, 1987). It is known that, *in vivo*, sodium aurothiomalate (the most common form of gold) rapidly dissociates to form the gold moiety, which becomes strongly protein bound. This binding has been estimated to be around 90% by Mascarenhas *et al* (1972). The molecule is taken up in macrophages and is selectively concentrated in the inflamed synovium (Vernon-Roberts *et al*, 1976); it is this effect which may well account for the action of the drug.

There has been some speculation as to whether the effect of the gold salt is due to the thiol group in the drug. Clinical evidence in support of the importance of thiol groups for anti-rheumatic activity was found by Jellum *et al* (1980) who administered aurothiomalate labelled with the radio-isotopes ^{195}Au and ^{14}C to mice. The authors demonstrated that both groups had anti-rheumatic activity.

The site of action of the slow acting rheumatic drugs is also still unclear (Bacon and Salmon, 1987). Within the synovium, it is known that gold is deposited in

monocyte/macrophage cells, which indicates that the drug may have a direct effect at this site; but evidence for this is still thin.

1.3 Toxicities of Gold

Toxic side effects from gold treatment occur in approximately a third of patients. These effects are varied and include: exfoliative dermatitis; eosinophilia; thrombocytopenia; agranulocytosis and aplastic anaemia; jaundice; lung changes and proteinuria (Collins, 1987). Fatalities from gold treatment however are rare, although it has been suggested by Girdwood (1974) that deaths per number of prescriptions exceed that of any other drug. However, more recently, it was concluded by Lehtinen and Isomäki (1991) that large cumulative amounts of gold was not associated with premature death. The authors concluded that "the best way to prevent premature death is probably to treat RA effectively. Though the drugs have serious side effects, the benefits may outweigh the disadvantages."

The most widely documented side effect of gold treatment is proteinuria (signifying renal damage), this occurs in 2-20% patients treated (Hall and Tighe, 1989) and occurs anytime between two weeks and six years after commencement of treatment, of these cases 10-30% have nephrotic syndrome. However proteinuria eventually resolved in all patients studied by Hall *et al* (1987) after discontinuation of gold therapy. It has also been reported by Silverberg *et al* (1970) that the severity and duration of proteinuria is not related to total gold administered, duration of treatment, the peak or mean serum gold levels or urinary gold excretion. However the fact that eventually proteinuria resolves in all patients has reassured clinicians: To quote Collins (1987): 'These new findings, which suggest a "sitting on hands approach" to proteinuria caused by gold while nature effects a cure, are reassuring'. Nevertheless it would be advantageous to develop a simple technique that could predict the onset of proteinuria, thus allowing renal failure to be prevented.

Chrysiasis, another side effect of gold therapy, is a rare, long-lasting or permanent pigmentation of the skin brought about by the parenteral administration of gold preparations, and subsequent exposure of the skin to ultraviolet radiation (Schmidt, 1941). The chrysiasis is not in itself a problem, except that it is usually accompanied by dermatitis. Jeffrey *et al* (1975) studied skin gold levels in both chrysiasis and non-chrysiasis patients. The findings of this group were that in chrysiasis patients there was no correlation between dose rate and skin gold levels, however in non-chrysiasis patients the skin gold levels were proportional to the current dose rate. The other side effects of gold therapy are less well documented in the literature except that it has been reported that all patients undergoing treatment with gold eventually develop dermatitis with or without chrysiasis.

1.4 Aim of this project

Despite the fact that proteinuria eventually resolves itself in all patients, it would be useful to develop a non invasive technique that could measure the gold build up in the kidney and to try and relate this to the onset of proteinuria, in order to predict and prevent the onset of proteinuria. To this end this project was undertaken. The availability of data on gold levels in the kidney is limited to three sets of results taken by Gottlieb *et al* (1972), Vernon-Roberts *et al* (1976) and Bascó *et al* (1988) from seven cadavers, undergoing gold therapy at the time of death. The samples of kidney tissue from these cadavers had gold concentrations between 45 and 175μg gold (g kidney tissue)$^{-1}$. From these figures it was concluded that any technique must be able detect concentrations of gold in the kidney at least as low as 40μg gold (g kidney tissue)$^{-1}$. The technique used must also be specific to gold in the kidney as Gottlieb *et al* also found similar or greater concentrations of gold in many other parts of the body, as shown in table 1.4.1.

1.5 Possible measurement techniques

When measurements of potentially toxic trace elements are to be made *in vivo*,

Specimen	μg Gold (g wet tissue)$^{-1}$	
Lymph node	391	211
Liver	125	126
Bone Marrow (Sternal)	81	
Spleen	77	
Synovium	32	
Bone (Cortical Sternal)	38	
Muscle (Quadriceps)	7	
Cartilage (Knee)	5	
Adrenal	239	
Muscle (Gluteus)	95	211
Renal Cortex	129	
Skin (Dernatitis, Forearm)	79	
Renal Medulla	64	
Thyroid	41	
Skin (Normal, Forearm)	38	
Ovary	23	21

Table 1.4.1 - Gold levels found in a cadaver of a Rheumatoid Arthritic by Gottlieb *et al*

the usual constraints of keeping any radiation dose as low as possible, and the non-standard, extended shape of humans, are compounded by the fact that the target element is present, by definition, only in small quantities. The initial developments all used neutron activation analysis, in one form or another, as the basis of the analytical method. However the use of X-ray fluorescence is now increasingly widespread, and a few other distinct techniques have been reported for particular elements; such as γ-resonance scattering for iron overload (Wielopolski *et al*, 1985). Cadmium, lead and platinum are three trace elements which have been most extensively studied, and a summary of techniques employed is given in the following sections.

1.5.1 Lead

Lead normally accumulates in bone and is therefore an archetypically high atomic number (Z) element embedded in a much lower Z matrix, lending itself to *in vivo* X-ray fluorescence. Three basic types of systems have been used for *in vivo* human studies, one based on the measurement of L X-rays (Wielopolski *et al*, 1989), the other two using K-rays, but with different γ-ray sources and

different source-detector geometries (Ahlgren and Mattsson, 1979; Somervaille *et al*, 1985; Price *et al*, 1984). For *in vivo* measurements of bone lead it seems that a K X-ray measurement of tibia lead using ^{109}Cd is now the method of choice to meet the commonly identified need in toxicological research for an indicator of cumulative internal lead dose (Landrigan, 1989).

1.5.2 Cadmium

Cadmium has been measured *in vivo* by neutron activation, in which prompt γ-rays are monitored, or by X-ray fluorescence. The first *in vivo* X-ray fluorescence systems used 59keV γ-rays from an ^{241}Am source (Ahlgren and Mattsson, 1981), a significant improvement was achieved by using the polarized output of an X-ray generator as the excitation source (Christoffersson and Mattsson, 1983). An important feature of these techniques, however, is the very rapid variation of signal strength with depth in tissue, due to the relatively low energy of the cadmium fluorescence photons (25keV).

Cadmium is measurable by neutron activation analysis largely because the 12% abundant isotope, ^{113}Cd, has an exceptionally high probability (20 000 barns) for capture of thermal neutrons; the effective average cross section for the element is about 2500barns. The prominent prompt γ-ray, at 559keV, is detected in high resolution solid state spectrometers; counting takes place simultaneously with neutron irradiation. Both ^{238}Pu-Be and ^{252}Cf neutron sources have been reported, although ^{252}Cf is the preferred source because of its lower mean energy neutrons.

1.5.3 Platinum

In vivo measurements of platinum are designed to assist in the study of the pharmacokinetics of platinum containing drugs, used in the treatment of various cancers. As the side effects of these drugs include nephrotoxicity, measurements are made in the kidney as well as the tumour site. A detailed description of an X-ray fluorescence system based on a filtered and polarized

X-ray generator has been described by Jonson *et al* (1988). An X-ray fluorescence system to measure both lead and platinum simultaneously has also been described by Todd (1989), following the report of unexpectedly high levels of lead in the kidneys, of patients undergoing cis-platin chemotherapy, by El-Sharkawi *et al* (1986).

1.5.4 Other elements

Another element that has been investigated is mercury (Bloch and Shapiro, 1981). The motivation behind this was the determination of the mercury burdens of dentists, who had used mercury based amalgam. More recently a feasibility study was carried out by Scott and Lillicrap (1988) into whether X-ray fluorescence could be used for gold. The results of this study looked very promising and therefore work has been continued.

1.6 Description of Technique

The technique of X-ray fluorescence involves irradiating a sample with X-rays or gamma photons and recording the resultant spectra. These spectra contain peaks which are characteristic of each element present and the magnitude of these peaks is then related to the amount of the element present. (The details of this are discussed in later chapters.)

The apparatus for this project consisted of various radiation sources which were used to irradiate phantoms representing the gold containing kidney (represented by bottles containing a solution of chloroauric acid) and other body tissue (represented by water). In the first studies, the resultant spectra were recorded using an EG&G Ortec hyper-pure germanium detector (Model Nº 1113-10205) which was 10mm in diameter and 7mm thick. This was biased to -1000V (as specified in the data sheet supplied with the detector) using an EG&G Ortec 459 bias supply and connected via EG&G Ortec 572 amplifier to an EG&G Ortec Multi Channel Analyser. Pulse pile up rejection was always used following the results of Chettle *et al* (1989). Initial settings on the

amplifier were: Pulse shape timing of 6μs; coarse gain of 200; and fine gain of 0.6. This system gave a peak resolution of 500eV (FWHM) at 122keV. A schematic diagram of system inter-connections is shown in figure 1.6.1.

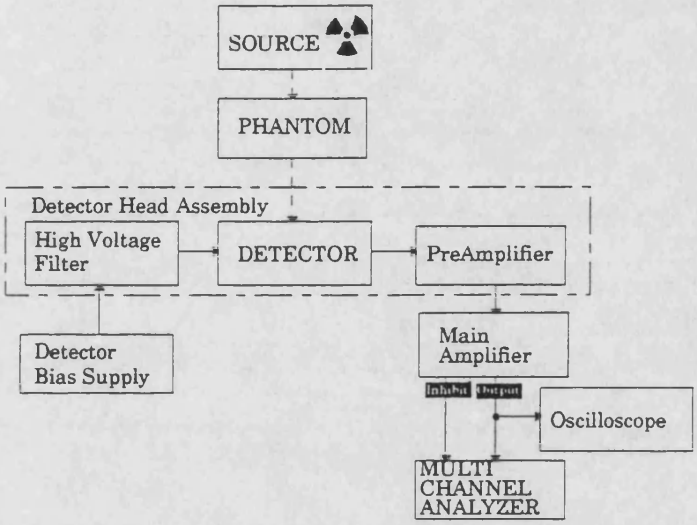

Figure 1.6.1 - Block diagram of apparatus

1.7 Conclusions

It is concluded from the above review that it would be useful to develop a technique that can detect levels of gold in the kidney down to at least 40μg gold (g tissue)$^{-1}$, in order to study the relationship between the gold content of the kidney and the onset of proteinuria. It seems as though X-ray fluorescence would be a suitable technique to do this *in vivo*. In order to obtain maximum sensitivity it is important to understand all the features in the recorded spectrum, and to optimize the detection system to produce the maximum signal to noise ratio.

Chapter 2

Spectral Composition

2.1 Introduction

In the spectrum of number of counts at each energy, it is important to understand where all the features come from so that we may minimise those components which are undesirable, and be aware of those which are inherent to the chosen experimental arrangement.

2.2 Interactions of X-rays with matter

X-rays undergo four types of interaction with matter:

- Inelastic or Compton scattering
- Absorption by the photoelectric effect
- Elastic scattering
- Absorption by pair production

Of these only the first three occur at photon energies up to 1MeV. Therefore it is these three processes that are responsible for the features seen in the recorded spectra.

2.2.1 Compton scattering

In the Compton effect, an incoming photon imparts momentum to an initially bound electron. By consideration of conservation laws, it is clear that the momentum of the photon is reduced after the interaction. By consideration of an initially free electron at rest, it is possible to deduce the energy of the scattered photon at any particular chosen angle. Conservation of both energy and momentum give the following change in wavelength, $\Delta\lambda$, to the incoming photon:

$$\Delta\lambda = \frac{h}{m_e c(1 - \cos\theta)} \tag{2.2.1}$$

Where h is Planck's constant, m_e the rest mass of an electron, c the speed of light, and θ the angle of scatter. This can be rearranged into the following form:

$$E = \frac{E_0}{1 + \frac{E_0}{m_e c^2}(1 - \cos\theta)} \tag{2.2.2}$$

Where E is the energy of the scattered photon, when observed at a scattering angle θ, and E_0 is the energy of the incident photon. It is therefore seen that the Compton effect is independent of atomic number (to a good approximation)..

The directional distribution of photons removed from the incident beam, is described by the differential collision cross-section ($d\sigma$), evaluated as a probability per electron and expressed by the number of scattered photons found in an element of solid angle ($d\Omega$) at a mean scattering angle of θ.

For unpolarized incident photons:

$$d\sigma = \frac{r_0^2}{2}\left(\frac{1}{(1 + \alpha(1 - \cos\theta))^2}\left(1 + \cos^2\theta + \frac{\alpha^2(1 - \cos\theta)^2}{1 + \alpha(1 - \cos\theta)}\right)\right) d\Omega \tag{2.2.3}$$

(Klein-Nishina approximation)

where

$$\alpha = \frac{E}{m_e c^2} \tag{2.2.4}$$

and

$$r_0 = \frac{e^2}{4\pi\varepsilon_0 m_e c^2} \tag{2.2.5}$$

r_0 is known as the 'classical' radius of the electron.

Equation 2.2.3 can also be written in the following form:

$$d\sigma = \frac{r_0^2}{4}\left(\frac{E}{E_0}\right)^2\left(\frac{E_0}{E}+\frac{E}{E_0}-2+4\cos^2\theta\right)d\Omega \qquad (2.2.6)$$

A similar equation also exists for polarised photons:

$$d\sigma = \frac{r_0^2}{2}\left(\frac{E}{E_0}\right)^2\left(\frac{E_0}{E}+\frac{E}{E_0}-2\sin^2\theta\cos^2\beta\right)d\Omega \qquad (2.2.7)$$

where β is the angle between the plane of polarisation of the incoming photons and the scattering plane. From this it can be seen that the flux of Compton scattered photons can be significantly reduced by using polarised photons such that $\sin^2\theta\cos^2\beta$ is maximised. i.e. By setting θ=90°.

The directional distribution of unpolarized Compton scattered photons for

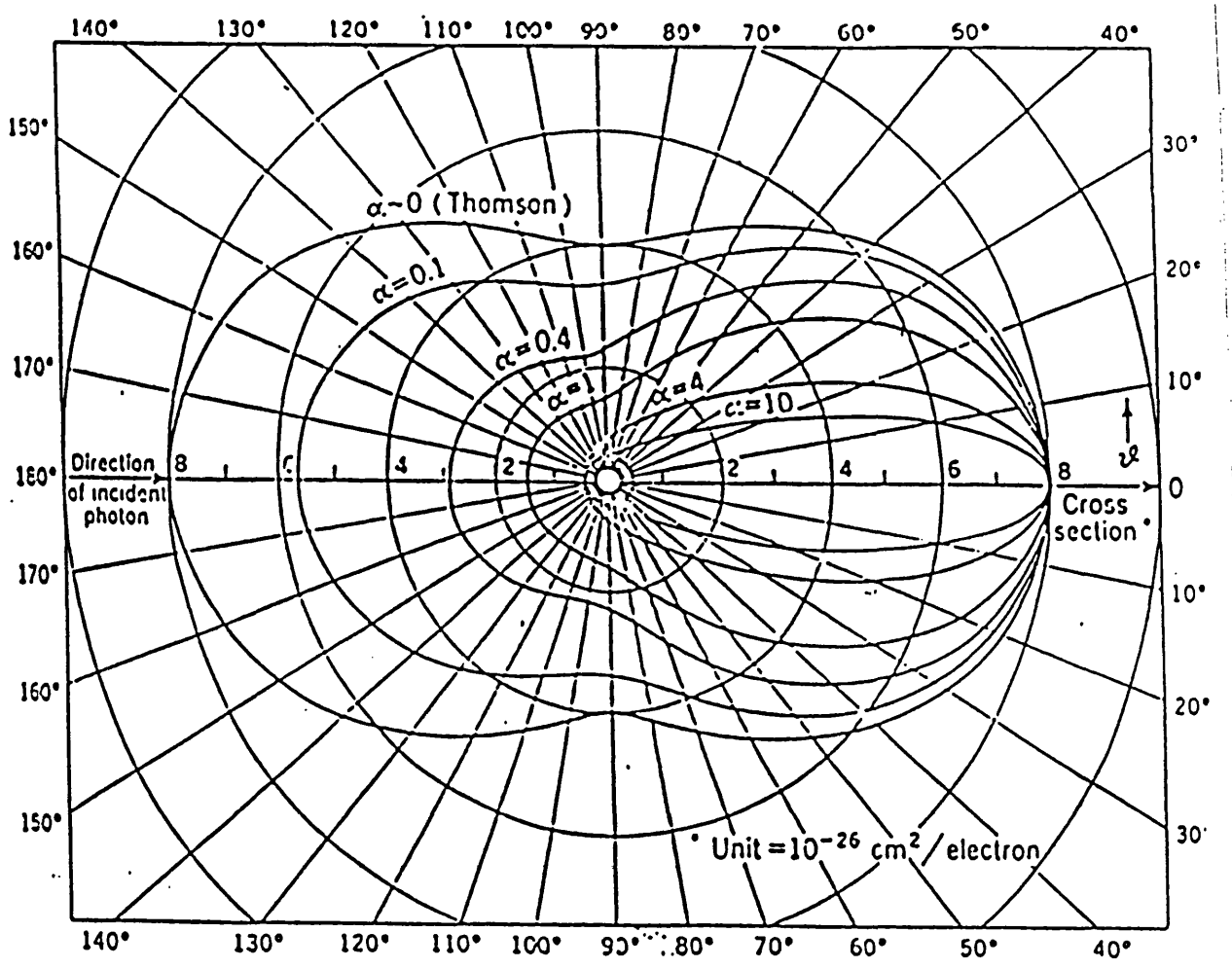

Figure 2.2.1 - The number of photons scattered into unit solid angle $d\sigma/d\Omega$ at a mean scattering angle of θ. (Evans, 1955)

various values of θ is shown in figure 2.2.1. From the figure it is clear that, as photon energy rises the distribution becomes more peaked in the forward direction.

2.2.2 Photoelectric effect

In this process the incident photon energy is dissipated in ejecting a bound electron from an atom. The ejection of the electron will leave a vacancy to be filled by an electron from another shell.

For this process to occur the incoming photon must obviously have an energy greater than that of the bound electron. The bound electron is then ejected with a kinetic energy, Q, given by equation 2.2.8 where E_0 is the energy of the incoming photon and E_B is the binding energy of the ejected electron.

$$Q = E_0 - E_B \tag{2.2.8}$$

After the photo-electron has been ejected the atom is left in an excited state. The ground state energy is however quickly regained (within 1fs) by one of two processes. Either the Auger process, where one or more outer shell electrons are ejected. (This is not of any interest to the project since these electrons are absorbed within a short distance in tissue.) The other possibility is by emission of an X-ray of characteristic energy (XRF).

This process results in a sharp increase in absorption cross-section just above the binding energies of the electrons for any given element. This is demonstrated in figure 2.2.2 (Hubbell, 1968).

It should be noted that photons of energy greater than but just above the L absorption edge have a much greater cross-section for photoelectric absorption than those just above the K absorption edge. It might therefore be thought that it would be better to use L X-rays when designing an XRF system. However L X-rays have a much greater linear attenuation coefficient, μ, in tissue than the K X-rays. The L X-rays are therefore almost completely absorbed before

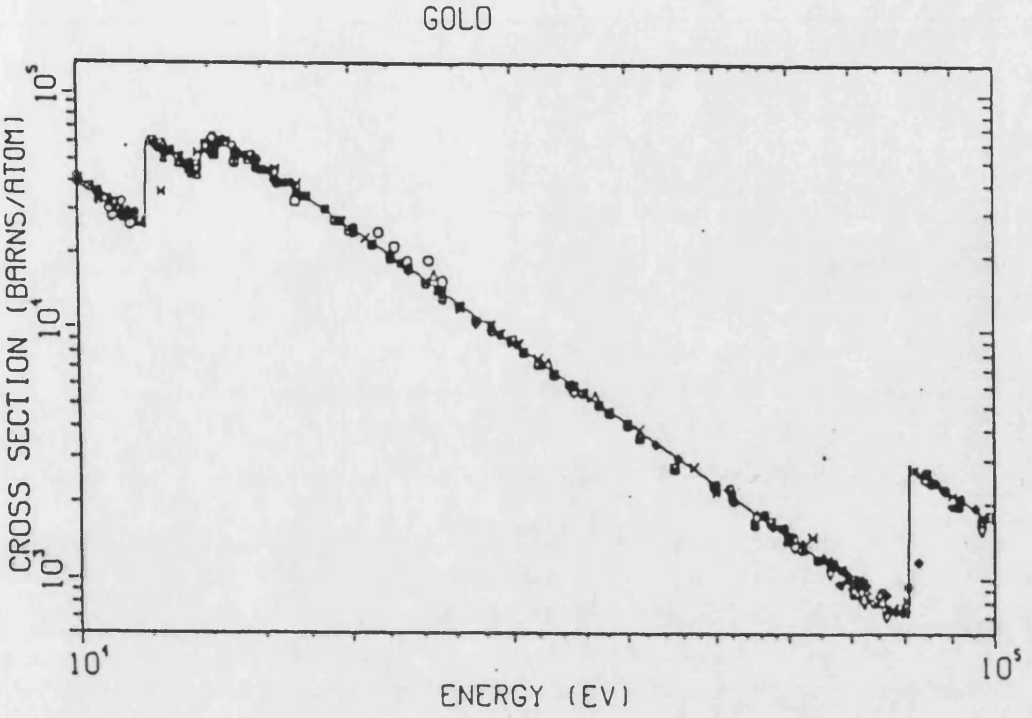

Figure 2.2.2 - Total X-ray cross-section for gold (Z=79)

reaching the skin surface, if they are emitted from the kidney which lies at a depth of greater than twenty-five millimetres.

$$I = I_0 e^{-\mu x} \tag{2.2.9}$$

Equation 2.2.9 gives the reduction in intensity of an X-ray beam, incident intensity I_0, passing a distance x through a medium of linear attenuation coefficient μ. The linear attenuation coefficient, μ, is a function of both energy of the incident photons and composition of the medium. Using a value of $\mu = 0.1639 mm^{-1}$ (Hubbell, 1982), and a value of x = 30mm (a typical kidney depth) gives a value of $I/I_0 = 0.00073$. Showing that almost complete absorption occurs for L X-rays.

Although the consideration of conservation of momentum means that a photon can not be completely absorbed when it interacts with a free electron in the

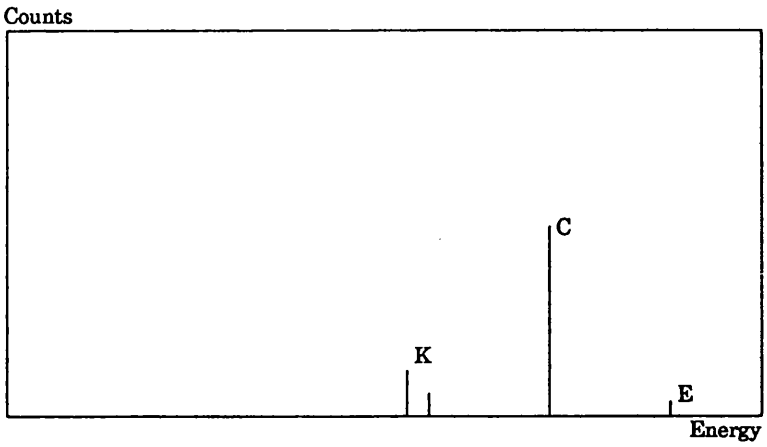

Figure 2.3.1 - Ideal Spectrum

Compton process, this is not true of the photoelectric effect since the photon interacts with a bound electron and the whole atom can recoil.

2.3 The ideal spectrum

From the consideration of the basic physics, the ideal spectrum that would be obtained from an idealised experimental setup is shown in figure 2.3.1.

In this ideal situation the following assumptions are made:

- Both source and detector may be considered as points.
- Both source and detector are perfectly collimated. (Therefore only one sharp scattering angle is seen.)

In this spectrum the following features should be noted:

- K - These sharp lines correspond to the K_α lines of gold. The K_β lines would also be present, but due to their reduced intensity they are not visible on this scale.
- C - Is the Compton peak, this corresponds to Compton scatter of one angle only. i.e. A scatterer that is infinitesimally small in size.
- E - These are peaks that are at the same energy as the source and are due to elastic scatter of the exciting photons.

The non-ideality of these features is discussed in greater detail in the following sections.

2.4 Contributions of the detection system to non ideality

A small amount of non-ideality in the spectrum can be attributed to the components of the detection system. However, with the exception of pulse shape timing, the effects are very small and are fixed for any given detection system.

2.4.1 Detector resolution

Detector resolution is that width which a peak recorded from a single energy photon will appear to have. Hyperpure germanium detectors of the type used in this project are usually supplied with a quoted resolution at photon energies of 5.9keV (^{55}Fe), 122keV (^{57}Co) and 662keV (^{137}Cs). Better resolution is usually obtained with smaller diameter detectors.

The full width half maximum, W_t, of a typical peak in the spectrum can be modelled in the following way (Knoll, 1979):

$$W_t^2 = W_D^2 + W_X^2 + W_e^2 \qquad (2.4.1)$$

where the W values on the right-hand side are the peak widths that would be observed due only to effects of carrier statistics, charge carrier collection and electronic noise respectively.

W_D represents the inherent statistical fluctuation in the number of charge carriers created by the incident photon in the detector, and is given by

$$W_D^2 = (2.35)^2 F\varepsilon E_0 \qquad (2.4.2)$$

where F is the Fano factor, ε is the energy required to generate one electron-hole pair, and E_0 is the energy of the incoming photon. This statistical fluctuation is the primary contribution to the FWHM of the peak in small detectors. The values quoted for the detector used (10mm diameter, 7mm thick)

were checked and found to be accurate.

The second term, W_X, is due to incomplete charge collection in the detector. Its magnitude can be determined experimentally by carrying out a series of FWHM measurements at different applied bias voltages. It is usually assumed that if the bias could be made infinitely large then the contribution of incomplete charge collection would be negligible. A plot of FWHM of the 122keV peak from a ^{57}Co source against bias voltage, showed that at the recommended bias voltage (of -1000V) this effect was negligible for the detector used.

Another effect of incomplete charge collection is that a shelf is seen on the low energy side of peaks. This shelf corresponds to the photons being assigned a value that is too low in energy, because the charge was not completely collected. The presence of this shelf can be clearly seen in figure 2.4.1.

The third factor, W_e, results from electronic noise due to all the electronic

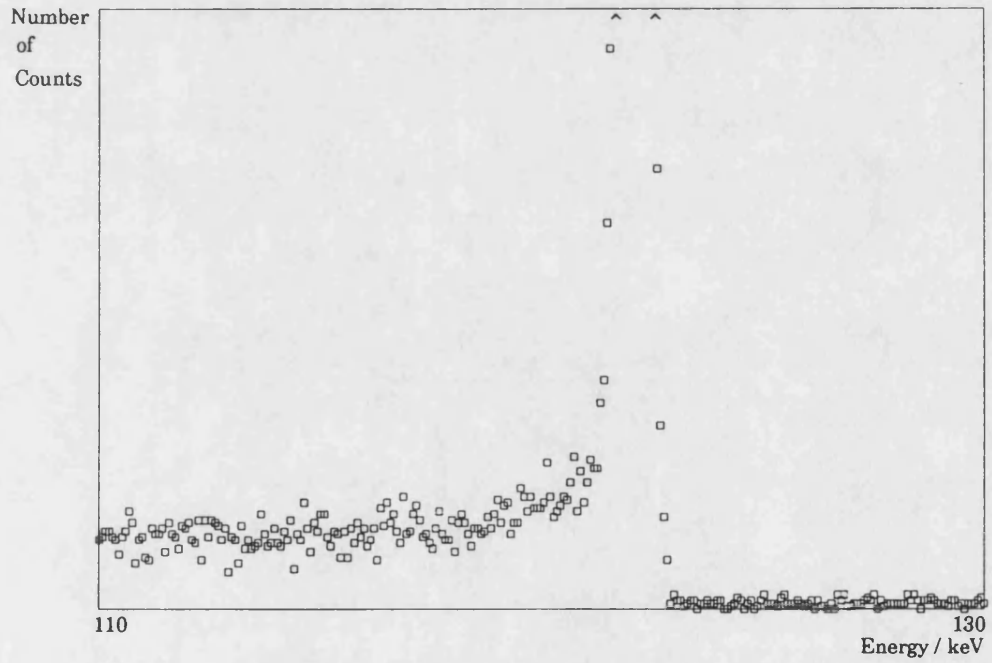

Figure 2.4.1 - 112keV emission peak from a ^{57}Co source placed in front of the detector window. Neither the detector nor the source were collimated. There was no scattering medium present except the holder that the detector is mounted in. Note the expanded vertical scale necessary to show this shelf. The shelf height is approximately 1% of the peak height.

components following the detector. Its magnitude may be measured by connecting the output of a precision pulser with highly stable amplitude to the preamplifier. A parallel test pulse input to the preamplifier is usually present for this purpose. It should be noted that the value of W_e is not entirely independent of the detector itself. Large detectors tend to have large capacitance and therefore larger electronic noise figures.

2.4.2 The 'Compton shoulder'

The 'Compton Shoulder' is a feature that can be seen in spectra of this type and is caused by the energy of the incoming photon not being completely absorbed. i.e. The photon undergoes a number of interactions within the detector, but then escapes before its energy is completely absorbed. In normal circumstances, all scattering angles will occur in the detector. The energy, E_e, transferred to an electron in any one of these scattering events is given by

$$E_e = E_0 - E \tag{2.4.3}$$

where E_0 is the energy of the incident photon and E is the energy of the scattered photon given by equation 2.2.2. Therefore by substituting equation 2.2.2 into equation 2.4.3 we obtain an expression for the energy, E_e, transferred to an electron in any one interaction.

$$E_e = \frac{E_0}{\frac{m_e c^2}{E_0(1 - \cos\theta)} + 1} \tag{2.4.4}$$

where $m_e c^2$ is the rest mass energy of an electron, and E_0 is the energy of the incident photon. If the photon escapes from the detector after only one interaction the detector registers a photon of energy E_e. This energy has a maximum value corresponding to $\theta=180°$. We therefore obtain an edge at this maximum energy, E_c, given by equation 2.4.5 and a continuum of energies below it; corresponding to the energies it is possible to transfer to an electron in a single interaction.

$$E_c = \frac{E_0}{\frac{m_e c^2}{2E_0} + 1} \qquad (2.4.5)$$

Table 2.4.1 shows the position of the Compton shoulder for various isotopes. It can be seen that the Compton shoulder will be well below the gold fluorescence peaks for exciting sources near the K absorption edge of gold.

In fact experimentally the Compton edge could not be seen for either ^{241}Am or ^{57}Co and was only visible in the ^{137}Cs spectrum (figure 2.4.2). This can be explained using equation 2.2.9. If a value of the linear attenuation for germanium is used for a photon energy of 100keV, x = 7mm. We obtain the result that $I/I_0 = 0.12$. However for a photon energy of 600keV we obtain $I/I_0 = 0.79$ (Hubbell, 1982). Thus demonstrating that for a ^{57}Co source we would expect only 12% of the photons to be incompletely absorbed and for ^{137}Cs about 79% of the photons to be incompletely absorbed. Therefore we would expect the Compton shoulder for the ^{137}Cs system to be about 7 times larger than for the ^{57}Co system.

2.4.3 Pulse shape timing

The pulse shape timing is a parameter of the electronic amplification system used. The term refers to the time constant in RC circuits used to change the shape of the incoming pulse. In general a shorter shaping time yields a higher achievable count rate, but the width of the X-ray peaks increases (the resolution of the detector decreases) and hence the signal to background ratio is reduced as the total number of counts in the peak remains constant. The pulse shape timing must be optimised for any given source.

Isotope	Main Photon Energy / keV	E_c / keV
^{241}Am	59.54	11.3
^{57}Co	122.06	39.5
^{137}Cs	662	478

Table 2.4.1 - Energies of Compton edge for various isotopes

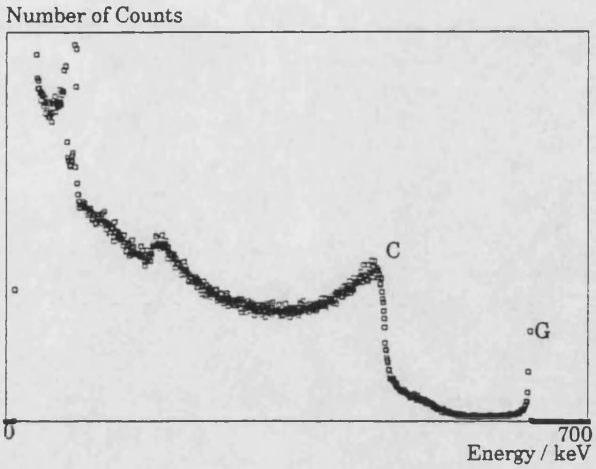

Figure 2.4.2 - Spectrum recorded when a ^{137}Cs source was placed in front of the detector window. The γ-emission peak (G) and Compton edge (C) are clearly visible

2.5 The Compton peak

It is clear that in practice it is impossible to collimate perfectly either the source or the detector. Otherwise the time taken to make a measurement would be prohibitively long. Therefore in a practical situation we expect the Compton peak to have a finite width, corresponding to a finite spread of scattering angles accepted by the detection system and the detector resolution effects discussed in section 2.4.1.

By considering the geometry of the experimental apparatus, the collimation of both source and detector, the finite size of both source and detector and amount and position of any scattering material present, it should be possible to predict both the shape and position of the Compton peak.

A series of four computer programs were written to model the response of the detector to Compton scattered photons in a typical experimental set up (figure 2.5.3) with varying degrees of sophistication. In the first three models, each point in the scattering medium lying in the plane containing both the centre of the source and the centre of the detector was considered.

The first of these models simply considered the proportion of the source and detector each point could see and allowed for the effect of the inverse square

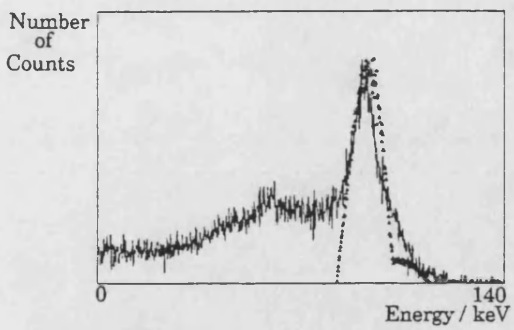

Figure 2.5.1a - Crude model (Model 1)

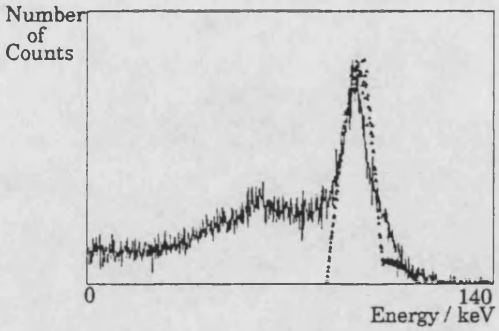

Figure 2.5.1b - Model 2 including finite walls

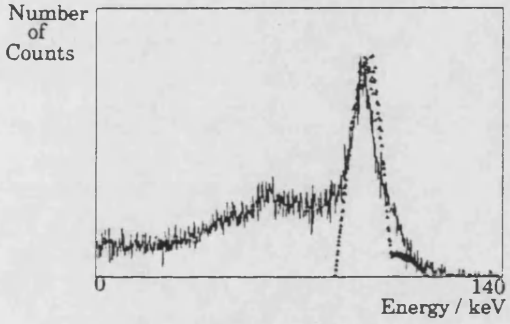

Figure 2.5.1c - Model 3 including attenuation in scattering

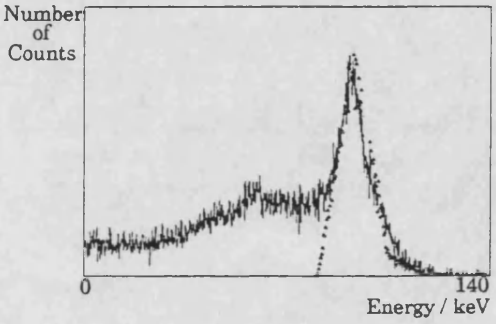

Figure 2.5.1d - Complete three dimensional model (Model 4)

Figure 2.5.1 - Models of Compton scattering with varying degrees of sophistication. Note small lump on high energy side of all the fitted peaks, due to the fact that ^{57}Co is a dual photon energy source (122keV (85%), 136keV (11%)). The Compton scatter of the 136keV peak therefore produces a subsidiary Compton peak on the high energy side of the main peak. Note also the number of points fitted in model 4 is less than the other models.

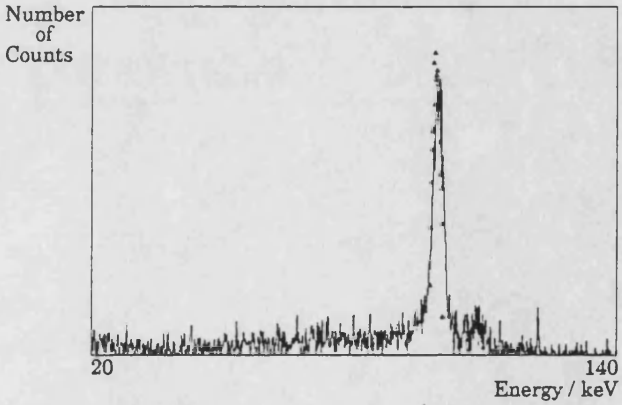

Figure 2.5.2 - A more complete fit can be obtained with systems with less multiple scatter

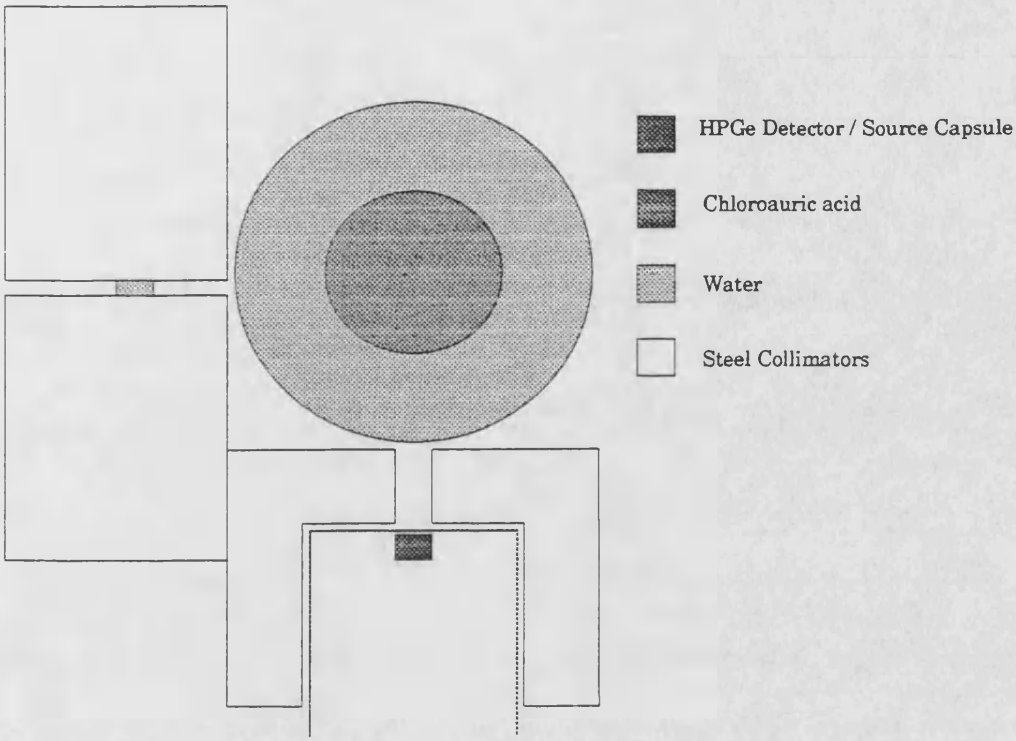

Figure 2.5.3 - Scale diagram of experimental apparatus used to obtain the results in figure 2.5.1. Both the ^{57}Co source and the detector were in steel collimators. A small polythene bottle (47mm diameter) filled with a solution of chloroauric acid was used to represent the kidney. A glass beaker (90mm diameter) was used to represent the surrounding tissue.

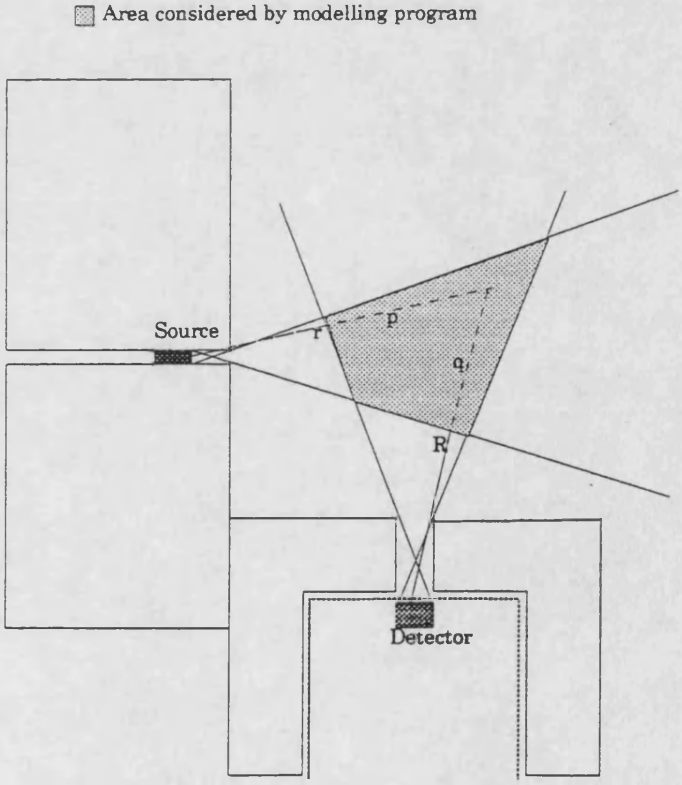

Figure 2.5.4 - Diagram illustrating the area considered by the Compton model program. The diagram also shows the parameters r, R, p & q used by the program.

law. The second model included effects due to finite wall thickness in the collimators. The third model included an approximation for the attenuation of the primary and scattered photons when passing through the scattering medium. (It was assumed the linear attenuation coefficient varied linearly with photon energy over the energy range of interest (60-120keV).)

The fourth and most sophisticated model allowed a full three dimensional consideration of the scattering medium. The results of these four models fitted to a typical system are shown in figure 2.5.1. Note all the models ignore the Klein-Nishina formula (2.2.3) and assume equal probability for all scattering angles. This assumption is justified by the success of the models, although a careful examination of figure 2.2.1 would not necessarily lead to this conclusion for photons of around 100keV ($\alpha \approx 0.2$).

The modelling procedure in all cases involved considering a number of points in the area defined by the two collimators (figure 2.5.4). If the point was within the scattering medium and could be 'seen' by at least some of both source and detector, its contribution was added to the model spectrum. The contribution, δ, of any given point is given by equation 2.5.1.

$$\delta = \frac{g}{r^2} e^{-\mu p} \frac{G}{R^2} e^{-\mu q} \qquad (2.5.1)$$

where g is the fraction of the source the point could 'see', G is the fraction of the detector the point could 'see', r is the distance from the point to the centre of the source, R is the distance from the point to the centre of the detector, p is the distance the unscattered photon travels through the scattering medium, q is the distance the scattered photon travels through the scattering medium and μ is the linear attenuation coefficient for a photon in the scattering medium and is a function of energy. From figure 2.5.1 it is clear that a fairly good fit of the centre section of the Compton peak can be obtained using this type of model especially using the full three dimensional model (model 4). It is also clear however that the models allowing for finite wall thickness in the collimator and

attenuation in the water (models 2 and 3) are not significantly better than the crudest one. This indicates that these refinements are insignificant. Therefore it is sensible to use the (simple) three dimensional model (model 4) for future predictive work. It is also noted that the fit obtained from the models is very good on both the low energy side and the centre regions of the Compton peak. However the fit obtained on the high energy side is less good. It appears that there is more tailing in practice than would be expected, which may be explained by the presence of multiple scattering:

If a single scatter event through angle θ is considered, then the energy of the scattered photon, E, is given by equation 2.2.2. Now considering a double scattering process through the same total angle: (i.e. A scattering event through an angle β, followed by another scattering event through an angle θ-β.)

The energy of the incoming photon after the first scattering event is given by equation 2.5.2.

$$E' = \frac{E_0}{1 + \frac{E_0}{m_e c^2}(1 - \cos\beta)} \qquad (2.5.2)$$

Similarly the energy of the photon after the second scattering event is given by equation 2.5.3.

$$E'' = \frac{E'}{1 + \frac{E'}{m_e c^2}(1 - \cos(\theta - \beta))} \qquad (2.5.3)$$

Combining these equations 2.5.2 and 2.5.3 gives equation 2.5.4.

$$E'' = \frac{E_0}{1 + \frac{E_0}{m_e c^2}[2 - \cos\beta - \cos(\theta - \beta)]} \qquad (2.5.4)$$

Now consider the difference between the denominators of equations 2.2.2 and 2.5.4. This expression can be simplified to have the form of equation 2.5.5.

$$d_{2.2.2} - d_{2.5.4} = \frac{2E_0}{m_e c^2} \sin\frac{\theta - \beta}{2} \cos\frac{\theta}{2} \sin\frac{\beta}{2} \qquad (2.5.5)$$

It is noted that from consideration of geometry the following conditions are imposed for most double scatter events:

$$-180° < \theta < 180° \tag{2.5.6}$$

$$-180° < \beta < 180° \tag{2.5.7}$$

$$\text{If } \beta>0\ ,\ \theta>\beta \text{ Otherwise } \theta<\beta \tag{2.5.8}$$

From these conditions it is seen that expression 2.5.5 is always positive if θ and β have the same sign. Which implies that $E < E''$. (i.e. Less energy is lost in a double scatter event than a single scatter event for any given angle. (This is illustrated in table 2.5.1.) Therefore if double scattering occurs we would expect to see more high energy photons than would otherwise be expected. This would explain the high energy tailing on the Compton peak. The results in figure 2.6.2 are also consistent with this explanation, as when the amount of scattering medium is reduced, so is the degree of high energy tailing on the Compton peak.

2.6 The low energy 'shelf' below the Compton peak

Examining a typical spectrum (figure 2.5.1) we see a high level of residual background at energies lower than the Compton peak. As the source is monochromatic in energy and is therefore not directly responsible for these low energy photons. The most conceivable source of this residual background is from secondary (and higher order) scatter. It should be noted that this background is too large in magnitude to be attributed to incomplete charge collection. As the background due to incomplete charge collection is typically

Number of Events	Angle of each Event	Total Angle	Final photon Energy /keV
1	90°	90°	98.6
2	45°	90°	107.0
3	30°	90°	111.3
4	22.5°	90°	113.7

Table 2.5.1 - Illustrating that a 122keV photon undergoing a number of scattering events, but the same total scattering angle, loses less energy than a 122keV photon undergoing one single scattering event.

only 1% of peak height, whereas these background levels are up to at least 50% of peak height. If secondary scatter is responsible for this residual background then the height of the background should increase with amount of scattering medium present. A series of experiments was therefore performed to test this hypothesis. The detailed setup was similar to that described in section 2.5. Here, instead of a water bath containing a polythene bottle of gold solution, various sized perspex cylinders were centred in the source beam and the detection area as shown in figure 2.6.1. A selection of results is shown in figure 2.6.2.

The results show that as the amount of scattering medium is increased the residual background height increases. For the 6mm diameter container (figure 2.6.2a) theoretically the chance of a primary scatter event is approximately 10% (using 2.2.9 again). Therefore the probability of a secondary scatter event is small - of the order of 1%. However with the 90mm diameter container, for example, the chance of a primary scattering event is approximately 80% and therefore the chance of a secondary scattering event is greatly increased. This residual background is therefore consistent with secondary scattering events, and consequently an inherent feature of the spectrum.

Examining figure 2.6.2b (and most other spectra with secondary scattering present) we notice a shoulder, S. As this shoulder only seems to appear in spectra with multiple scattering it seems likely that the shoulder is attributable in some way to multiple scattering. One obvious possibility is that it corresponds to the maximum possible energy it is possible to lose in two scattering events. The maximum energy loss obtained from these two scattering events is when the denominator in equation 2.5.4 has its maximum value. Differentiation of this denominator with respect to both θ and β leads to the conclusion for maximum energy loss:

$$\beta = -\theta \qquad (2.6.1)$$

If values of θ corresponding to the minimum and maximum scattering angles

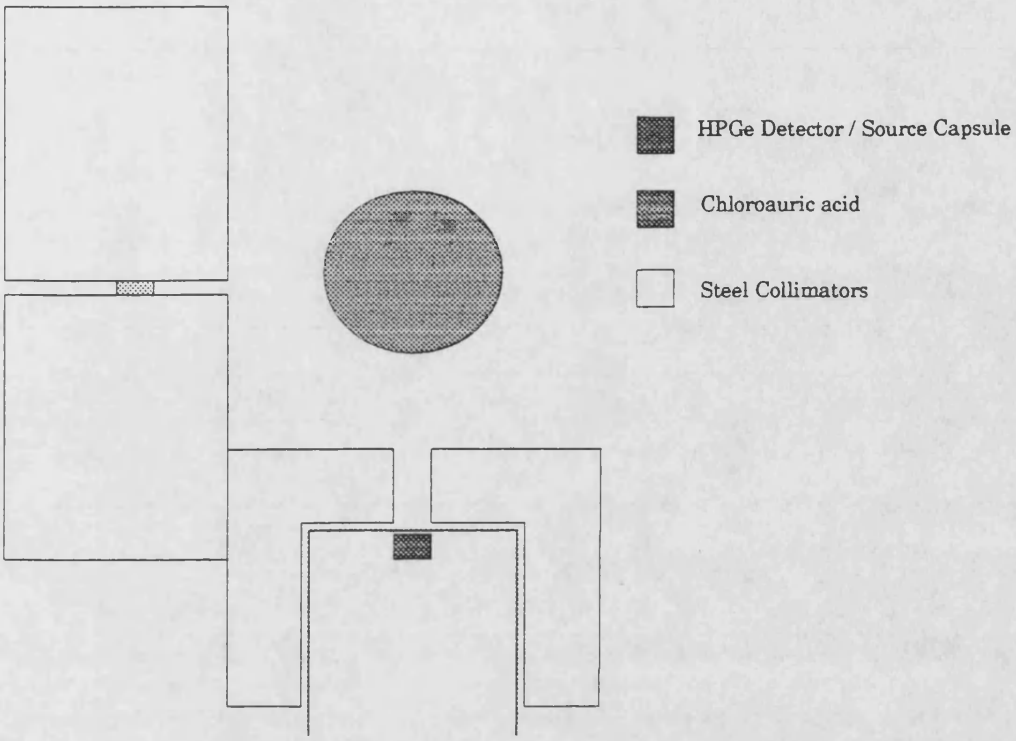

Figure 2.6.1 - Schematic diagram of experimental apparatus

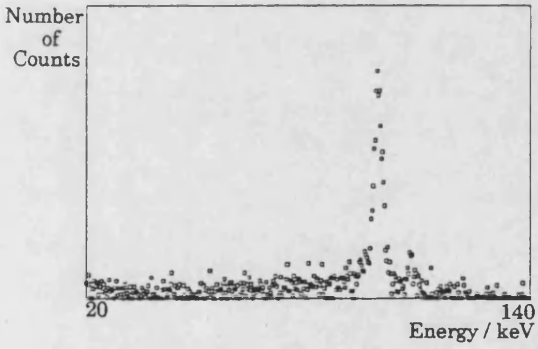

Figure 2.6.2a -6mm diameter container

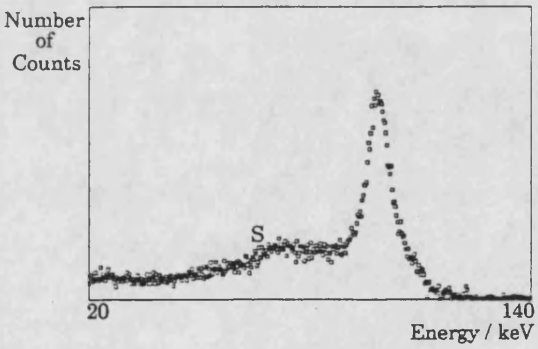

Figure 2.6.2b - 47mm diameter container

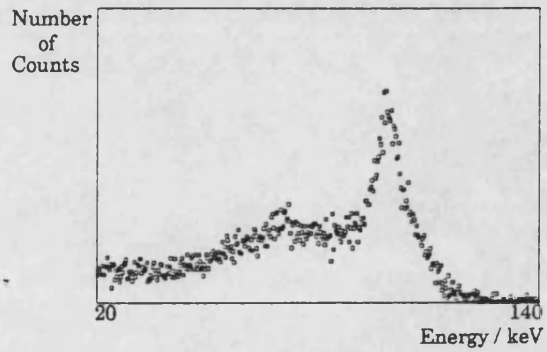

Figure 2.6.2c - 90mm diameter container

NB: These spectra have had the 'background' recorded when no scattering medium was present subtracted.

Figure 2.6.2 - Compton peaks for varying amounts of scattering medium. Note the decrease in the Compton height/residual background height ratio for increased amounts of scattering medium.

the collimation system will accept are substituted into equation 2.5.4 using condition 2.6.1, it is found that the resulting range of energies corresponds to the range of energies over which the shoulder is seen. This shoulder is therefore attributed to the maximum energy it is possible to lose in two Compton scattering events. To confirm this a spectrum similar to that in figure 2.6.2b was taken using a ^{153}Gd source (97,103keV) instead of a ^{57}Co source (122keV). The resulting spectrum had the shoulder in the position predicted by the theory outlined above. This type of argument is also supported by the results of extensive Monte Carlo calculations performed by Rosenthal and Henry (1990) for $^{99}Tc^{m}$ sources and a sodium iodide detector for use in Nuclear Medicine and Laird *et al* (1982) for ^{57}Co and a hyperpure germanium detector.

It would be useful to try and move this shoulder so that the gold peaks (figure 2.5.1) do not sit on it, as the rapidly varying background makes the evaluation of the magnitude of the gold peaks difficult. The possible ways of doing this are either to use a source of different energy or to rearrange the geometry so that the average scattering angle accepted by the collimation system is changed.

2.7 Conclusions

By considering both the system geometry and the physical processes involved it is possible to understand the features on which the fluorescence peaks sit.

By consideration of just the geometry it is possible to predict the shape of the Compton peak. The exception to this is the tailing on the high energy side of the Compton peak. This tailing is consistent with secondary (and higher order) scatter events.

The rest of the spectrum can be understood qualitatively from the experimental results using scatterers of different diameter: The low energy 'shelf' is also consistent with secondary (and higher order) scatter.

It should now be possible to use this information to make a preliminary evaluation of any systems that are proposed for use in the future.

Chapter 3

Detection Limits

3.1 Introduction

It is important to be aware of the detection limit (DL) of any system. i.e. The minimum concentration (of gold) that can be detected. The aim of the project is to achieve a detection limit of 40μg gold (g tissue)$^{-1}$ at tissue depths of 30 - 40mm. It is therefore important to understand the factors that affect the detection limit and to adopt the experimental arrangement that will achieve the lowest value. The parameters which may be varied are detector/source geometry, collimation, detector size, source to skin distance, detector to skin distance, source energy and phantom depth and each was investigated in turn. First however the meaning of detection limit is considered.

3.2 Detection limit definitions

There are various definitions of detection limit used in the literature. Most are based on the argument that follows (Bevington, 1969).

3.2.1 Standard definition of detection limit

The most common definition of the detection limit of an emission line relates the line intensity to the background count level. The observed number of counts, N_0, is composed of two components: the number of counts in the peak, N_P, and the number of counts in the background, N_B, as illustrated in figure

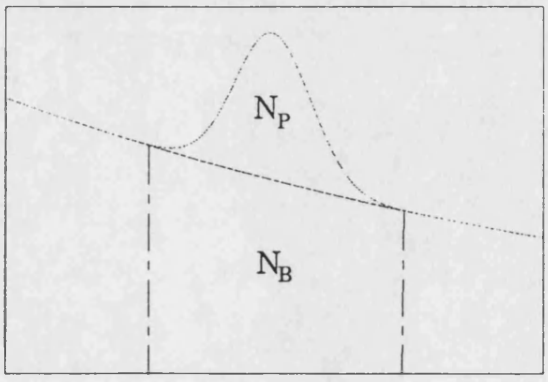

Figure 3.2.1 - Illustration of N_P, N_B, and N_0 (= N_P + N_B)

3.2.1. Poisson statistics are assumed due to the statistical counting process involved. Therefore the total number of counts and related uncertainty (1 standard deviation) is given by equation 3.2.1.

$$N_0 = (N_P + N_B) \pm \sqrt{N_P + N_B} \tag{3.2.1}$$

In order to calculate N_P, the background either side of the peak of interest is fitted and interpolated under the peak. The number of counts in the peak, N_P, and related uncertainty is then calculated by subtraction using 3.2.2.

$$\begin{aligned} N_P &= \left(N_0 \pm \sqrt{N_B + N_P}\right) - \left(N_B \pm \sqrt{N_B}\right) \\ &= (N_0 - N_B) \pm \sqrt{2N_B + N_P} \end{aligned} \tag{3.2.2}$$

Usually $N_B >> N_P$ and therefore equation 3.2.2 approximates to equation 3.2.3 to first order:

$$N_P = (N_0 - N_B) \pm \sqrt{2N_B} \tag{3.2.3}$$

The precise definition for detection limit varies from group to group. Typically the detection limit is defined to be when the number of counts in the fluorescence peak, N_P, is greater than twice (95% certain peak exists) or three times (99.7% certain peak exists) the uncertainty in peak area given by equation 3.2.3. The conditions for a peak to be detectable which are given in 3.2.4 are therefore typical.

$$\begin{aligned} N_{P,DL} &= 2\sqrt{2N_B} \text{ at 2 SD level} \\ &= 3\sqrt{2N_B} \text{ at 3 SD level} \end{aligned} \tag{3.2.4}$$

By assuming that the number of counts in the peak, N_P, is proportional to the concentration, C, of gold in the phantom equation 3.2.5 is obtained.

$$N_P = kC \tag{3.2.5}$$

The constant of proportionality, k, can be determined experimentally (either

from a single result, where k is obtained from the ratio of counts in the peak to the concentration of phantom used ($N_{P,X}/C_X$), or from the least squares fit for a number of results using different concentrations). Combining equation 3.2.5 with condition 3.2.4, the expression (at the 2 standard deviation level) which is given in equation 3.2.6 can be derived.

$$N_{P,DL} = \frac{N_{P,X}C_{DL}}{C_X} = 2\sqrt{2N_B} \qquad (3.2.6)$$

where $N_{P,X}$ and N_B are the number of counts in the peak and background obtained from an experiment and C_X is the concentration of gold solution in the phantom used in that experiment. This can now be rearranged to give the expressions for detection limit given in equation 3.2.7.

$$C_{DL} = \frac{2\sqrt{2N_B}\,C_X}{N_{P,X}} = \frac{2\sqrt{2}\,C_X}{r\sqrt{N_B}} \qquad (3.2.7)$$

where r is the ratio of counts in the peak to counts in the background (N_P/N_B). From equation 3.2.7 it is seen, that using this definition of detection limit, the detection limit decreases with increase in the square root of dose, as N_B is approximately proportional to dose for a given experimental setup, the contribution from the fluorescence lines being small. Consequently if the photon flux (dose rate) is kept constant, detection limit decreases with increase in the square root of time. Similarly if exposure time is kept constant, detection limit decreases with increase in the square root of dose rate.

3.2.2 Other definitions of detection limit

The other definition of detection limit that is commonly used is that a peak is below the detection limit if the peak area returned by the peak fitting program (section 3.8) is less than twice (2 standard deviations) the uncertainty in the peak area returned by the fitting program. This uncertainty in the peak area is derived from how well the model fits the raw data. However it is not so easy to

extrapolate the detection limit from high concentrations using this definition. It is thought that strictly this is a more correct definition and should be used in a clinical system as the uncertainty in the peak fitting program is derived from the data set being used. (Conclusion of panel at International Symposium on *in vivo* body composition studies, Toronto 20-23 June, 1989)

3.2.3 Experimental verification that peak size is proportional to gold concentration, and of predicted detection limit

Although obviously it is possible to predict detection limits using phantoms of high gold concentration and equation 3.2.7, it is unclear how accurate these predictions are. Therefore an experimental investigation was undertaken to establish the validity of this calculation, by firstly verifying that the number of counts in the fluorescence peak were proportional to the gold concentration in a phantom. Secondly by looking for which concentration could not be measured or no longer fell on the line of proportionality.

Two series of experiments were performed in which the concentration of gold in the kidney phantom was varied. In one series a ^{57}Co source was used in a 90° geometry with an experimental arrangement identical to that described in section 3.4.1 and illustrated in figure 3.4.1, and in the other a ^{133}Xe was used in a backscatter arrangement identical to that shown in figure 3.3.1.

In both cases the number of counts in the $K_{\alpha 1}$ gold fluorescence peak (obtained by using the fitting program described in section 3.8) was plotted against the concentration of gold in the phantom. The results are illustrated in figure 3.2.2 and given in table 3.2.1. The predicted detection limits using the 500 $\mu g\, g^{-1}$ phantom result and equation 3.2.7 are 120 and 77 $\mu g\, g^{-1}$ for ^{133}Xe and ^{57}Co respectively.

From these results it is clear that the number of counts in the fluorescence peaks is proportional to the concentration of gold in the kidney phantom. It is also clear that the predicted detection limit is achieved, as the line of

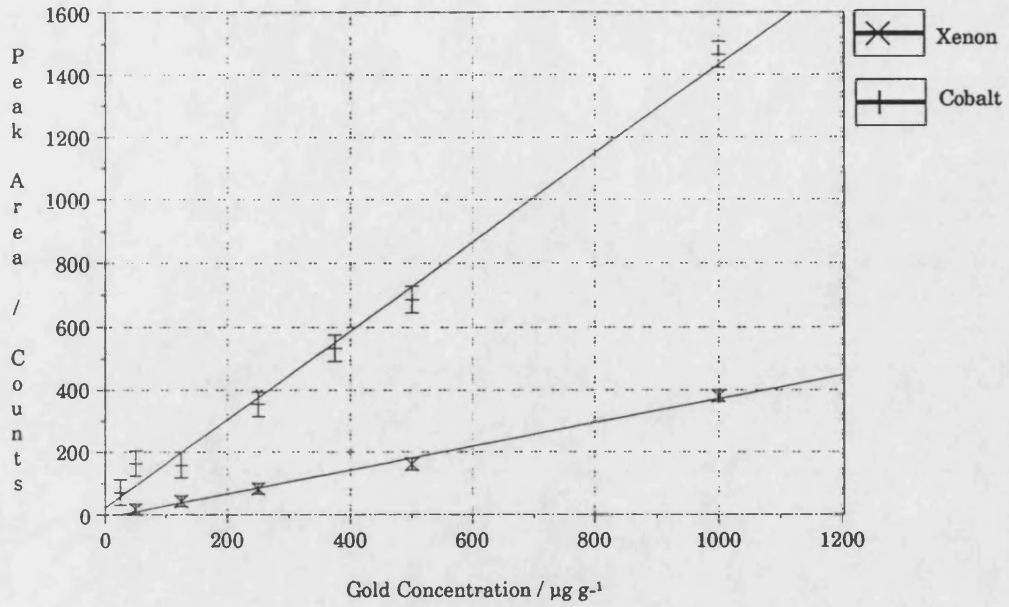

Figure 3.2.2 - Plot of kidney phantom gold concentration against number of counts in the $K_{\alpha 1}$ fluorescence peak. (NB: The error bars on the figure represent the standard error in the number of counts in the $K_{\alpha 1}$ peak as returned by the fitting program.)

Phantom Gold Conc. / µg g^{-1}	$K_{\alpha 1}$ Peak / Counts (^{133}Xe)	$K_{\alpha 1}$ Peak / Counts (^{57}Co)
1000	380±19	1465±42
500	161±19	687±41
375		534±42
250	83±17	354±40
125	43±17	159±41
50	18±17	164±40
25		71±41

Table 3.2.1 - Table of experimental results. The uncertainties in peak area are the standard error in the peak area returned by the peak fitting program

proportionality goes through the predicted detection limit without extrapolation.

3.3 Detector/source geometry

The detector/source geometry refers to the angle between the axis of the detector and the source beam axis. Of the possible geometries the backscatter geometry and 90° geometry have been evaluated by this and other groups although other arrangements are of course available. The angle referred to in

this convention is approximately the average angle of scatter for singly scattered Compton photons, that is accepted by the detector.

3.3.1 90° Geometry

This geometry is used with the ^{57}Co source already described so that the gold fluorescence peaks are not at the same energy as the Compton scattering peak. The inherent advantages of this geometry are that primary Compton scattering is at a minimum at 90° (Evans, 1955) and that it is easy to arrange the collimators for a well defined field of view. Another factor that should be noted is that arrangements with average scattering angles of less than about 135° are the only really practical geometries if an X-ray tube is used as an exciting source as the X-ray tube is too large to accommodate a detector in the backscatter arrangement. The Swansea *In Vivo* Analysis Research Group (SIVARG) have found that the use of two separate collimators makes it much more difficult to keep the organ in the field of view of the well collimated source and is generally much more awkward to align to a patient.

3.3.2 Backscatter geometry.

A second detector/source geometry that has been investigated is one in which the scattered and fluorescence photons are detected at the maximum possible angle from the source beam (ideally 180°).

In this geometry the source is an annular source placed around the detector although shielded from it. A typical arrangement is shown in figure 3.3.1. From the figure it is clear that the average scattering angle is between 150° and 160°. Since with this type of setup the source, source collimator and detector collimator are in the same unit, positioning of the apparatus / patient becomes much easier as only one collimator has to be located.

This type of system has been adopted by the Swansea group using $^{99}Tc^{m}$ as a source for detecting platinum in neck tumours after cis-platin therapy. The reasons for this decision are two fold: firstly the smaller compact

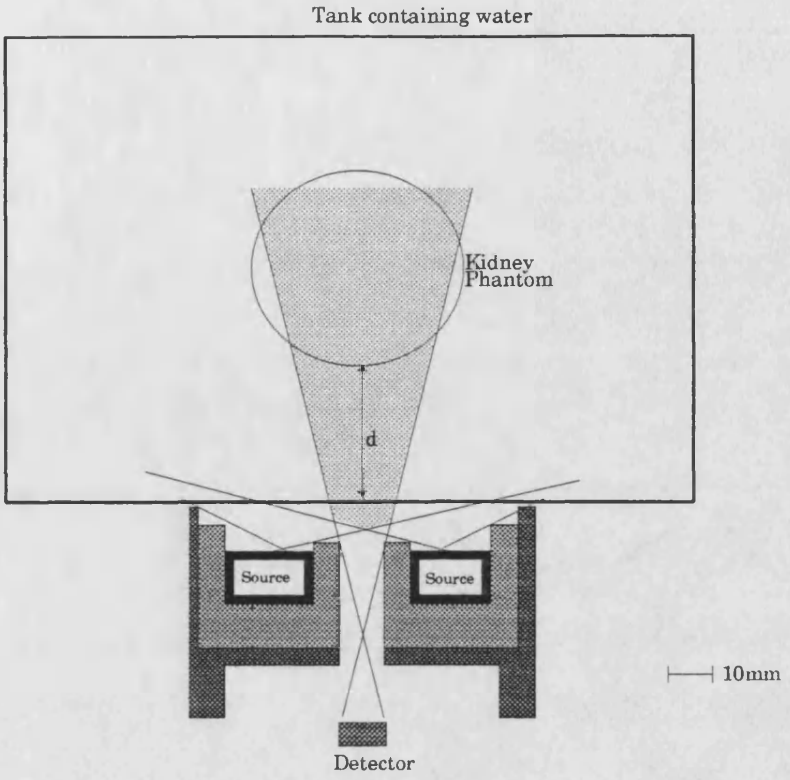

Figure 3.3.1 - Typical experimental arrangement for backscatter geometry

detector/source head is easy to position in the relatively confined space in the neck area (Al-Sadhan *et al*, 1989) secondly $^{99}Tc^{m}$ is a cheap and readily available source as it is used routinely in nuclear medicine studies.

The initial reason for adoption of the backscatter geometry was that if a source of energy just above the K absorption edge of the metal of interest is used, the fluorescence peaks lie above the Compton scattering peak as the Compton scattering energy loss is greatest at large scattering angles. Examining figure 2.5.1 it is seen that if the fluorescence peaks lie above the Compton peak in energy they sit on a much lower background. Applying equation 3.2.7 the detection limit should therefore be much lower. It turns out from equation 3.3.1 that, in order for the fluorescence peaks to lie above the Compton peak, the source must have a energy as close as possible to the K absorption edge of the metal of interest. The exciting source being close in energy to the absorption edge metal also maximises the probability of the photoelectric effect and

therefore the intensity of the fluorescence signal.

$$E = \frac{E_0}{1 + \frac{E_0}{m_e c^2}(1 - \cos\theta)} \qquad (3.3.1)$$

Much work has been done by Somervaille *et al* (1985) on this type of system for bone lead. For bone lead work a ^{109}Cd source (88.0keV) is used to excite lead (K_{abs}= 88.0keV) in tibia. For tibia there is very little overlying tissue and multiple scatter caused by overlying tissue is minimal. Quoted detection limit is 10μg (g wet bone)$^{-1}$ at an absorbed dose of 100μGy to 1.5kg of non-radiosensitive tissue (Chettle *et al*, 1989). A similar type of system is possible for detection of gold (K_{abs}= 80.7keV) using a ^{133}Xe (81.0keV) source, although xenon, being gaseous, is in an inconvenient physical form and therefore difficult to obtain high activities. A diagram of the collimators used for the evaluation of this system is shown in figure 3.3.2.

The disadvantage of this type of system is that the sensitivity falls off rapidly with tissue depth as reported by the Swansea group (Dutton *et al*, 1985) and supported by our own results. This phenomenon is discussed further in section 3.7.

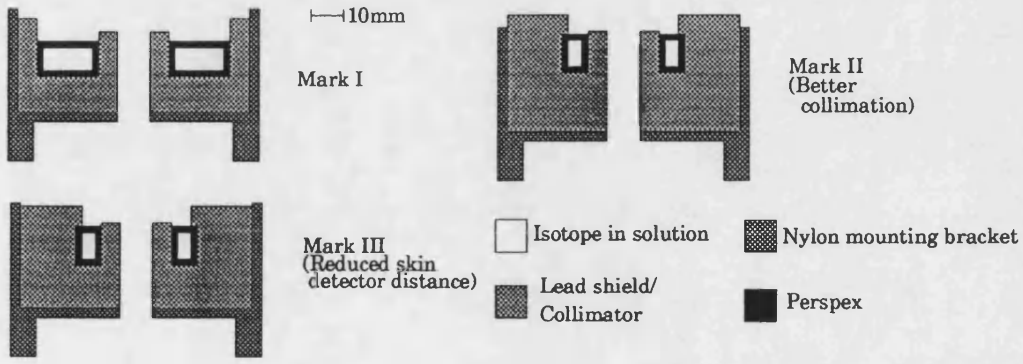

Figure 3.3.2 - Different versions of the backscatter collimator

3.4 Collimation

When making a comparison of results it is also important to be aware of the effect of the position of the kidney phantom in relation to the field of view of the collimators. If the whole of the phantom is within the field of view of both collimators then the detector effectively measures total gold content rather than gold concentration. However if only a section of the phantom is within the field of view of the collimators then the system effectively measures gold concentration in the field of view of both collimators. This however is only an approximation which ignores the effect of attenuation of both the exciting source and fluorescence emission.

An experimental investigation into the effect of source collimation was undertaken. In this investigation the depth of the ^{57}Co source in a cylindrical collimator was varied to produce different fields of view. The source to skin distance was kept constant throughout in order to deliver constant skin and kidney doses. The detector collimation was also kept constant. The source was used to irradiate a kidney phantom (containing 500μg gold (g water)$^{-1}$) in a rectangular tank of water. The depth of the phantom measured along the source axis was 50mm and along the detector axis was 30mm, these being typical kidney depths in the human body. The detector collimator was placed as close as possible to the tank wall. A diagram of the apparatus is shown in figure 3.4.1. The full angular width, θ, of the source beam was varied. A summary of the results is given in table 3.4.1.

Beam Angle /°	$K_{\alpha 1}$ Peak (N_P) /Counts	$K_{\alpha 1}$ Background (N_B) /Counts	N_P/N_B	DL / μg g^{-1}
10±0.3	690± 80	5912	0.114	158±18
20±0.8	2066±153	21579	0.095	111± 8
30±2	2757±204	38891	0.070	101± 7
40±3	3442±231	49892	0.069	92± 6
50±3	4354±273	70613	0.062	86± 5
60±4	4573±261	70832	0.064	82± 5
90±6	4652±285	76269	0.061	84± 5
180	4597±314	93909	0.049	94± 6

Table 3.4.1 - Summary of collimation results

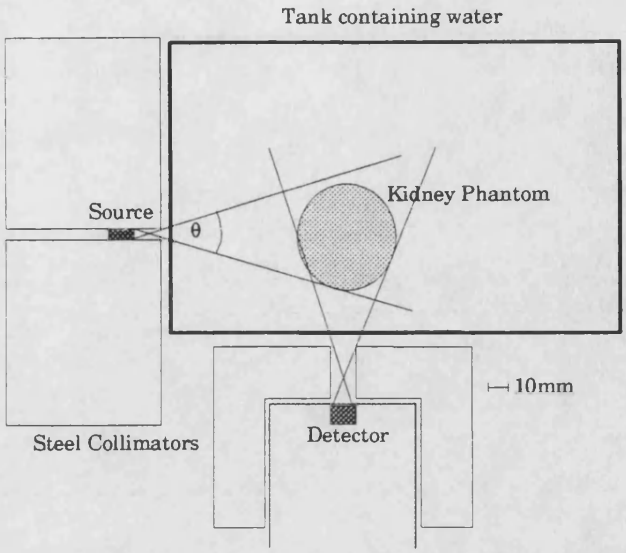

Figure 3.4.1 - Experimental arrangement for source collimation study

The position of the primary Compton scatter peak in the detected photon spectra moves to a higher energy as the angular width of the collimated beam increases, indicating a reduction in the average scattering angle of detected photons. This is illustrated in figure 3.4.2 which shows the spectra for beam angles of 10° and 90°. It is also noted that the proportion of secondary scatter relative to primary scatter increases markedly with decrease in collimation.

Consideration of the results in table 3.4.1 leads to the following conclusions: Firstly the number of counts in the gold $K_{\alpha 1}$ peak increases with volume of phantom seen. Secondly, the number of counts in the background under the $K_{\alpha 1}$

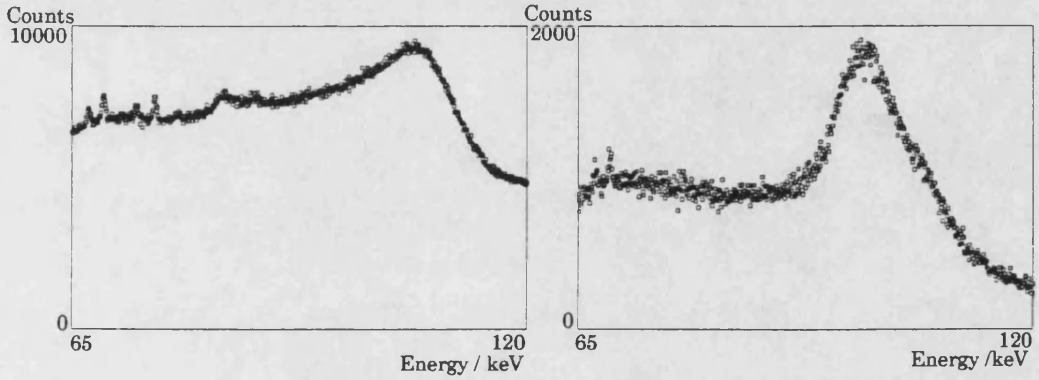

Figure 3.4.2 - Spectra obtained using 10° (Right) and 90° (Left) full beam angles

peak rises with volume of scattering medium seen by the collimators. The background under the fluorescence peaks arises mostly from photons which have been scattered at least twice in the tissue volume before reaching the detector. Figure 3.4.3 illustrates how the peak (N_P) and background (N_B) components increase, as expected, as the volume irradiated increases, but not directly in proportion.

Since the obtaining of the optimum detection limit is the primary aim, it is interesting to note that for a fixed dose the optimum detection limit is not obtained with the same degree of collimation as is the highest peak to background area ratio, r. The reasons for this are found by looking at equation 3.2.7. It can be seen that as the angular width of the collimated beam is varied the detection limit decreases as the denominator of this equation, $r\sqrt{(N_B)}$, increases. Therefore in designing a system for optimum detection limit there is a trade off between peak to background area ratio, r, and count rate (increasing the beam angle increases the count rate and therefore $\sqrt{N_B}$). From equation 3.2.7 it can also be seen that detection limit is proportional to $\sqrt{(N_B)}/N_P$, this

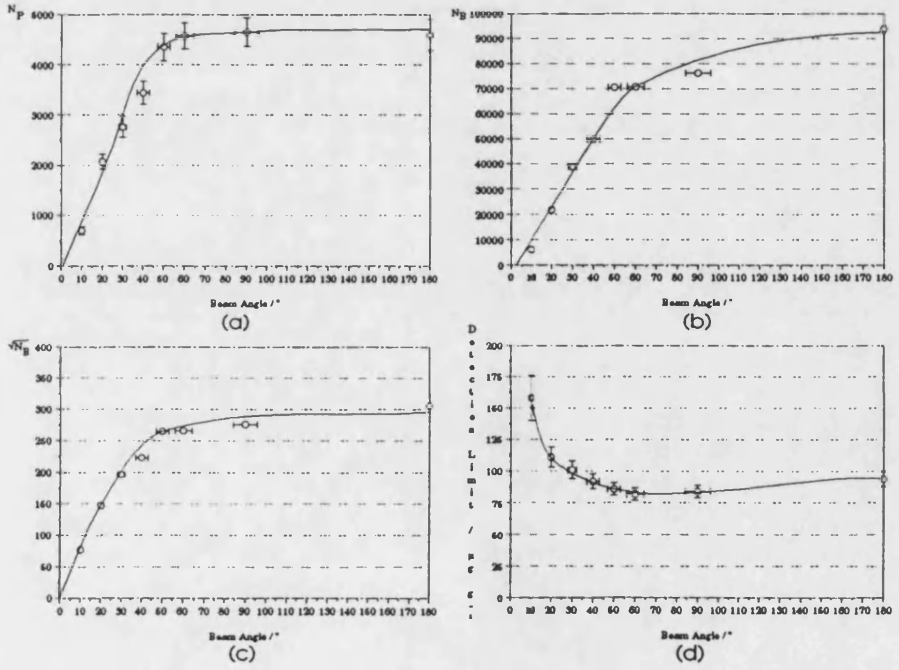

Figure 3.4.3 - Summary of collimation results

allows the variation of detection limit with beam angle to be derived from the measured values of N_P and N_B in the way illustrated in figure 3.4.3. The variation of N_P and N_B are determined experimentally (figures 3.4.3a and 3.4.3b respectively). The variation of $\sqrt{N_B}$ with beam angle can then be calculated directly (figure 3.4.3c), this can then be combined with the variation of N_P with beam angle to give variation of detection limit with beam angle (figure 3.4.3d). The reason for the less rapid increase in detection limit than might be expected for irradiating larger volumes than necessary to just cover the kidney phantom is partly attributable to the fact that detection limit only increases with the square root of counts in the background, whereas detection limit decreases linearly with number of counts in the peak. Empirically our results (both those presented in table 3.4.1 and other results for alternative phantom depths) indicate that the optimum detection limit is obtained when the whole phantom is just irradiated by the whole source (i.e. approximately 50° in the case of the data in table 3.4.1). From figure 3.4.3d it can be concluded that it is better to irradiate a slightly greater volume rather than a slightly smaller volume due to the rapid deterioration of the detection limit with increased collimation (i.e. smaller angular widths of the irradiating beam).

On the assumption that the effect of varying detector collimation will be broadly similar to that of varying source collimation (i.e. the optimum detection limit will be achieved when the whole phantom diameter is just seen by the whole detector) the detector collimator was opened out, such that the whole detector would just see the full diameter of the phantom at a depth of 30mm (figure 3.4.4). A summary of results comparing the new and old collimators is presented in table 3.4.2. The experimental details are similar to those

Detector Collimator	Source Beam Angle / °	N_P / Counts	N_B / Counts	DL / μg g^{-1}
Old	55	4552	68924	81
Old	10	690	5912	158
New	55	10379	153795	53
New	10	1530	16890	120

Table 3.4.2 - Detector collimation results. Phantom gold concentration was 500μg g^{-1}

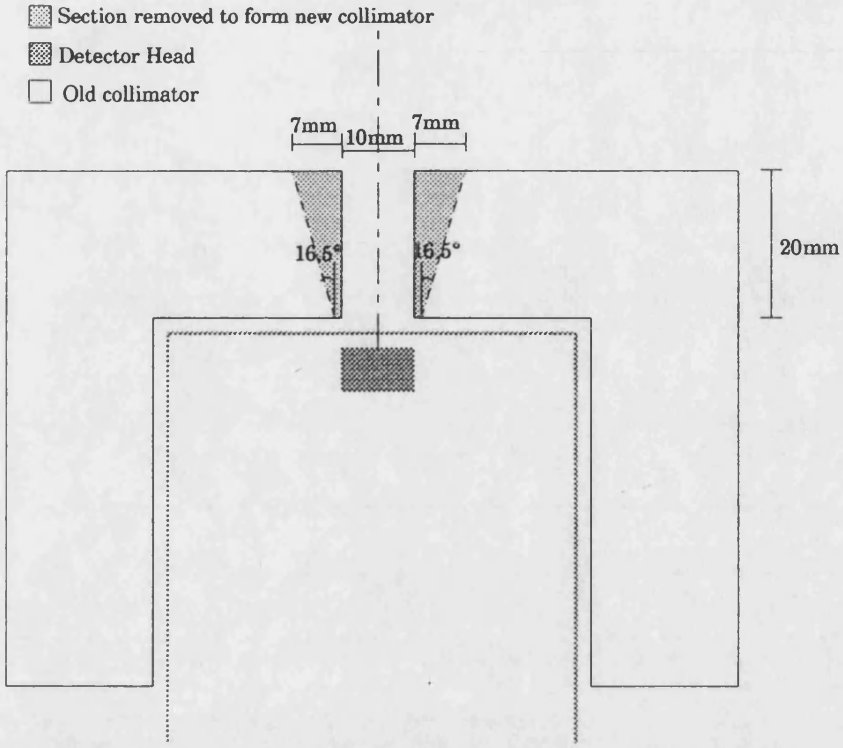

Figure 3.4.4 - Illustration of section removed from old detector collimator to form new detector collimator

described for the source collimation work (figure 3.4.1). The irradiation time and source to skin distance was identical for all the experiments.

From these results it can be seen that (for similar irradiation times) the number of counts in the peak, N_P, for the new detector collimator increases by the same proportion independent of source collimation. This is as expected, due to the fact that the peak size is proportional to the amount of gold seen and the extra volume of gold containing material seen increases by the same proportion in each case. However the number of counts in the background, N_B, increases by a larger proportion for the highly collimated source than for the less well collimated source. This is due to the larger relative increase in secondary/multiple scatter accepted by the detector collimator for the well collimated source than for the less well collimated source. (This is an observed experimental fact.) Combining these results for the peak counts, N_P, and background counts, N_B, leads to the conclusion that the highly collimated source will have a proportionally smaller decrease in detection limit than the

less well collimated source. This is indeed found to be the case. However in both cases a significant reduction in detection limit has been obtained by opening out the detector collimator. It is therefore concluded that varying the collimation of the detector has broadly the same effect as varying the collimation of the source (although two different collimations is a very limited data set) and the new detector collimator gives a significant improvement in detection limit compared with the old one.

It is noted that the detection limits would be completely different if normalised to total absorbed energy rather than an organ dose. This is because with a well collimated beam less energy would be absorbed than with a poorly collimated beam, whereas the collimation of the source beam does not markedly affect skin dose. Therefore a well collimated beam would give a high peak to background area ratio with low absorbed energy and would be the optimum arrangement if total absorbed energy was the limiting factor. However when working to WHO guidelines it is not total absorbed energy but effective dose that defines the limits to permissible irradiation.

3.5 Detector Size

A larger detector should give a reduced detection limit as more photons would be detected in a given irradiation time. The count rate increases proportionally with detector area and therefore the detection limit decreases with increase in square root of the detector area or with increase in detector diameter. This is only an approximation which ignores the effect of poorer collimation and problems caused by higher count rates if high photon flux sources are used, which may reduce the expected improvement to detection limit if a larger detector were used.

The resolution of larger volume detectors is usually poorer than small volume detectors, which can lead to the improvement in detection limit not being as great as predicted from the increase in area. This poorer resolution is primarily due to the lower electric field achievable in these detectors which leads to

greater incomplete charge collection (section 2.4; Knoll, 1979).

3.6 Source energy

It is obviously possible to use sources of different energies. The choice however is limited by the fact that we require a source with a simple spectrum with photon energies close to but above the K absorption edge of gold; without additional higher energy components that cannot be filtered out; that can be obtained in relatively high activities and has a suitably long half life.

If sources lower in energy than the K absorption edge are used there is no cross section for K shell photoelectric absorption and consequently no detectable fluorescence. The maximum cross-section for absorption is obtained if the energy of the source is just above the K absorption edge of gold and as the energy of the source is increased above the K absorption edge the probability of photoelectric absorption decreases. Low activity sources require small skin to source distances to give a sufficient photon count in a limited irradiation time, this leads to large skin doses. A source with a short half life would require replacing regularly and would therefore have high overhead costs.

Table 3.6.1 shows the position of the Compton peak for various available sources, which have suitably simple emission spectra of energy close to the K absorption edge of gold, in the two investigated geometries. It is noted that using ^{153}Gd in a backscatter geometry or ^{133}Xe in a 90° geometry means that the fluorescence lines (67-68keV) are coincident with the Compton peak. If the fluorescence lines are coincident with the Compton peak the detection limit will

	Compton Peak Energy / keV	
Source	90° Geometry	Backscatter Geometry
^{133}Xe	69.9	61.5
^{57}Co	98.4	82.6
^{99}Tc^{m}	109.9	90.4
^{109}Cd	74.7	65.2
^{153}Gd	81.8	70.5

Table 3.6.1 - Compton peak energies

be increased unacceptably as the number of counts in the background, N_B, will be increased (equation 3.2.7).

It is concluded therefore that ^{57}Co, $^{99}Tc^m$ and ^{153}Gd might be suitable sources for use in a 90° geometry and ^{133}Xe, ^{57}Co and $^{99}Tc^m$ might be suitable sources for use in a backscatter geometry.

Preliminary experimental work comparing ^{153}Gd (100keV) and ^{57}Co (122keV) in similar experimental setups has indicated that ^{153}Gd is a better source than ^{57}Co because it is closer in energy to the K absorption edge of gold giving a higher cross section for K shell photoelectric absorption. The experimental results are presented in table 3.6.2. The theoretically predicted ratio of peak sizes could be determined from the ratio of cross-sections for absorption by gold (1.3 Gd:Co) and the ratio of photon fluxes reaching the kidney phantom from equation 3.6.1 (0.90 Gd:Co; 45mm water (to centre of phantom)). Therefore the predicted ratio of peak sizes is 1.2 Gd:Co. The ratio of peak sizes obtained experimentally (1.28 ± 0.13) is therefore explained.

$$I = I_0 e^{-\mu x} \qquad (3.6.1)$$

^{153}Gd is also available in higher activities (up to 37GBq) than ^{57}Co (up to 2GBq) thus allowing larger source to skin distances to be used for a fixed irradiation time. It is not possible to use a source lower in energy than ^{153}Gd in a 90° geometry as the gold fluorescence peaks become coincident with the primary Compton scattering peak.

It is therefore concluded that the effects of source energy can be explained using photoelectric absorption cross-sections and differential absorption of

Source	Phantom Depth /mm	SSD /mm	$K_{\alpha 1}$ Peak / Counts
^{57}Co	22.5	25	369±11
^{153}Gd	22.5	25	475±29

Table 3.6.2 - Comparison of ^{153}Gd and ^{57}Co as sources in a 90° geometry. The skin dose for the results is 5mGy. The concentration of gold in the kidney phantom was 500μg g^{-1}.

different photon energies by overlying tissue.

3.7 Kidney phantom depth

The effect of kidney phantom depth is not a simple problem as the magnitude of the effect is not independent of source energy or detector/source geometry. The effect of phantom depth has been investigated with two systems: ^{133}Xe in a backscatter arrangement and ^{57}Co in a 90° geometry.

3.7.1 ^{133}Xe backscatter system

In the experimental arrangement used the mark I collimator, shown in figure 3.3.2, was mounted on the front of the detector and positioned as close as possible to a beaker of water (115mm in diameter). The kidney phantom was then positioned at different positions within the beaker (figure 3.7.1). Effectively all that is happening in this series of experiments is that the depth, d, of the gold containing kidney phantom is being altered. The amount of water that is in the field of view remained constant as the beaker size remained constant. The results for various kidney phantom depth are presented in table 3.7.1.

The results may be understood partly by considering the effect of attenuation of photons due to overlying tissue and the inverse square law losses. However this simple model ignores any photons which are Compton scattered but still have enough energy to excite fluorescence. Firstly the attenuation of the fluorescence signal and exciting photons due to overlying tissue will be a relatively small factor ($I/I_0 = 0.83$ for 10mm at 80keV). Secondly the application of expression 3.7.1, which gives the form of the inverse square law for a

Phantom Depth /mm	SSD /mm	Peak Area / Counts
10	20	6231±90
20	20	3177±139
30	20	1610±132

Table 3.7.1 - Results from the ^{133}Xe backscatter system with different phantom depths. The skin dose for all the results was 6.5mGy and the peak areas are for the $K_{\alpha 1}$ peak only. The concentration of gold in the kidney phantom was 500μg g^{-1}

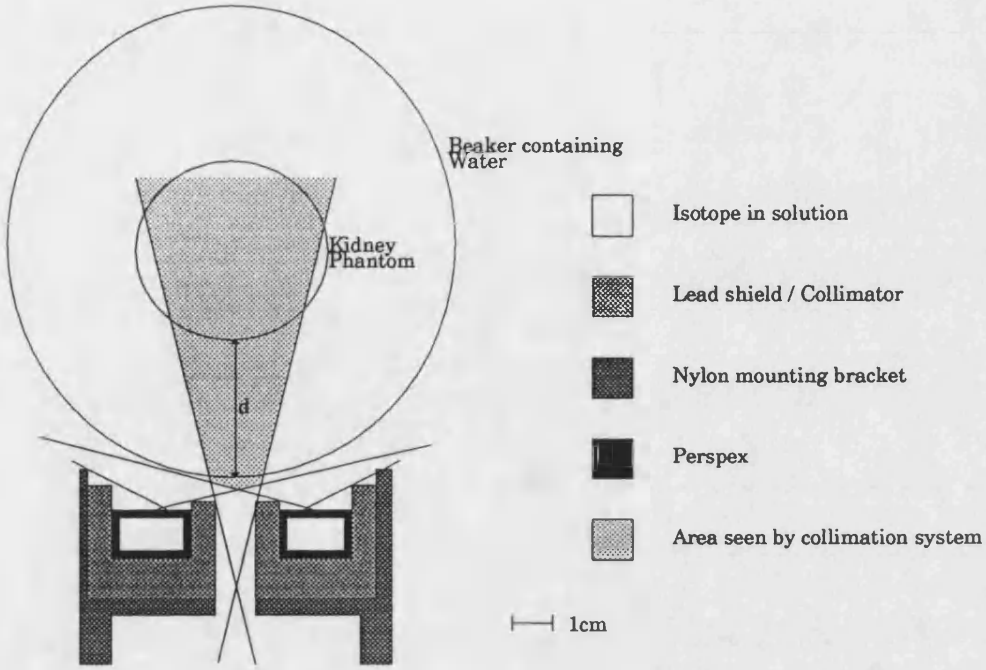

Figure 3.7.1 - Diagram of experimental arrangement for ^{133}Xe work

distance r along the axis from a ring source radius, R, leads to the conclusion that for the dose received by the near side of the kidney phantom when 30mm deep is only 0.49 of that received when 10mm deep.

$$\frac{1}{r^2 + R^2} \tag{3.7.1}$$

The XRF signal received by the detector will also be reduced by the inverse square law. Applying both the attenuation and inverse square law factors, it would be expected that the fluorescence signal from the front surface of the kidney would be reduced by a factor of 11 when the depth is increased to 30mm from 10mm. However taking the front of the kidney is by far the worst case for the inverse square law and performing a similar calculation for the centre of the kidney phantom (47mm diameter) yields a reduction by a factor 5. This is somewhat larger than the observed reduction of 3.9 and may be explained by considering the geometry of figure 3.7.1: When the phantom is 30mm deep more phantom is seen by both collimators than when the phantom is 10mm deep. This decreases the expected reduction in signal. The variation of

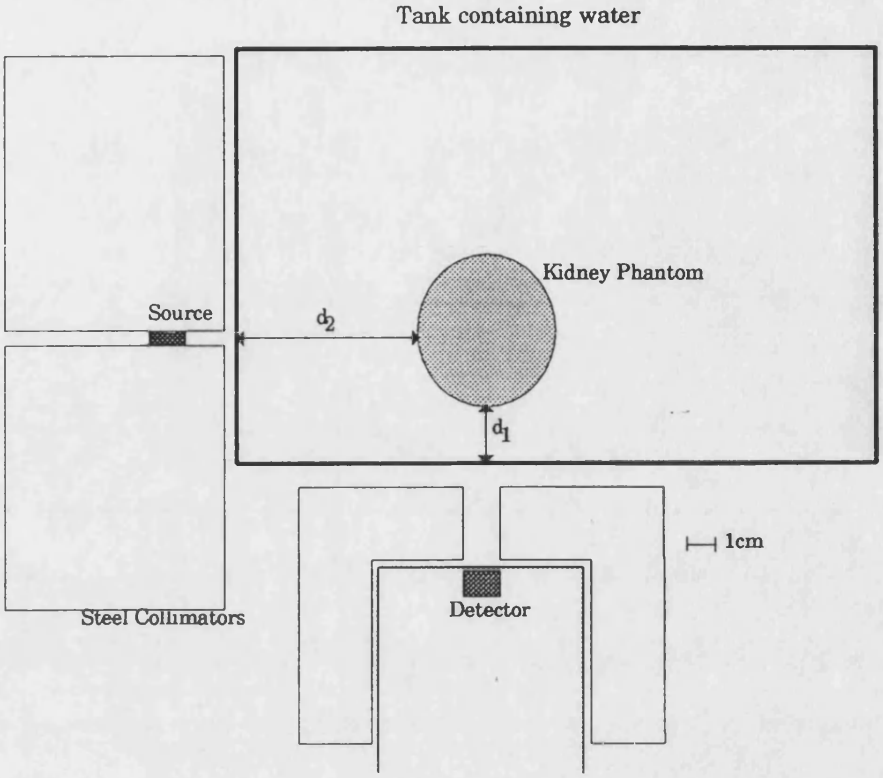

Figure 3.7.2 - Diagram of experimental arrangement for ^{57}Co work

the signal with depth of kidney phantom thus can be explained, at least partly, by a simple consideration of the basic underlying physical processes.

3.7.2 ^{57}Co in a 90° geometry

A similar set of experiments were performed using a ^{57}Co source in a 90° geometry. however there are now two depths that can be varied. i.e. the depth with respect to the detector, d_1, and the depth with respect to the source, d_2. The effect of varying both of these was investigated. A diagram of the experimental arrangement is shown in figure 3.7.2 and a summary of results is given in table 3.7.2.

Phantom Depth / mm		SSD	Peak Area
d_1	d_2	/ mm	/ Counts
20	20	20	1099±84
30	30	20	739±70

Table 3.7.2 - Results from the ^{57}Co 90° system geometry with different phantom depths. The skin dose for all the results is 5mGy and the peak areas are for the $K_{\alpha 1}$ peak only. The concentration of gold in the kidney phantom was 500μg g^{-1}

It is clear from these results that the sensitivity of the ^{57}Co system falls off less rapidly with depth than the ^{133}Xe system described above. This is partly attributable to the fact that the 122keV ^{57}Co photons are more penetrating than the 81keV ^{133}Xe photons. It is also partly attributable to the fact that ^{57}Co photons that have undergone low angle Compton scatter will still have enough energy to cause a photoelectric transition in gold whereas Compton scattered ^{133}Xe photons will in general not. However it is not possible to quantify the magnitude of the latter effect without a Monte Carlo type calculation, similar to that described in chapter 5.

3.7.3 Conclusions

It is concluded that the peak area falls off less quickly for the 90° type systems with higher energy sources such as the ^{57}Co results presented above. This phenomenon is attributed to two factors: Firstly the higher energy photons of the ^{57}Co source are more penetrating so more unscattered exciting photons reach the kidney phantom, and secondly that more of the higher energy ^{57}Co photons that have undergone Compton scattering will still be able to cause photoelectric transitions in gold. However it is not possible to predict the rate of decrease in sensitivity with increase in phantom depth for different energy sources.

3.8 Peak fitting program

The peak fitting program (given in Appendix A) was used to fit the region of the spectrum containing the gold fluorescence peaks. It was used to evaluate the area under the peaks (and hence for a calibrated system the concentration of gold could be deduced).

The program used a fitting function (described below) to fit both the background around the peaks (so that the background under the peaks could be interpolated) and the peaks themselves. The algorithm employed by the program was the non-linear least squares fit proposed by Levenberg and

Marquadt. (Press *et al*, 1988; Marquadt, 1963)

The function used to fit the peaks is given in equation 3.8.1. The general cubic part was used to fit the background as no analytical expression exists for the background due to multiple scattering. The two gaussian parts were used to represent the $K_{\alpha 1}$ and $K_{\alpha 2}$ peaks of gold with small underlying shelf due to incomplete charge collection represented by the complementary error functions (Varnell and Trishcuk, 1969).

$$y = a_1 \exp\left(\frac{-(x - a_2)^2}{2a_3^2}\right) + a_{11}\,\mathrm{erfc}\left(\frac{x - a_2}{\sqrt{2}\,a_3}\right) + a_4 a_1 \exp\left(\frac{-(x - (a_2 + a_5))^2}{2a_6^2}\right) + a_{11}\,\mathrm{erfc}\left(\frac{x - (a_2 + a_5)}{\sqrt{2}\,a_6}\right) + a_7 + a_8 x + a_9 x^2 + a_{10} x^3 \qquad (3.8.1)$$

where erfc represents the complementary error function given by equation 3.8.2 and a_1-a_{11} are the parameters adjusted by the fitting program.

$$\mathrm{erfc}(z) = 1 - \frac{2}{\sqrt{\pi}} \int_{-\infty}^{z} e^{-z^2} dz \qquad (3.8.2)$$

The parameters a_1-a_{11} have the physical interpretations given in table 3.8.1 and illustrated in figure 3.8.1.

Parameter	Interpretation
a_1	Height of $K_{\alpha 2}$ peak / Counts
a_4	Height of $K_{\alpha 1}$ peak / Height of $K_{\alpha 2}$ peak
a_2	Position of $K_{\alpha 2}$ peak / keV
a_5	Difference in energy between $K_{\alpha 1}$ and $K_{\alpha 2}$ peaks / keV
a_3	½WHM of $K_{\alpha 2}$ peak / keV
a_6	½WHM of $K_{\alpha 1}$ peak / keV
a_{11}	Height of shelf under peaks relative to their height
a_7-a_{10}	Coefficients of polynomial used to fit background under the peaks

Table 3.8.1 - Interpretation of fitting parameters

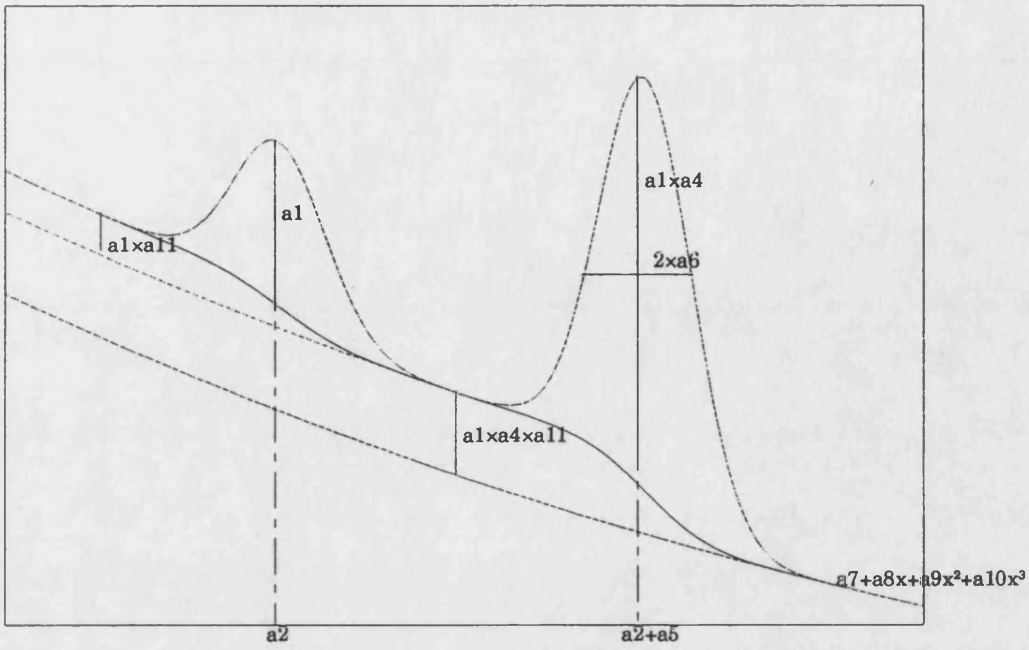

Figure 3.8.1 - Illustration of fitting parameters

In a typical fit parameters a_5, a_3, a_6, a_4 and a_{11} were fixed to the values predicted theoretically; a_5 is the theoretical separation of the two peaks, a_3 and a_6 are the detector resolution for the appropriate amplifier parameters (determined experimentally), a_4 is the relative heights of the $K_{\alpha 1}$ and $K_{\alpha 2}$ peaks and was set to the relative transition probability, and a_{11} is the experimentally determined height of the shelf for an ^{241}Am photon (59.5keV). (The method for the experimental determination is identical to that described in the caption to figure 2.4.1 except that an ^{241}Am source was used instead of a ^{57}Co source.) The other parameters were all allowed to vary freely. Initially a_2 was set to the expected position of the $K_{\alpha 2}$ peak; a_7-a_{10} were set such that the background was the cubic determined using the method described by Jonson *et al* (1988); and finally a_1 was estimated from the raw data using the estimated background.

3.9 Inter-laboratory comparisons

A study of published work suggests there are three other groups other than ourselves actively involved in using XRF for determination of trace levels of heavy metals in the kidney *in vivo* although none are investigating gold *in vivo*. These groups are based in Swansea, Birmingham and Göteburg (Sweden). The

following section compares the published results from these groups with our own preliminary work.

As detection limit is related to dose/time, a convenient measure of the potential sensitivity when comparing similar systems is to look at the peak area to background area ratio. This ratio should be independent of time, detector size and dose. The larger this ratio is the more potential the system has. However for a practical system the dose must not be ignored and an upper limit to the permissible dose is set depending on the diagnostic value of the investigation for the patient (WHO, 1977). It may be possible to have a system with a high peak to background area ratio and poor detection limit because of the high effective dose required to produce an acceptable photon count. This will be particularly true of highly collimated systems. Therefore it is also of interest to compare detection limits at similar skin doses, which are easy to measure and related to effective dose (Preface).

In order to compare different detection limits, with different quoted/measured skin doses, all results in the following discussion have been normalised to a skin dose of 4mGy. The detection limits were calculated assuming that detection limit decreases with increase in the square root of dose. It should also be noted that all detection limits quoted in this section are calculated from measurements obtained at higher concentrations using equation 3.2.7.

Examining table 3.9.1, which compares similar geometries with a ^{57}Co source from our own laboratory and Swansea (Dutton *et al*, 1985), it is noted that the systems appear to have different peak to background area ratios. This is

Group	Metal	Detector Area /mm^2	d_2* /mm	d_1* /mm	SSD /mm	Peak Area[1] / Back. Area	DL[§] / μg g^{-1}
Swansea	Pt	100	60	20	40	0.17	34
Bath	Au	78	60	20	40	0.10	76

* See figure 3.7.2 [1] Areas under $K_{\alpha 1}$ only
[§] Normalised to absorbed skin dose of 4mGy
Table 3.9.1 - Comparison of results from Swansea and our own work using a ^{57}Co source in a 90° geometry. The concentration of metal in the kidney phantom was 500μg g^{-1}

explained by the fact that although in both cases the arrangement was such that the volume seen by both collimators was nearly identical, in the case of the Swansea group the kidney phantom was larger in one dimension by a factor of approximately 1.6, the amount of metal in the phantom increasing in proportion. Thus although the normalised detection limit for the platinum system appears to be far superior, a number of factors contribute to this. Firstly the detector used in the platinum system was larger, this gives a detection limit reduction of 1.2 (calculated from the square root of the ratio of detector areas). Secondly the dose for the gold system is calculated rather than measured, a similar calculation for the platinum system yields a dose of 2.5mGy rather than the 1.8mGy quoted; this gives another factor of 1.2. As already mentioned the platinum system has an increased signal to background ratio due to the increased size of the phantom, this gives a further factor of 1.3. Overall these three factors will reduce the detection limit by a factor of 1.9 which would reduce the normalised detection limit for the gold system from 76 to 40μg g^{-1}, which is close to the 36μg g^{-1} quoted detection limit for the platinum system.

The Birmingham group have opted for a $^{99}Tc^{m}$ source in a backscatter arrangement for determination of platinum in the kidney (Todd, 1989). This type of system has also been adopted by the Swansea group for assessment of platinum in neck tumours although no detailed results have been published. A comparison of results from our own work (using the mark I xenon collimator) and the results from Birmingham is presented in table 3.9.2. No detection limit comparison is made because it is unclear how the TLD chips were positioned in

Group	Metal	Detector Area /mm²	Phantom Depth /mm	SSD /mm	Peak Area[1] / Back. Area
Birmingham	Pt	256	20	30	0.08
Bath	Au	78	20	30	0.09

[1] Areas under $K_{\alpha 1}$ only

Table 3.9.2 - Comparison of results from Birmingham and our own work using a $^{99}Tc^{m}$ source in a backscatter geometry. The concentration of metal in the kidney phantom was 500μg g^{-1}

the Birmingham dose determination.

Although it would have been preferable to have a comparison of detection limits between the two systems, especially as the quoted detection limit by the Birmingham group is 56μg g^{-1}, it is clear from the peak to background area ratios that the results are very similar. It should be noted that both ourselves and the Birmingham group used similar sized kidney phantoms and therefore it is valid to compare the peak to background area results directly.

The group working in Göteburg have been using an X-ray tube as an exciting source with both polarized and unpolarized photons. The use of an X-ray tube has allowed large source to skin distances and therefore has reduced the necessary dose. The disadvantages of using an X-ray tube are that some of the radiation incident on the patient can not excite fluorescence as it is too low in energy but it contributes to the overall dose. Also, if polarized X-ray photons are to be used then a very high photon flux is required before the polarizer and therefore a large amount of shielding is needed to protect the patient (and the detector) from stray radiation. This group has not published any raw data which allows a direct comparison to be made between their work and our own.

In conclusion, our results are similar to those obtained by other groups using similar techniques to investigate low levels of platinum in the kidney. However the amount of data that is available to make these comparisons is extremely limited.

3.10 Conclusions

In designing a system with optimum detection limit for typical kidney depths there are several parameters which may be varied. These are skin to source distance, detector to skin distance, degree of collimation, detector size, source energy and geometry. The effect of varying these parameters has been investigated in this chapter with the following conclusions:

3.10.1 Detector/source geometry

There are two types of geometry which have been commonly used: backscatter, where the source is mounted in a collimator which fits onto the front of the detector head, and other systems where independent collimation has been used for both source and detector. In the latter systems the angle between the source and detector axes is less than approximately 160° to accommodate both collimators. Angles less than 90° are excluded because of the rapid increase in the amount of tissue between the skin surface and the kidney at smaller angles (figure 3.10.1), and the 90° case has been investigated as an example of such a geometry. The inherent advantage of a backscatter system for gold detection is that a ^{133}Xe type system can be used where the fluorescence peaks are above the primary Compton scattering peak in energy. The large angle of scatter is needed to place the Compton scattered photons below the energy of the fluorescence photons. The inherent disadvantage is that it is difficult to well define the field of view of both collimators even when using a collimated point source rather than an almost uncollimated ring source. (Compare figures 3.4.1 and 3.10.2) The only inherent advantage of the 90° type system is that it is

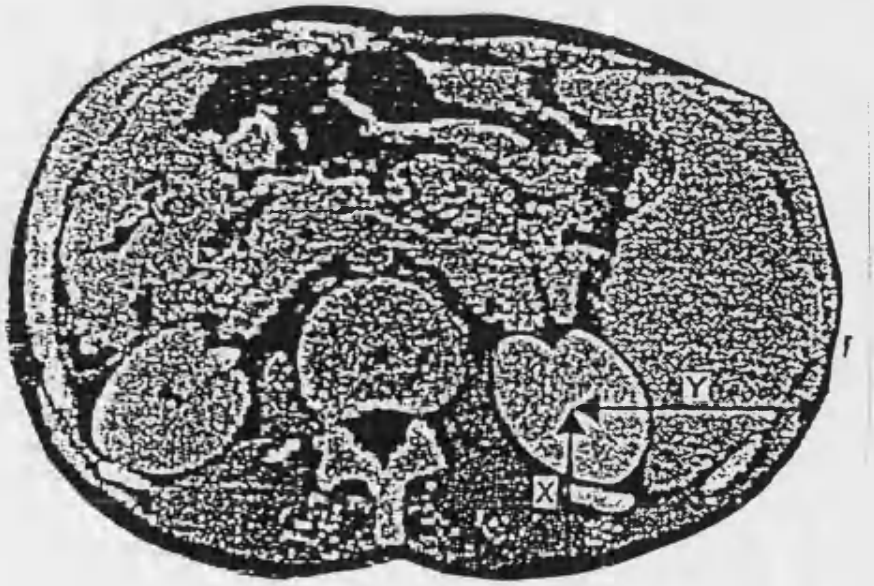

Figure 3.10.1 - Cross-section through body at kidney height

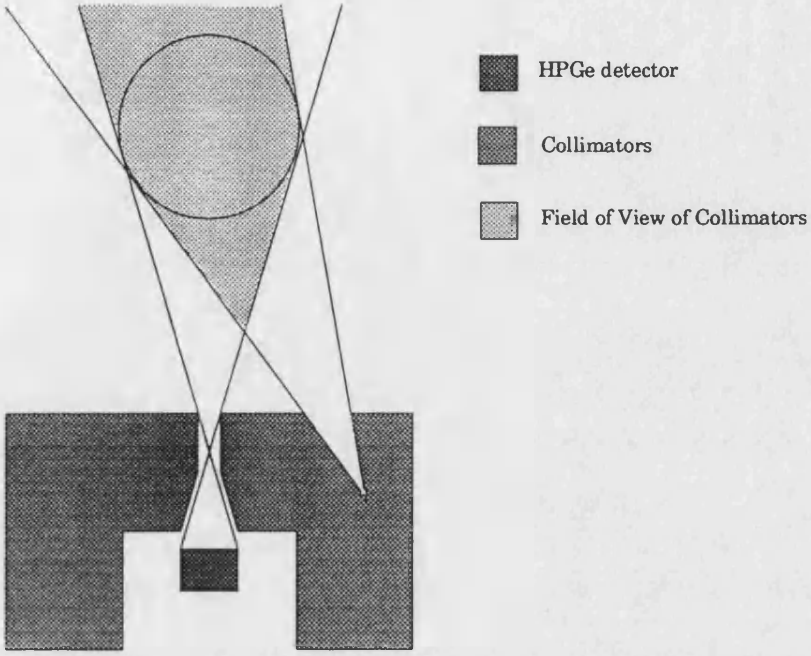

Figure 3.10.2 - Possible apparatus for backscatter geometry with a point source

relatively easy to well define the field of view of both collimators. Therefore no fluorescence radiation is detected from any other gold containing organ such as the skin or liver (Gottlieb *et al*, 1972; Bascó *et al*, 1988; Vernon-Roberts *et al*, 1976).

3.10.2 Collimation

The effects of source collimation discussed in section 3.4 lead to the conclusion that the highest peak to background area ratios are obtainable with very fine collimation. However the best peak to background area ratios do not necessarily lead to the lowest detection limits due to low count rate per unit skin dose and it appears that the optimum detection limits are achievable when the source just irradiates the kidney volume, thus obtaining the maximum number of counts in the fluorescence peaks. The detection limit proves to be not very sensitive to slightly poorer collimation due to the fact that it only increases with the square root of counts in the background and that the number of counts in the background increases less rapidly than the increase in

the total volume of scattering medium seen by both collimators. The effect of varying detector collimation has not been studied extensively. The limited amount of experimental work that has been carried out indicates that the effects and conclusions would be broadly similar to those for source collimation. (i.e. An optimum system will be achieved when the collimation is such that the detector just sees the kidney volume).

3.10.3 Detector size

Although for economic reasons the effect of varying detector size has not been investigated, it is anticipated that generally an increased detector size will lead to a reduced detection limit due to an increased count rate per unit skin dose. The only exception to this may be in a backscatter system with source very close in energy to the K absorption edge (^{133}Xe for gold or ^{109}Cd for lead) where the larger range of scattering angles accepted and consequent increase in width of the Compton peak and background below the fluorescence peaks may lead to an increased detection limit.

3.10.4 Source to skin distance

If the skin to source distance is made large with respect to kidney size and depth then the kidney receives a more uniform dose distribution and variation in sensitivity across the kidney is reduced. Large skin to source distances would however require a source with very high photon flux to maintain a reasonable count rate. However it should be noted that with large skin to source distances a much smaller error in angular alignment will cause the irradiating beam of photons to miss the kidney completely.

3.10.5 Detector to skin distance

The effects of varying detector to skin distance can be explained using the inverse square law. This leads to the conclusion that the detector should be placed as close as possible to the skin surface in order to maximise count rate.

3.10.6 Source energy

Varying the source energy has two effects: Firstly to change the cross section for absorption for the exciting photon by the gold and secondly the attenuation coefficient for the photon in tissue is different. Combining these two factors gives an indication as to whether the alternative source will improve or degrade system performance. It is not possible to use all source energies in all geometries due to the relative positions of the primary Compton scattering peak and the fluorescence peaks.

3.10.7 Kidney phantom depth

The effects of varying the kidney phantom depth can be explained to a great extent using both the inverse square law and simple attenuation of both fluorescence and incident photons in the overlying water. However as the linear attenuation coefficient is not independent of energy the effect of kidney phantom depth is not independent of source energy. The rate of increase in volume of scattering medium seen by the collimators with phantom depth is dependent on detector/source geometry and collimation. Thus the magnitude of the increase in detection limit with increase in phantom depth is not independent of collimation or detector/source geometry.

3.11 Design parameters for a clinical system

From the above discussion one may conclude that to produce an optimum system it is necessary to maximise skin to source distance while maintaining high photon flux; minimise detector to skin distance; maximise detector size (unless a ^{133}Xe type system is used); collimate such that the source and detector just see the kidney volume; and use a source of energy close to the absorption edge of gold (while bearing in mind that the primary Compton scattering peak should not be coincident with the fluorescence peaks).

The problem with a backscatter system is that increasing source to skin distance also increases detector to skin distance. Also if a ^{133}Xe type system is

used with the source surrounding the detector, increasing the detector size increases the count rate but also increases the relative height of the background underneath the fluorescence peak. Therefore an optimum backscatter system will be a compromise between competing requirements. However using an alternative geometry separates the source from the detector and allows the factors affecting detection limit to be optimised separately. Thus it is concluded that, although it is probably possible to achieve the desired detection limit of 40μg g^{-1} with any of the arrangements investigated with the target organ close to the skin surface, it is best to proceed with the 90° geometry as the target organ lies at a depth of 25mm or more. Another advantage of a 90° type system is that it is easy to tailor the collimation such that the fluorescence signal comes from the kidney and no other organ. It is therefore concluded that the best system to proceed with is a 90° geometry ^{153}Gd system as the field of view of the collimators can be well defined to cover only the kidney and no other gold containing organ. ^{153}Gd has a better cross section for absorption by the gold than ^{57}Co and is available in higher activities and therefore the source can be positioned some distance from the skin while keeping the detector as close as possible to the skin.

Chapter 4

^{153}Gd System

4.1 Introduction

In the conclusions to the last chapter a set of design parameters were proposed for a clinical system. The following work describes an evaluation of a prototype system based on these parameters.

4.2 The source

It was proposed in the last chapter that ^{153}Gd would prove to be a better source than ^{57}Co for studies using a 90° geometry. ^{153}Gd appears to give better detection limits than ^{57}Co, has a similar half life, lower cost per unit specific activity, and is available in higher activities. Unfortunately ^{153}Gd has strong emission of europium K X-rays (41-48keV, 110%) as well as emission lines at 97keV (30%) and 103keV (20%). These europium K X-rays would give an absorbed radiation dose to the patient without inducing any fluorescence of the K lines of gold, and would also cause unnecessary dead-time in the detector by causing extra counts. It is however possible to filter the beam emerging from the source capsule to very significantly reduce the intensity of these very low energy photons. In order that only 10% of the incident photons have no chance of exciting fluorescence, the intensity of the photons with energy around 100keV should be approximately ten times the intensity of europium K X-ray photons (44keV). The appropriate attenuation coefficients of three possible filtration materials with widely varying atomic number are given in table 4.2.1 (Hubbell, 1982). The ratio of intensities, η, from a filtered source is given by equation 4.2.1

$$\eta = \frac{50\, e^{-\mu_{100} x}}{110\, e^{-\mu_{50} x}} \qquad (4.2.1)$$

where x is the thickness of the filter and μ_{100} and μ_{50} are the linear attenuation coefficients for the material at 100keV and 50keV respectively.

Material	μ/ρ at 50keV /m^2 kg^{-1}	μ/ρ at 100keV / m^2 kg	ρ / kg m^{-3}
Al	3.66×10^{-2}	1.70×10^{-2}	2700
Fe	1.94×10^{-1}	3.70×10^{-2}	7860
U	1.12×10^{-1}	1.95×10^{-1}	18950

Table 4.2.1 - Mass attenuation coefficients (μ/ρ) and density (ρ)

Therefore the thickness of the filter that is required to give η=10 can be calculated from equation 4.2.2

$$x = \frac{\ln 22}{\mu_{50} - \mu_{100}} \qquad (4.2.2)$$

These thicknesses are given in table 4.2.2, for the possible filter materials given in table 4.2.1, together with the proportion of photons with energy of 97keV or 103keV transmitted. Thus it can be concluded that a 2.4mm iron filter would be suitable. uranium gives a slightly higher flux of unattenuated 97 or 103keV photons for a filter thickness such that η=10 than iron due to its high atomic number. However, the advantage of uranium over iron is insignificant and not worth the extra expense that would be incurred and inconvenience of using an alpha particle emitter. The emission spectra of a ^{153}Gd both pre and post filtration with a 2.4mm iron filter can be seen in figure 4.2.1. These experimental results agree well with the photon intensities predicted by equation 4.2.1.

4.3 Collimation

The conclusions from the previous chapter were that the optimum collimation system was when both the source and detector could just 'see' the kidney. A detector collimator to this design had already been built and successfully tested

Material	Thickness / mm	Unscattered 97 and 103keV photons / %
Al	58.5	7
Fe	2.4	48
U	0.18	51

Table 4.2.2 - Thickness of filter required for η=10

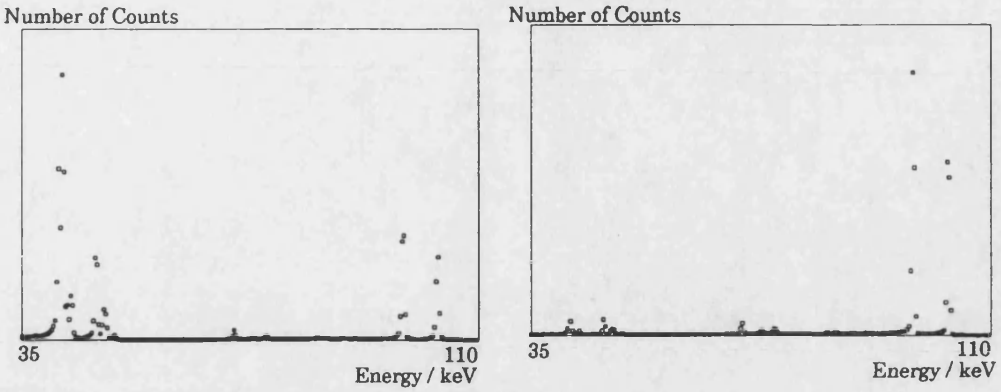

Figure 4.2.1 -Spectra from ^{153}Gd source both before (left) and after (right) filtration with 2.4mm of steel

(as described in the previous chapter). A collimator along similar lines was built for the ^{153}Gd source with an active diameter of 3mm in a X1041 capsule, as supplied by Amersham International, and is illustrated in figure 4.3.1. The design allowed for two alternative source to kidney centre distances: these were 95mm and 130mm, the larger distance required additional collimation and therefore the addition of the extra collimating plate illustrated in figure 4.3.1. These distances were chosen such that two alternative source to skin distances could be evaluated, which were 20mm and 45mm, with a typical kidney depth, that would be found using this geometry, of 50mm. An additional blanking plate was also made for the collimator, so that source could be stored without removing it from the collimator.

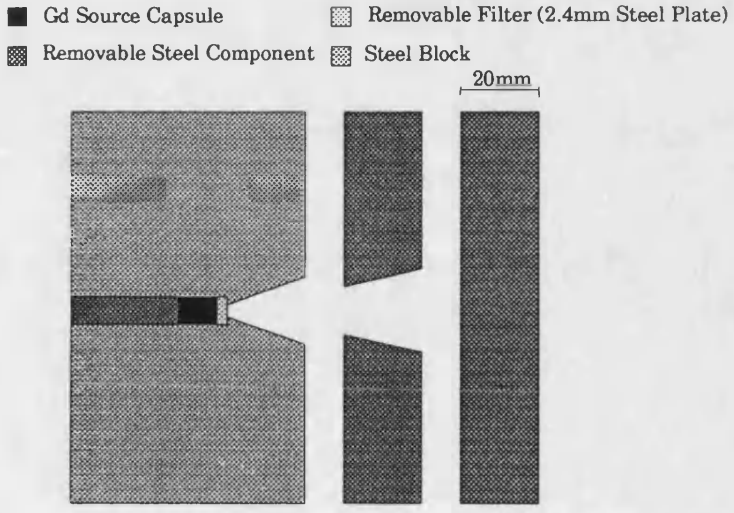

Figure 4.3.1 - Scale diagram of ^{153}Gd collimator

Collimator	$K_{\alpha 1}$ Peak / Counts	DL / $\mu g\ g^{-1}$
New	1886±145	102
Old	1587±165	142

Table 4.3.1 - Summary of results comparing old and new source collimators with ^{57}Co source since ^{153}Gd source would not fit into the old source collimator

A comparison of the results obtained using this source collimator was made with those obtained with the old source collimator in similar experimental arrangements. A summary of the experimental results is given in table 4.3.1. From these results it can be clearly seen that the new collimator is superior in performance to the old source collimator, since improved detection levels are achieved with the same absorbed dose at the skin.

4.4 Dosimetry

There are three measures of radiation dose: absorbed dose which is simply the energy absorbed per unit mass (SI unit - Gray); equivalent dose which takes into account the biological effect of the type of radiation being used (SI unit - Sievert); and effective dose which is calculated by summing the products of the equivalent dose contributions and their respective weighting factors for different organs (SI unit - Sievert (as well!)). Equivalent dose, H_T, is the product of absorbed dose, D, and the radiation weighting factor, w_R, for the type of radiation being used (shown in table 4.4.1), as given by equation 4.4.1. It is these dose equivalents, that are used to calculate the effective dose, H_E, using equation 4.4.2, together with the tissue weighting factors, w_T, given in table 4.4.2. Dose limitations are usually defined in terms of the effective dose, however it is the absorbed dose of a particular organ that is usually measured or calculated.

$$H_T = w_R D \tag{4.4.1}$$

$$H_E = \sum_i w_{T_i} H_{T_i} \tag{4.4.2}$$

When calculating effective dose, using the tissue weighting factors given in table 4.4.2, it should be noted that the tissue weighting factor for "other"

Radiation Type	w_R
α	20
β, Electron	1
γ	1
X-ray	1
Muon	1
Proton (>2MeV)	5
Neutron	5-20

Table 4.4.1 - Radiation weighting factors for different radiation types

Organ	w_T
Gonads	0.20
Red bone marrow, Colon, Lungs, & Stomach	0.12 each
Bladder, Breast, Liver, Oesophagus, & Thyroid	0.05 each
Bone Surfaces, & Skin	0.01 each
Other	0.05

Table 4.4.2 - Tissue weighting factors for different organs

organs is composed of the adrenals, the brain, the small intestine, the kidneys, muscle, the pancreas, the spleen, the thymus and the uterus. The recommendations, given in ICRP report 60 (ICRP, 1990) also state *"In those exceptional cases in which a single one of the other organs receives an equivalent dose in excess of the highest dose in any of the twelve tissues or organs for which an* (individual) *weighting factor is specified, a weighting factor of 0.025 should be applied to that tissue or organ and a weighting factor of 0.025 to the average dose in the rest of the other organs as defined above."*

With regard to skin dose the recommendations state that provided the maximum skin equivalent dose does not exceed that required to cause deterministic effects (0.5Sv y^{-1}), the skin dose may be averaged over the whole skin surface. This, coupled with the relatively small weighting factor for the skin (0.01), makes the contribution of skin dose to the equivalent dose for an X-ray fluorescence investigation small. Nevertheless the maximum skin dose is a useful quantity since it can be measured directly or calculated using the dose rate constant. An approximate value for the kidney dose can be calculated allowing both for the attenuation effects of the overlying tissue, and of the inverse square law (since the kidney is further from the source than the skin).

It is possible to calculate the skin dose received from an isotope source at any distance from the source using the dose rate constant, Γ. This is defined in ICRU report 33 and has dimensions of Sv m^2 h^{-1} Bq^{-1}. The equivalent dose, H_T, received from a source of activity A, at distance x, over a period of T hours is

given by equation 4.4.3.

$$H_T = \frac{\Gamma A T}{x^2} \qquad (4.4.3)$$

The value of the dose rate constant, Γ, is *"a characteristic of a radio-nuclide* (and) *is defined for an ideal point source. In a source of finite size, attenuation and scattering occur and annihilation radiation and external bremsstrahlung may be produced. In some cases these processes necessitate significant corrections."* (ICRU 33, 1980). Therefore it is clear that any calculation made using a published value of the dose rate constant, Γ, will contain a degree of uncertainty since the sources used are not perfect point sources and are contained in a metallic capsules which will cause a degree of attenuation.

4.4.1 Thermoluminescence Dosimetry

Since dose rate constants are not available for all radio-isotopes and none that have been filtered such as the ^{153}Gd described above, it is necessary to have a method of measuring dose experimentally. The method usually employed is thermoluminescence dosimetry (TLD). A large number of materials exhibit radio-thermoluminescence. In this process light is emitted from a previously irradiated material when it is heated, by the release of electrons from traps in the lattice. The intensity of the emitted light is related to the dose of radiation absorbed by the material and this property is utilised to measure absorbed radiation doses.

The technique is relatively simple requiring a suitable dosimeter material, a controllable heating mechanism, and a light collection and recording system. Photomultiplier tubes with a low response to infrared radiation are used to detect the low levels of light emitted by the thermoluminescence detectors. The plot of emitted light intensity as a function of temperature or time is called the glow curve. The glow curves of radio-thermoluminescent materials contain many glow peaks, corresponding to different traps depths each occurring at a different temperature. The glow peak temperature depends on several factors,

for example it increases with heating rate. For ease of measurement and simple thermal treatment, a single well-resolved and stable peak is generally required. With low temperature peaks the thermoluminescence signal may reduce or fade during storage or use of the material and with high temperature peaks non-radiation induced signals may increase the background or zero dose response of the dosimeter material. Therefore a glow peak in the temperature range 190°C to 240°C is usually used.

Of the thousands of materials which exhibit thermoluminescence, only four with low effective atomic, Z, similar to that of tissue are commonly used in applied radiation dosimetry. These are lithium fluoride (LiF), lithium borate ($Li_2B_4O_7$), beryllium oxide (BeO) and magnesium borate (MgB_4O_7). These materials are doped with various activators which characterise the thermoluminescence properties of each material. For example $Li_2B_4O_7$ doped with copper gives a blue luminescence and high sensitivity, but when doped with manganese gives an orange luminescence and consequently a low sensitivity, due to the low sensitivity of the photomultiplier tubes at the red end of the spectrum.

Impurities and intrinsic defects such as vacant atomic sites are crucial to the thermoluminescence process. The impurity additions to the host material therefore need to be controlled to give optimum performance. The phenomenon of radio-thermoluminescence is basically a three stage process. In the first stage free electrons and holes are produced by irradiation. In the second stage some of these free carriers become trapped in the field potential of certain defects. The more tightly bound carriers require more energy (higher temperatures) to release them. In the third stage some of the electrons released from the traps recombine with the holes releasing the excess energy in the form of light. The plot of light intensity against absorbed dose gives the dose response curve of the irradiated material, generally the shape of this curve is linear up to about 5Gy. Weakly bound charge carriers are released easily from

Material	Sensitivity Φ / kg^{-1}	Dose Threshold D_0 / µGy	Fading Factor Ψ / %
BeO	0.2-1	<100	5 (in 1 to 5m)*
$Li_2B_4O_7$:Cu	2	10	<5 (in 10d) *
$Li_2B_4O_7$:Mn	0.2	50-100	<5 (in 1m)
LiF(TLD100)	1	50	5 (in 1y)
LiF:Mg,Cu,P	20	-	5 (in 2m)
MgB_4O_7:Dy	5-10	20-50	<5 (in 1m) *

Ψ fading in the dark per year (y), month (m) or day (d)
* Light sensitive
Φ for ^{137}Cs, relative to TLD100
Table 4.4.3 - Properties of some commercially available TLDs

trapping centres and therefore lead to low temperature glow peaks which fade relatively quickly at room temperature. These weakly bound charge carriers are therefore deliberately released in a preliminary low temperature (120°C) part of the heating cycle before counting of the luminescent photons begins. The properties of some commercially available TLD chips are given in table 4.4.3.

4.4.2 Calibration of TLD Chips

When using TLD chips it is necessary to calibrate one set by irradiating them with a known dose of radiation of equivalent energy to the source under test. This can be a problem if no calibrated source exists. However it is usually possible to use a source with a different energy profile to the one under test because most chips have a reasonably flat energy response. A typical energy response curve for TLD chips is shown in figure 4.4.1.

The sources used for calibration were X-ray therapy units, which had been calibrated using an NPL secondary standard ionisation chamber. These are inherently broadband sources which have a spectral output of similar shape to that shown in figure 4.4.2. In order to determine a calibration for TLD chips when using a single energy photon source such as the filtered ^{153}Gd described above, the logical approach is to use an X-ray source from which the peak photon count is of similar energy to the energy required. An inspection of X-ray spectra such as the one illustrated in figure 4.4.2, leads to the conclusion that

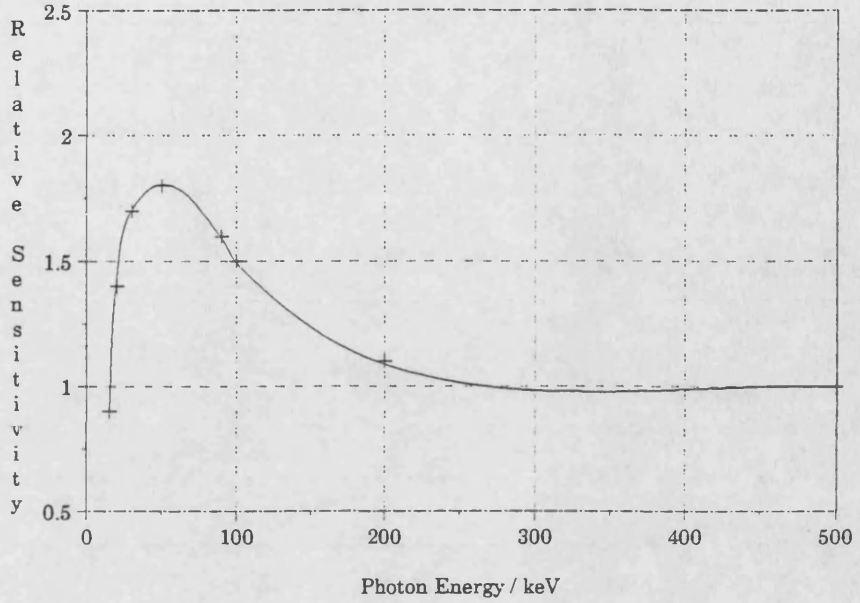

Figure 4.4.1 - Plot of sensitivity against energy for Vinten LiF TLD chips

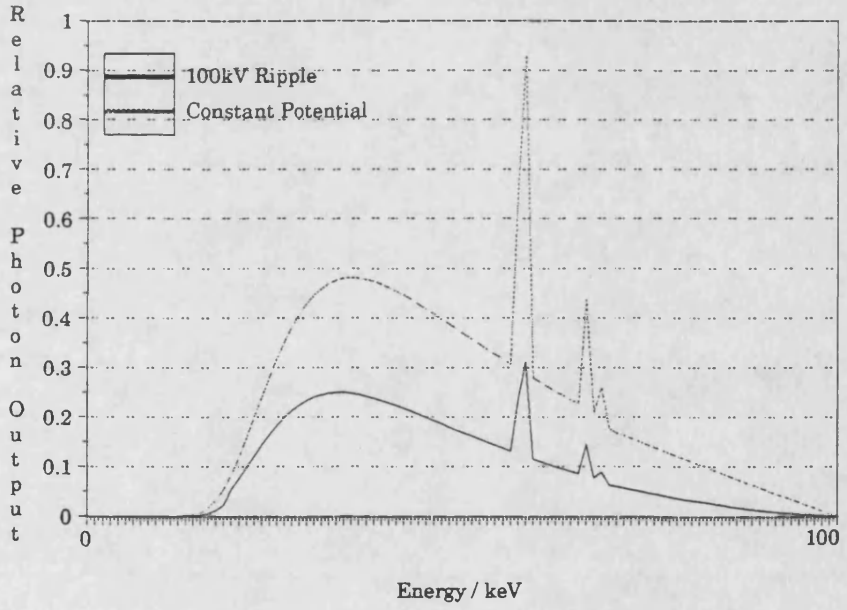

Figure 4.4.2 - Typical spectral output from an X-ray source

the peak photon count (in the bremsstrahlung) occurs at approximately one third the peak energy. The calibrated sources that were available locally had peak energies of 120keV, 250keV and 6MeV. Therefore the most appropriate was the 250kV source, however all three were used to give some idea of the possible error introduced into the calibration from the variation in sensitivity of

the TLD chips with energy. Figure 4.4.1 would indicate that the TLD chips would be more sensitive at the lower X-ray energies than at 6MeV. This was confirmed in the experimental work described below.

4.4.3 TLD Experimental Work

In order to estimate the absorbed doses at different tissue sites with alternative experimental arrangements, it is useful to know the value of the dose rate constant for the source and capsule being used. This value will allow for the factors mentioned in section 4.4, such as the fact that the source is not a point, but distributed within a metallic capsule. Therefore the effective dose rate constants for both our ^{57}Co and the filtered ^{153}Gd were determined experimentally using LiF TLD chips supplied by Vinten. These chips were annealed at 300°C for 1 hour and then 80°C for 16 hours (Harshaw TLD100 [used later in the project] - 400°C for 1 hour followed by 80°C for 16 hours), put in small sachets (three chips in each). Calibration of the TLD chips was performed using the Varian Clinac 6MeV linear accelerator, the Philips RT250 250kV ortho-voltage therapy X-ray set, and the Therapax Series 3 superficial treatment X-ray set at the Royal United Hospital in Bath, whose outputs had been calibrated using an NPL secondary standard dosimeter. Two sachets were exposed on each machine. Three sachets were also left unirradiated as a determination of the background. In order to experimentally determine the dose rate constants for both ^{57}Co and filtered ^{153}Gd, two sets of two sachets were affixed to a small water bath (180 × 110mm) to represent the phantom arrangement used in previous experimental arrangements to represent the human body. These sets of two sachets were then irradiated for 92 hours, one using the 35MBq ^{57}Co source used in earlier work and the other using a 63MBq ^{153}Gd filtered with 2.4mm of steel. The sources were positioned at a distance of 50mm from the water bath.

The results read out from the TLD reader (Vinten Toledo 654) are given in tables 4.4.4 (calibration) and 4.4.5 (isotope source results). The calibration

Radiation Source	Average Counts	C.V.* / %	Dose / mGy	Calib. Factor / Counts mGy^{-1}
Clinac	48639	2.4 (n=6)	40.3	1206
RT250	59983	1.9 (n=5)	42.3	1418
Therapax	65292	2.1 (n=6)	41.0	1592
Background	559	19.6 (n=9)	-	-

*C.V. - Coefficient of variation over n results
Table 4.4.4 - Calibration results from TLD experimental work

Radiation Source	Average Counts	C.V.* / %	Skin Dose D_{RT250} / mGy
^{57}Co	33678	2.1 (n=6)	24.0
$^{153}Gd(Fe)$	18374	4.3 (n=4)	13.1

*C.V. - Coefficient of Variation over n results
Table 4.4.5 - Results from TLD work with ^{57}Co and ^{153}Gd

factors given in table 4.4.4 have a coefficient of variation of only 10% about their mean (1405 counts mGy^{-1}). Therefore if the RT250 calibration factor is used to determine the doses for the isotope sources, which is the most appropriate for the reasons discussed in section 4.4.2, the error in the doses deduced in table 4.4.5 is unlikely to exceed 5%. The analysis of these results gives a value of the dose rate constant, Γ, for ^{57}Co $\Gamma=18\pm1\mu Sv\ m^2\ h^{-1}\ GBq^{-1}$, using the RT250 calibration. It should be noted that the absorbed dose, D, has been converted to equivalent dose, H_T, using the unity radiation weighting factor, w_R, for γ-radiation in equation 4.4.1. This value of the dose rate constant lies between the published values for ^{57}Co of $\Gamma=15\mu Sv\ m^2\ h^{-1}\ GBq^{-1}$ (Siemens,1991) and $\Gamma=22\mu Sv\ m^2\ h^{-1}\ GBq^{-1}$ (Padikal and Fivozinksy, 1982). There are three factors which may lead to the experimentally determined values of the dose rate constant disagreeing with the calculated published values. Firstly the calculated value does not allow for the absorption of photons backscattered from the water bath, which will increase the dose absorbed by the TLD chips. Secondly the calculated value does not allow for the fact that the source is contained in a metallic capsule which will attenuate the photon flux by around 5%, and thirdly the source is not a perfect point source. The fact that the source is not a perfect point source will only be a small effect since the active area of the source is small (2mm diameter) and very thin (less than

100μm). Therefore there is an insignificant amount (estimated as less than 2%) of self attenuation of the source in the forward direction due to the finite thickness of the source.

The values of the dose rate constant for the filtered ^{153}Gd source that was calculated from the experimental results above is Γ=5.7±0.3μSv m^2 h^{-1} GBq^{-1}. For future work on filtered ^{153}Gd systems this value of the dose rate constant based on the RT250 calibration will be used to calculate skin doses, for the reasons discussed in section 4.4.1 and supported by the work for the ^{57}Co result described above.

It also possible to calculate a value of the dose rate constant, Γ, in air using the following method. It is known that the rate of energy loss with distance, x, to a medium of energy absorption coefficient, μ_E, is given by equation 4.4.4; where E is the energy of the photons.

$$\frac{dE}{dx} = E\mu_E \qquad (4.4.4)$$

Therefore the rate of energy loss, with distance, to a medium from a point source of activity, A, over a period of time, T, is given by equation 4.4.5; where n_i is the number of photons of energy, E_i, per disintegration and μ_{E_i} is the energy absorption coefficient at that energy.

$$\frac{dE}{dx} = \sum_i E_i \mu_{E_i} n_i AT \qquad (4.4.5)$$

As the source is a point source, this energy is being lost to a spherical shell of radius, x, and mass, dm, given by equation 4.4.6; where ρ is the density of the medium.

$$dm = 4\pi\rho x^2 dx \qquad (4.4.6)$$

Therefore the rate of energy loss per unit mass, which is equivalent dose, H_T, for γ-rays, is given by equation 4.4.7.

$$H_T = \sum_i \frac{E_i \mu_{E_i} n_i AT}{4\pi\rho x^2} \qquad (4.4.7)$$

Using equation 4.4.3 an expression for the dose rate constant, Γ, can now be obtained, and is given by equation 4.4.8.

$$\Gamma = \sum_i \frac{E_i \mu_{E_i} n_i}{4\pi\rho} \qquad (4.4.8)$$

A more useful form of equation 4.4.8 is given by equation 4.4.9; where e is the elementary charge; the photon energy, E_i, is in keV; and the dose rate constant, Γ, is in $\mu Sv\ m^2\ GBq^{-1}\ h^{-1}$.

$$\Gamma = \frac{9e \times 10^{20}}{\pi} \sum_i E_i n_i \frac{\mu_{E_i}}{\rho} \qquad (4.4.9)$$

Using equation 4.4.9 a value of the dose rate constant for ^{57}Co in air of $\Gamma = 19\mu Sv\ m^2\ GBq^{-1}\ h^{-1}$ is obtained, which is in agreement with both the tabulated and measured values.

4.5 Evaluation of a ^{153}Gd system

Now that an effective dose rate constant for the ^{153}Gd source had been determined, an evaluation, including the resultant dose consequences, of an X-ray fluorescence system based on a ^{153}Gd could be undertaken. The optimum design parameters for such a system were discussed and demonstrated to be correct in chapter 3 and sections 4.2 & 4.3. The experimental arrangement shown in figure 4.5.1 was adopted. The kidney was represented by a small (150ml) polythene bottle which was 47mm diameter and filled with chloroauric acid such that the concentration of gold was $500\mu g\ g^{-1}$. This kidney phantom was placed in a water bath that was 210mm × 150mm to represent the surrounding tissue. The source and detector were collimated such that they could just 'see' the kidney phantom as described in section 4.3. In order to

maximise the count rate, the detector collimator was placed against the water bath. So that the kidney phantom just filled the field of view, the source collimator was placed such that source was 20mm from the surface of the water bath (75mm from the kidney surface). The ^{153}Gd source, which had been removed from a Novo bone densitometer based at the RNHRD (Bath), had an activity of 1.6GBq. The dose rate at the skin surface from this source was therefore 22mGy h^{-1}. In a further experiment the source collimator was moved a further 20mm away from the water bath, to reduce the skin dose compared to the kidney dose, such that the source to kidney surface distance was 95mm. The additional collimation plate was added to the front of the collimator for this experiment so that the kidney phantom, again, just filled the field of view of the source collimator. The dose rate at the skin was consequently reduced to 4.4mGy h^{-1}. A summary of the results from this preliminary work is given in table 4.5.1. All the results in the table were for a skin dose of 8mGy assuming the dose rate constants given at the end of section 4.4 are correct.

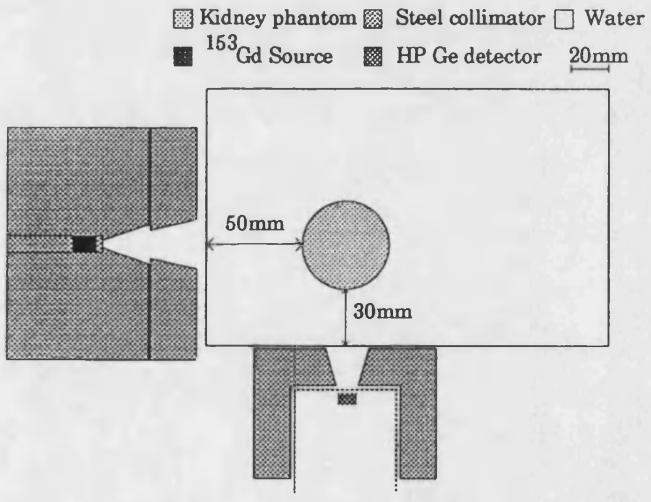

Figure 4.5.1 - Scale diagram of apparatus for evaluation of ^{153}Gd based system

SSD /mm	Irradiation Time / s	$K_{\alpha 1}$ Peak / Counts	DL / μg g^{-1}
45	6000	2718±165	76
20	1200	1476±120	103

Table 4.5.1 - Summary of results of preliminary evaluation of ^{153}Gd based system

Examination of these results leads to the conclusion that even if the source is positioned at a distance from the skin, the required detection level can not be achieved with the current detector and source, in an acceptably short irradiation time. However for the desired detection level to be achieved a larger detector could be used, thus increasing the count rate per unit dose. The forecast improvements for larger source and detector are discussed in section 4.7.

4.6 Alignment Uncertainties

It is obviously important to be aware of any variation that could be introduced into the results by misaligning both source and detector collimators. Potentially the errors involved are likely to be significant because of the relatively small detector to kidney and source to kidney distances. Therefore a study was undertaken in order to assess the reproducibility of the results from slight differences in alignment. In order to assess the system component(s) that led to the largest errors, a four stage study was undertaken. In the first stage (stage I) only the source collimator was repositioned between spectra. In the second stage (stage II) the source collimator and the phantoms were repositioned between measurements and in the third stage (stage III) all the system components were repositioned between measurements. In the fourth stage (stage IV) no system components were repositioned in order to find the statistical variation in the results. It was found that this variation was of the order of $1/\sqrt{N_P}$ which is the variation that would be predicted theoretically for the number of counts in the peak, N_P. The variation found in stage IV indicated that the fitting program was not introducing a significant amount of uncertainty into the size of the peaks. In each stage of the study three separate

Stage	Coefficient of Variation / %	Average $K_{\alpha 1}$ Peak / Counts
I	10	1201
II	8	1153
III	9	1100
IV	3	1251

Table 4.6.1 - Summary of results from first reproducibility study

Stage	Average $K_{\alpha 1}$ Peak / Counts	C.V.* / %	Average Background beneath $K_{\alpha 1}$ / Counts	C.V.* / %
I	20680	2.4	206387	1.8
II	21351	8.0	211539	1.4
III	21627	8.1	204745	1.2
IV	20755	1.2	205537	1.6

* C.V. - Coefficient of Variation
Table 4.6.2 - Summary of results from second reproducibility study

spectra were taken and the coefficient of variation due to the system component in question was calculated. A summary of the results from these experiments is given in table 4.6.1. These results show that alignment problems are leading to poor reproducibility. To try and improve the reproducibility in the laboratory apparatus the whole apparatus was positioned on a piece of graph paper glued to a wooden base, and pieces of acetate sheet showing the direction of the field of view were attached to the bottom of the collimators. The results after this improvement are shown in table 4.6.2. It can be seen that these improvements generally led to significant improvements in reproducibility and emphasised the need for both accurate positioning in a clinical system and accurate kidney depth determination. The latter point being made by the large increase in coefficient of variation of peak counts between stages I and II, without an increase in coefficient of variation of the number of counts beneath the peak; thus indicating the variation came from the relative position of the kidney phantom in the water bath, rather than the absolute position of the water bath.

In a further experiment the effect of misalignment was assessed. The source collimator was deliberately positioned so that the centre of the irradiating beam was not coincident with the centre of the kidney phantom by a known distance. The experimental arrangement is illustrated in figure 4.5.1. This was repeated for each distance three times and a summary of results is given in table 4.6.3. From these results it can be seen there was a marked decrease in sensitivity when the part of the kidney phantom nearest the detector was not irradiated. This is as would be expected from inverse square law and

Misalignment * / mm	Average $K_{\alpha 1}$ Peak / Counts	Coefficient of Variation / %
-9	4055	4
0	4007	4
+3	3615	5
+6	3330	3
+9	2661	3

* The source collimator was moved parallel to the detector axis. A negative number indicates that the source was moved towards the detector.

Table 4.6.3 - Summary of misalignment study results

attenuation considerations as discussed briefly in the previous chapter. (A more thorough theoretical consideration of sensitivity variation with different parameters will be given in chapter 5.) Therefore in any clinical system, assuming that the gold is uniformly distributed in the kidney, it will be important to make sure the part of the kidney nearest the detector is irradiated, so as to maximise the fluorescence signal detected and also to give reproducible results.

4.7 Clinical system performance: predictions

From the preliminary experimental results above it is possible to make some predictions about the performance of a prototype clinical system. These predictions will allow the performance of this system to be compared with other systems described in later chapters. For simplicity these predictions will be made for a single kidney depth which is 50mm of overlying tissue between the source and the kidney surface and 30mm of overlying tissue between the detector and the kidney surface. In the introduction it was stated that for the system to be clinically useful the detection limit must be below 40μg g^{-1}. Therefore in order to make a comparison with other systems, the absorbed dose that would be required to give this detection limit will be estimated. Another limitation of an isotope based system is the activity of the isotope that would be required to give the required detection limit in 30 minutes, since this is the maximum acceptable time for patient studies. Therefore the activity required will also be estimated.

SSD /mm	Skin Absorbed Dose / mGy	Minimum Source Activity / GBq
20	9	1.2
45	3	2.0

Table 4.7.1 - Anticipated skin doses required with 32mm diameter detector to obtain detection limit of 40μg g^{-1}

It was anticipated that before a clinical system was constructed a larger detector (32mm diameter) would be purchased. This would give a higher count rate per unit time and therefore a reduced detection limit. It was anticipated that this would reduce the detection limits by approximately a factor of three, since due to the Poisson nature of the counting process involved the detection limit decreases with the square root of the number of counts collected, and the number of counts collected per unit time increases approximately with detector area. Table 4.7.1 therefore contains the prediction of system performance (i.e. absorbed skin and kidney doses required to obtain a detection limit of 40μg g^{-1}) using a 32mm diameter detector for both of the different source to skin/kidney distances used in the experimental apparatus described in section 4.4.3. It also gives the minimum activity of ^{153}Gd that would be required in each case for an irradiation time not exceeding 30 minutes.

Examining the results in table 4.7.1 it is clear that the required detection levels can be achieved at skin doses of a few milligray. This skin dose is well within those used in normal diagnostic investigations. The activity of source required is also well within that available; a ^{153}Gd source for a bone densitometer when new is typically 37GBq. Therefore it was anticipated that a system based on ^{153}Gd with a 32mm diameter detector would be suitable for measuring gold concentrations *in vivo*.

Chapter 5

Sensitivity Variation

5.1 Introduction

Ahlgren and Mattsson (1981) reported a marked variation in sensitivity with depth with their cadmium X-ray fluorescence system, using a ^{241}Am source (59keV). This would be significant from a calibration point of view for any X-ray fluorescence. Therefore both an experimental study and computer modelling were carried out in order to confirm the magnitude of these effects with our higher energy system, and predict variation in sensitivity for different kidney positions.

The processes that are involved and need to be considered for any computer model are the inverse square reduction in photon intensity with distance, or appropriate form for a non-point source, and photon attenuation due to overlying tissue.

5.2 Sensitivity variation in air

In the first instance a computer model was written with no attenuation due to overlying tissue. The predictions from this model could then be compared with the results obtained from measuring the fluorescence signal from a small gold-plated ball at various positions, in the plane containing the centre of the detector and the source, in air.

In air, it is assumed that there will be insignificant scatter of the 100keV exciting photons. This is reasonable since using the absorption coefficient ($\mu=1.54\times10^{-2}m^2\,kg^{-1}$, Hubbell (1982)) in equation 5.2.1, it can be seen that less than 0.2% of the photons undergo an interaction in a distance of 100mm in dry air. Since the scatter of photons is insignificant, all photons reaching the gold-plated ball will have similar energy and thus similar cross-section for absorption. Therefore the only factor that needs to be considered in the computer model is the inverse square reduction in intensity.

$$I = I_0 e^{-\mu r} \qquad (5.2.1)$$

Also included in the model must be geometrical factors from the experimental arrangement. These factors include relative positions and collimation of the source and detector. The ^{153}Gd source is physically small and can therefore on the scale of this experiment be considered as a point source. Therefore the sensitivity fall off from the source should be modelled by the inverse square relation. Since the detector is extended in size there will be a large penumbra effect that will also need to be included in the model.

5.2.1 Computer model

A diagram of the arrangement modelled, together with some of the distances used in the model is given in figure 5.2.1. The sensitivity is assumed to vary with the inverse square of the distance from the source to the gold-plated ball (r) and with the inverse square of the distance from the ball to the detector (R). Any point that could not be seen by either the detector or the source due to collimation was ignored. Each point was assumed to have a sensitivity in proportion to the fraction of both source and detector that could be seen by it,

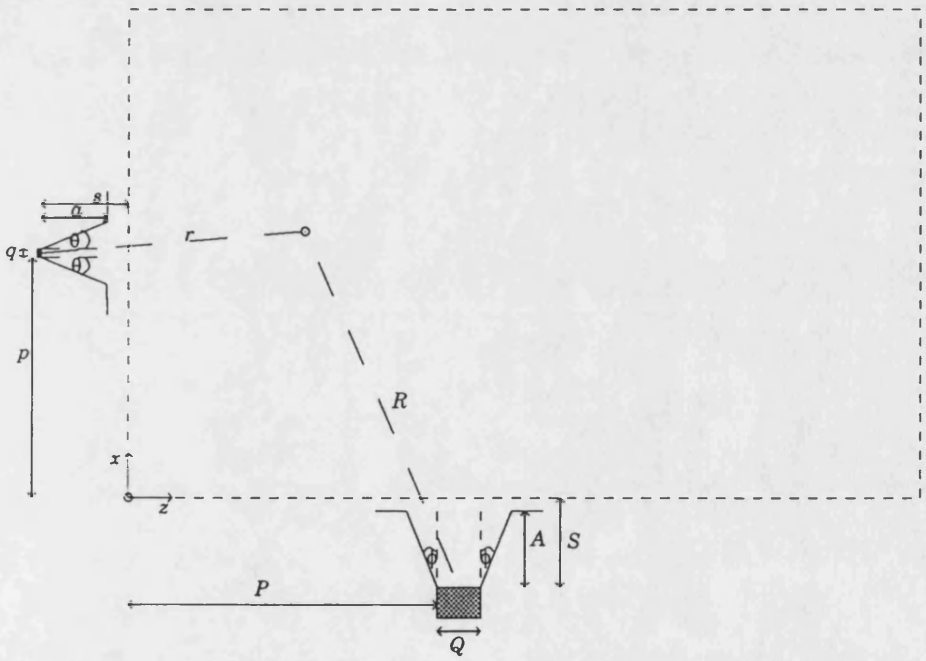

Figure 5.2.1 - Illustration of parameters used in model of sensitivity variation in air

thus allowing for the penumbra effect of collimation.

The factors discussed above were used to calculate a sensitivity for pixels in the field of view of the the detector and a source, using equation 5.2.2, where, s, is sensitivity at a point with parameters as illustrated by figure 5.2.1, and κ is the product of the proportion of the detector and the proportion of the source that can be seen by the point. The results of this model are illustrated in figure 5.2.2.

$$s = \frac{\kappa}{r^2 R^2} \tag{5.2.2}$$

The value of κ is therefore between zero and unity, only being unity when the whole of the detector and the source can be seen by the point. For this to occur the conditions given in both 5.2.3 *and* 5.2.4 must be fulfilled.

$$p - (s + x)\tan\theta < y < p + q + (s + x)\tan\theta \tag{5.2.3}$$

$$P - (S + Y)\tan\phi < x < P + Q + (S + Y)\tan\phi \tag{5.2.4}$$

However κ will be zero if the point can not be seen by either the source or the detector, this will be true if the conditions in either 5.2.5 *or* 5.2.6 are fulfilled, assuming the collimators are made of perfectly absorbing material. (The effect of collimators which are not perfectly absorbing has already been shown to be small by ourselves (chapter 2) and by Laird *et al* (1982)).

$$p - \frac{s + x}{a}(a\tan\theta + q) < y < p + q + \frac{s + x}{a}(a\tan\theta + q) \tag{5.2.5}$$

$$P - \frac{S + Y}{A}(A\tan\phi + Q) < x < P + Q + \frac{S + Y}{A}(A\tan\phi + Q) \tag{5.2.6}$$

5.2.2 Experimental results

The experimental arrangement was identical to that modelled and described above. The gold-plated ball was moved around a 10mm grid and a spectrum recorded at a number of positions for 30 minutes. Table 5.2.1 gives the recorded number of counts in the $K_{\alpha 1}$ peak in each position. The value calculated for each point by the model is also given in italics in table 5.2.1. Figure 5.2.2 gives

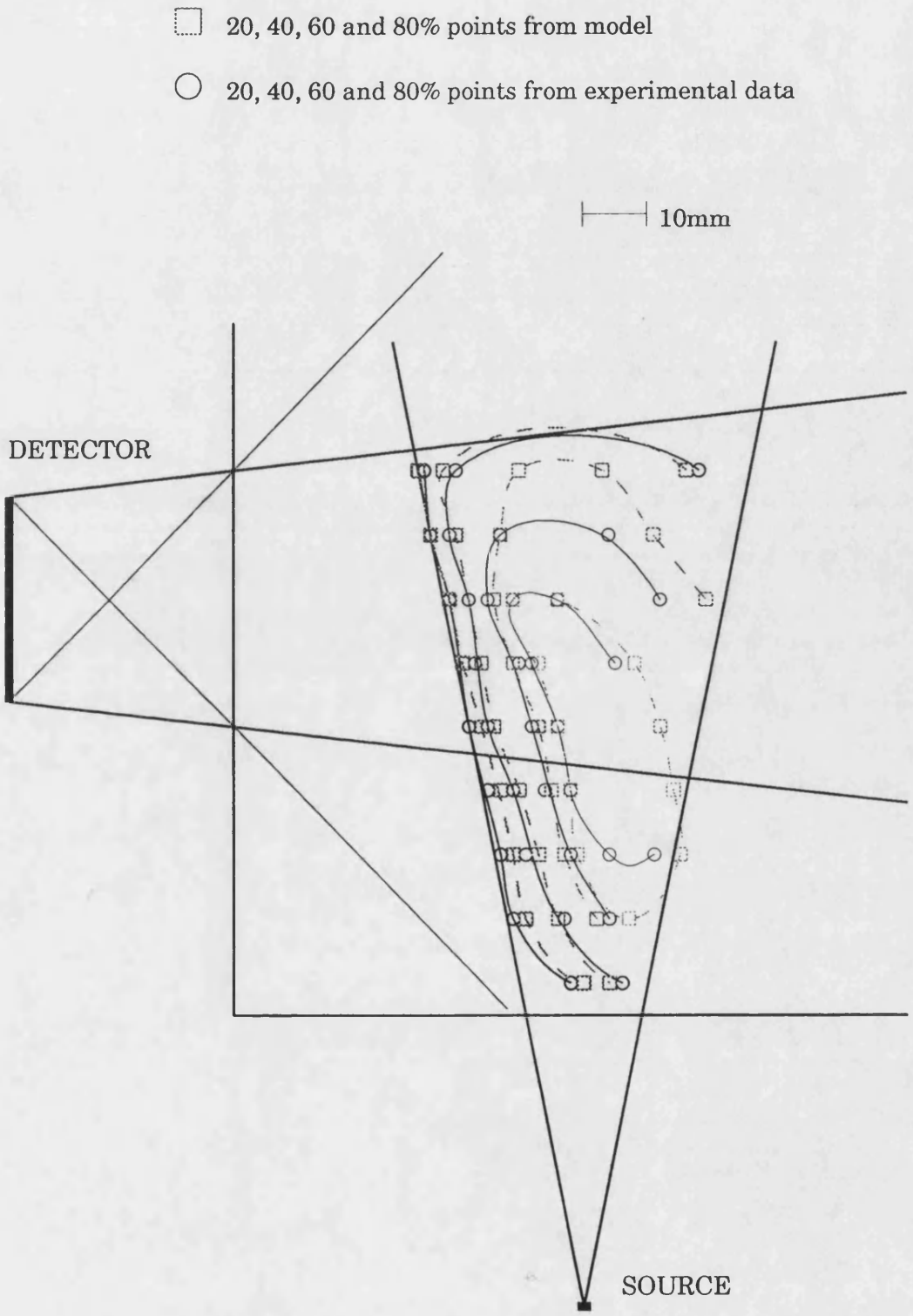

Figure 5.2.2 - Diagrammatic representation of both experimental and model results for sensitivity variation in air

z/mm	x/mm 5	15	25	35	45	55	65	75
5	0	0	0	0	0	0	1021±85	1185±84
	0	*0*	*0*	*0*	*0*	*231*	*1975*	*2029*
15	0	0	0	0	0	1004±83	1375±90	1378±89
	0	*0*	*0*	*0*	*0*	*1485*	*1928*	*1868*
25	0	0	0	0	0	1639±90	1739±93	1827±93
	0	*0*	*0*	*0*	*0*	*1926*	*1887*	*1751*
35	0	0	0	0	124±73	1974±95	2181±95	1984±95
	0	*0*	*0*	*0*	*0*	*1995*	*1851*	*1659*
45	0	0	0	0	668±86	2080±100	2120±97	2016±94
	0	*0*	*0*	*0*	*612*	*2039*	*1812*	*1580*
55	0	0	0	0	1650±90	2186	1815±93	1554±93
	0	*0*	*0*	*0*	*1579*	*2056*	*1766*	*1504*
65	0	0	0	0	2003±93	1823±95	1643±91	1441±92
	0	*0*	*0*	*0*	*2268*	*1909*	*1589*	*1324*
75	0	0	0	149±75	2130±95	1724±93	1410±90	1342±88
	0	*0*	*0*	*2*	*2040*	*1666*	*1374*	*1140*
85	0	0	0	746±81	1814±92	1342±90	1207±90	982±89
	0	*0*	*0*	*722*	*1776*	*1440*	*1183*	*979*
95	0	0	122±72	853±83	1624±90	1312±89	1106±87	885±85
	0	*0*	*0*	*1143*	*1516*	*1229*	*1010*	*838*

Table 5.2.1 - Experimental and model results for sensitivity variation in air (*Model results in italics*)

a diagrammatic representation of both the model and experimental results, using a contour plot of number of counts at a given point. Normalisation of the model was achieved by weighting the model such that the total number of counts, at the points where experimental data was available, was the same as the total number of counts in the experimental data.

5.2.3 Conclusions from work in air

A comparison of the modelled response with the experimentally determined response reveals a good correlation. Thus it is concluded that the fall off in photon intensity is well understood, and can be explained by use of the appropriate form of the inverse square law. The apparent slight deviations observed between the experimental data and the computer model in figure 5.2.2 can be explained by the fact that the experimental data contains a degree of error, due both to counting statistics and uncertainty in the position of the

gold-plated ball and collimators.

5.3 Sensitivity variation in water

The introduction of a scattering medium such as water complicates the modelling problem considerably. As already mentioned the exciting photons will be attenuated by the scattering medium, as will the fluorescence photons. It would be easy to allow for this using an appropriate absorption coefficient in equation 5.2.1. The appropriate form of equation 5.2.2 would then become that given in equation 5.3.1.

$$s = \frac{\kappa e^{(-\mu_1 R - \mu_2 r)}}{r^2 R^2} \qquad (5.3.1)$$

However this is an over-simplification of the problem, since exciting photons that are scattered by the water, may still have enough energy to excite fluorescence in the gold. Indeed these scattered photons which still have enough energy to excite fluorescence will have an energy closer to the K absorption edge and therefore an increased cross-section for absorption. It can be deduced from the Klein-Nishina formula that a good proportion of photons are scattered in the forward direction (section 2.2; $\alpha \approx 0.2$). Therefore to model this situation with accuracy would require a Monte Carlo, photon tracking, type of calculation.

5.3.1 Monte Carlo Model

Since the only method of accurately modelling the sensitivity variation in water would be a Monte Carlo type model, such a model was written. The detailed code is given in Appendix B, however an outline of the model, followed by some of the specific details are given below.

In order to calculate the relative sensitivity to gold at each point in the scattering medium, the model tracked the 'life history' of a large number of photons. In outline the program generates a photon from the source and follows

it until it 'dies' (see below). The photon initially has a random trajectory within the constraints imposed by the source collimator. The energy of the photon is randomly determined: In the case of the filtered ^{153}Gd source used in previous experiments, there is a probability of 0.60 of the photon energy being 97keV and 0.40 of being 103keV. From the photon energy an appropriately weighted random path length can then be determined (further details are given below). At the end of this path the photon undergoes some interaction, in the case of photons of initial energy around one hundred keV, there are three possibilities: Compton scattering, elastic scattering or a photoelectric interaction. The probability, p_i, of an interaction type i is given by equation 5.3.2, where μ_i is the component of the absorption coefficient due to interaction type i and μ_{tot} is the total absorption coefficient given by equation 5.3.3.

$$p_i(E) = \frac{\mu_i(E)}{\mu_{tot}(E)} \tag{5.3.2}$$

$$\mu_{tot}(E) = \sum_i \mu_i(E) \tag{5.3.3}$$

Once the type of interaction has been determined the effect on the photon can be calculated. For a scattering interaction a new trajectory for the photon can be found in a random fashion, and hence for a Compton scattering the new energy of the photon. The process described above is then repeated. For a photoelectric transition it is assumed that the energy of the photon is completely absorbed at the interaction site. If the interaction is with a gold atom then there will be a resulting fluorescence signal which is of interest. The proportion of this fluorescence signal entering the detector is then calculated using equation 5.3.4, where r is the distance between the interaction point and the point where the photon leaves the scattering medium in the direction of the centre of the detector; μ_{photo} and $\mu_{photo,Au}$ are the the components of the absorption coefficient due to the photoelectric effect, and the photoelectric effect due to gold alone respectively; and Ω is the solid angle subtended by the

detector at the interaction point.

$$s = \frac{\mu_{photo,Au}}{\mu_{photo}} e^{-\mu r} \frac{\Omega}{4\pi} \qquad (5.3.4)$$

Obviously a photoelectric transition leads to the 'death' of a photon, as far as tracking its life history is concerned. However there are also other ways in which the photon can 'die'. Firstly it can leave the scattering medium: The situation represented by the program given in appendix B is that the scattering medium is a semi-infinite cuboid with bounding planes z = SSD, and x = -X_SKIN, where SSD is the source to skin distance and X_SKIN is the distance between the source and the skin in the direction of the detector. The source is at the position $x = y = z = 0$, and the centres of both the detector and the source lie in the $y = 0$ plane. This is illustrated in figure 5.3.1. If the photon left the scattering medium and entered the detector the energy of the photon was recorded. This was used to build up a profile of the background spectrum that would be recorded by the detection system, and could be easily compared with

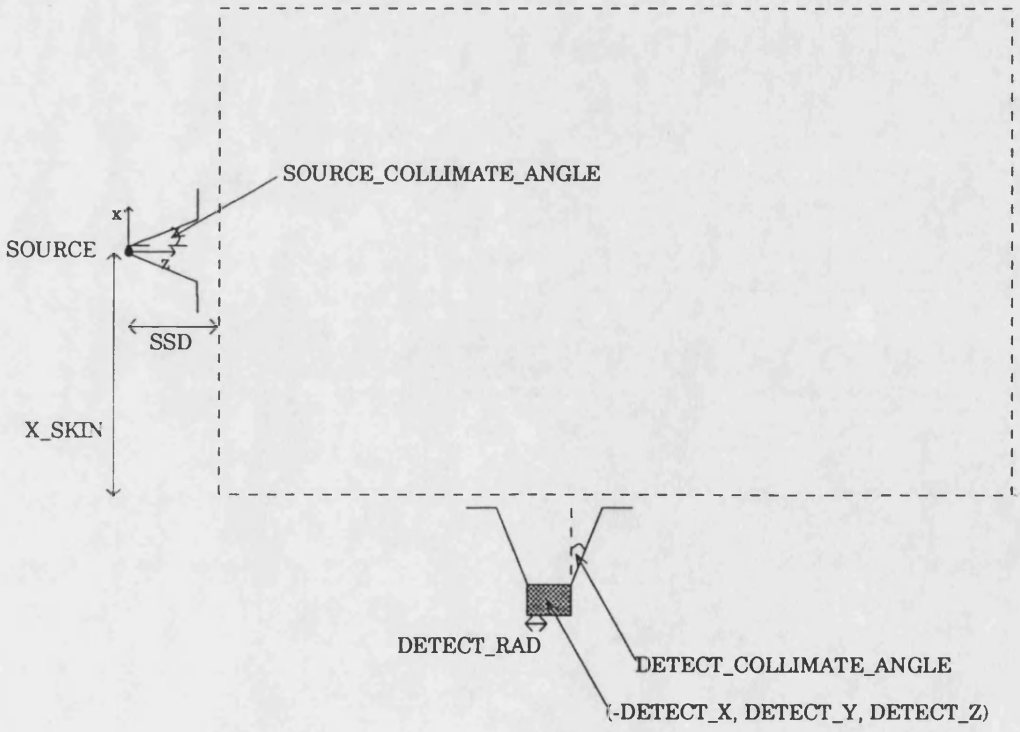

Figure 5.3.1 - Illustration of Monte Carlo model parameters

experimental results. Secondly the photon can also 'die' by losing so much energy by Compton interactions it is no longer of any interest. This occurs when the photon can no longer excite a photoelectric transition in gold. The program was therefore written such that it would stop tracking a photon once its energy was less than the K absorption edge of gold (~80keV).

The details of how the program modelled a number of situations are described in the following paragraphs, beginning with path length. In order to determine an average path length in a scattering medium, it is necessary to know the number of photons, n, in a beam at a distance, r, through the medium. This is given for a medium with attenuation coefficient, μ, by equation 5.3.5, where n_0 is the initial number of photons in the beam.

$$n = n_0 e^{-\mu r} \tag{5.3.5}$$

Therefore the probability, $p(r)$ that the first interaction occurs between r and r+dr in such a medium is given by equation 5.3.6 and equation 5.3.7 gives the corresponding distribution function, $P(r)$, for a first collision at distance less than or equal to r.

$$p(r)dr = [e^{-\mu r}]\,\mu dr \tag{5.3.6}$$

$$P(r) = \int_0^r p(r)\,dr = 1 - e^{-\mu r} \tag{5.3.7}$$

It follows that the Monte Carlo determination of path length, r, from an arbitrary point of departure to first collision, assuming the medium is homogeneous and infinite, is found by setting the distribution, $P(r)$, equal to a random number, ζ, with a value between zero and unity. This can be rearranged so that the path length, r, is given by equation 5.3.8.

$$r = \frac{-\ln(1 - \zeta)}{\mu} \tag{5.3.8}$$

Since $(1 - \zeta)$ is equidistributed on $0 \leq \zeta < 1$ if ζ is, equation 5.3.9 may be used in

the program to determine the path length, r, in the scattering medium.

$$r = \frac{-\ln \zeta}{\mu} \tag{5.3.9}$$

It is clear that for many of the situations modelled by the program, a value of an attenuation or scattering coefficient is needed. These coefficients are a function of energy, and are therefore not constant within the history of a photon. Data was therefore taken over an appropriate energy range from Hubbell (1969 & 1982) and a log-log linear regression of coefficient against energy was then performed, (for gold separate regressions were performed above and below the K absorption edge). In all cases the modulus of the correlation coefficient exceeded 0.98, and therefore these models were used to calculate the appropriate coefficients by the program.

Once the path length has been determined, the effect of the interaction at the end of that path needs to be found. The photoelectric interaction has already been discussed which leaves two scattering interactions to consider. When a photon is Compton scattered, the scattering angle can be between 0 and 180°. However each angle does not have an equal probability, and, as already discussed in chapter 2, the scattering distribution is approximately given by the Klein-Nishina equation which is given by equation 5.3.10 for unpolarized photons, where r_0 is the classical radius of an electron; E_0 and E are the energies of the photon before and after scattering respectively and θ is the scattering angle.

$$d\sigma_{compton} = \frac{r_0^2}{4}\left(\frac{E}{E_0}\right)^2\left(\frac{E_0}{E} + \frac{E}{E_0} - 2 + 4\cos^2\theta\right) d\Omega \tag{5.3.10}$$

There also exists a unique relationship between the scattering angle, θ, and final energy of the photon, E, which is given by equation 5.3.11a, which can be re-arranged to give equation 5.3.11b.

$$E = \frac{E_0}{1 + \frac{E_0}{m_e c^2}(1 - \cos\theta)} \tag{5.3.11a}$$

$$\cos\theta = 1 + m_e c^2 \left(\frac{1}{E_0} - \frac{1}{E}\right) = 1 + \frac{1}{\alpha_0} - \frac{1}{\alpha} \tag{5.3.11b}$$

Since it is true in general that,

$$d\Omega = -2\pi\, d(\cos\theta) \tag{5.3.12}$$

The differential scattering cross-section can be written entirely in terms of energy and is given by equation 5.3.13 where α and α_0 are the final and incident energies of the photon as a proportion of the rest mass energy of an electron, and are given by equations 5.3.14 and 5.3.15 respectively.

$$d\sigma_{compton} = \frac{\pi^2 r_0^2}{2}\left[\frac{\alpha}{\alpha_0} + \left(\frac{2}{\alpha_0} + \frac{1}{\alpha_0^2}\right) + \left(\alpha_0 - \frac{2}{\alpha_0} - 2\right)\frac{1}{\alpha} + \frac{1}{\alpha^2}\right] d\alpha \tag{5.3.13}$$

$$\alpha = \frac{E}{m_e c^2} \tag{5.3.14}$$

$$\alpha_0 = \frac{E_0}{m_e c^2} \tag{5.3.15}$$

Von Neumann's device (Cashwell and Everett, 1959) can now be used to sample this distribution to give the energy of the scattered photon, with correctly weighted probabilities.

The treatment of elastic scattering is more difficult, and this has therefore been ignored by most authors of photon tracking Monte Carlo models. This is not a bad approximation since the probability of elastic scattering is relatively small compared to the probability of Compton scattering at energies around 80-100keV. The angular distribution for elastic scattering is given by equation 5.3.16, where F(x,Z) is the atomic form factor for the atom by which the photon is being scattered; x is given by equation 5.3.17; and Z is the atomic number of the scattering atom.

$$d\sigma_{el} = \frac{r_0^2}{2}(1 + \cos^2\theta)\,[F(x\,,\,Z)]^2\,d\Omega \tag{5.3.16}$$

$$x = \frac{E_0 \sin\theta}{hc} = \frac{\sin\theta}{\lambda} \tag{5.3.17}$$

The method adopted by ourselves was that proposed by Persliden (1983), and is now described. From equation 5.3.16 the probability, $p(\theta)$, of a photon being elastically scattered by an angle θ can be derived and is given in equation 5.3.18.

$$p(\theta)d\theta = \frac{d\sigma_{el}(E\,,\,\theta\,,\,Z)\,d\theta}{\sigma_{el}(E\,,\,Z)} \tag{5.3.18}$$

This probability is then rewritten in terms of x^2, where x is given by equation 5.3.17, and is given by equation 5.3.19

$$p(x^2)dx^2 = \frac{r_0^2\,\pi\,2\lambda^2}{\sigma_{el}(E\,,\,Z)}(1 + \cos^2\theta)\,[F(x\,,\,Z)]^2\,dx^2 \tag{5.3.19}$$

since it is true that

$$p(x^2)dx^2 = p(\theta)d\theta \tag{5.3.20}$$

The two functions

$$A(x^2\,,\,Z) = \int_0^{x^2} [F(x\,,\,Z)]^2\,dx^2 \tag{5.3.21}$$

and

$$A(x^2_{max}\,,\,Z) = \int_0^{x^2_{max}} [F(x\,,\,Z)]^2\,dx^2 \tag{5.3.22}$$

where

$$x_{max} = \frac{1}{\lambda} \quad (\text{at } \theta = \pi) \tag{5.3.23}$$

are now introduced. The expression for $p(x^2)dx^2$ given in equation 5.3.19 may now be rewritten as follows:

$$p(x^2)dx^2 = r_0^2 \pi 4\lambda^2 \frac{A(x^2_{max}, Z)}{\sigma_{el}(E, Z)} \times \frac{1 + \cos^2\theta}{2} \times \frac{[F(x, Z)]^2}{A(x^2_{max}, Z)} \qquad (5.3.24)$$

or as

$$p(x^2)dx^2 = C(E, Z) \times g(\theta) \times f(x^2, Z) \qquad (5.3.25)$$

Now, $f(x^2, Z)$ is a frequency function, $g(\theta)$ is bounded $0 \leq g(\theta) \leq 1$ and C(E, Z) can be considered as constant for a given material and photon energy. In order to determine the scattering angle, a value of x is determined randomly using the inverse of $f(x^2, Z)$, and then Von Neumann's device (Cashwell and Everett, 1959) is used with $g(\theta)$ to decide whether this angle was rejected or accepted. If the angle was rejected the whole procedure was repeated.

The first stage of this process, that is finding the value of x from the initial random number, ζ, is non-trivial and is described in the following paragraph, which may be omitted on a first reading. To determine a value of x (given by equation 5.3.17) from a random number, ζ, it is clear, that the equation that needs to be solved for x in terms of ζ is given by 5.3.26.

$$\zeta = \int_0^{x^2} f(x^2, Z)\, dx^2 = A(x^2, Z)/A(x^2_{max}, Z) \qquad (5.3.26)$$

The solution of this is obviously non-trivial. The method that was used by ourselves was the value of $A(x^2, Z)$ was found by numerical integration (using the trapezium method with tabulated values of F(x, Z)), both for gold and water using the alternative expression for $A(x^2, Z)$ given by 5.3.27. The inverse distribution was then approximated by a fifth-order polynomial expression using a Marquadt-type fit. These polynomials were then used in the Monte Carlo program code (Appendix B).

$$A(x^2, Z) = \int_0^t [F(\sqrt{t}, Z)]^2\, dt \qquad (5.3.27)$$

The method of operation of the Monte Carlo model has now been discussed in detail. Each section of the model was tested individually, for example the Compton scattering section was tested to check that distribution of scattered photons was that predicted by Klein-Nishina formula, to within a 1% level of significance using the χ^2 test. The model was then run tracking 1×10^6 photons, with parameters of X_SKIN=55mm, SSD=45mm and DETECT_X,Y,Z = 90, 0, 130mm respectively. The results of this test run are presented in the following sections.

5.3.2 Model Results

The output from the model was a series of numbers representing the predicted sensitivities over a 10mm grid within the scattering medium. A plane section through this grid was taken containing the centre of both the source and the detector. A contour plot was then made of sensitivity. The contours represent 80%, 60%, 40% and 20% of the maximum sensitivity predicted. These contours could then be compared with a similar plot for the experimental results described in the following section.

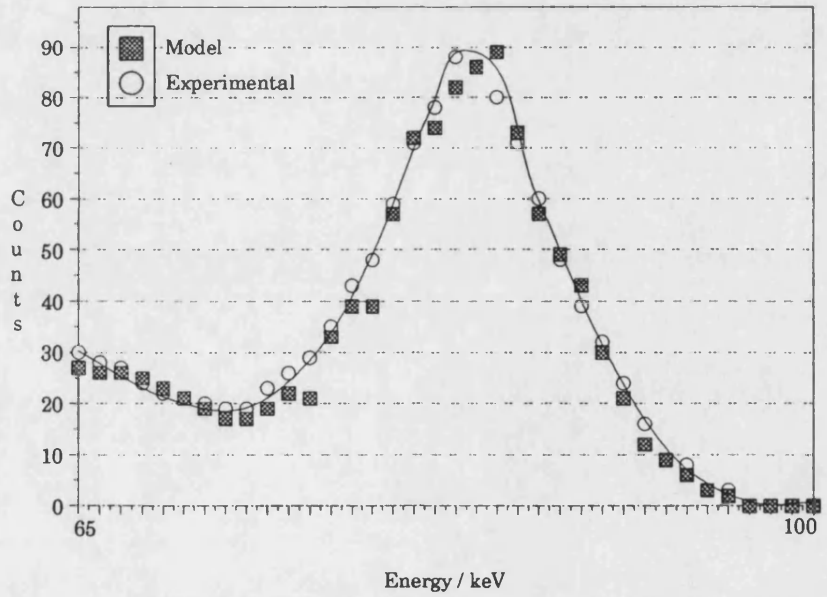

Figure 5.3.2 - Scatter spectrum predicted by Monte Carlo model, compared with experimentally determined spectrum. Note: The experimental data has been deconvolved with the detector response function as described and for the reasons detailed in Chapter 7

The other output of the model, as already mentioned, was a prediction of the shape of the Compton spectrum underlying the fluorescence peaks. A typical output is shown in figure 5.3.2 where this output is compared with an experimentally recorded spectrum. From this diagram it can be seen that the fit over the fairly limited energy region sampled is good, and therefore this a good indication that the model is working correctly. In fact the model was also run without any elastic scattering events, and the output was statistically insignificantly different from that with elastic scatter events. This demonstrates that the effect of elastic scatter is small, and is therefore justifiably omitted by most authors.

5.3.3 Experimental Results

As with all Monte Carlo models, it was important to test the model as thoroughly as possible, as erroneous results are easily obtained with this sort of model unless it is compared with experiment.

The experimental arrangement modelled, shown in figure 5.3.1, was set up so that the variation of sensitivity with position for one position of the source and detector could be evaluated, and is now described in more detail. Two small gold chain links were then moved over a 10mm grid in the plane containing both the centre of the source and the centre of the detector. Spectra were recorded over a period of 30 minutes for each grid position and the fluorescence peaks fitted using the program already described and given in Appendix A. The areas of the peaks were then used to draw a sensitivity contour plot in a similar way to that described in the preceding section. This contour plot was then compared with the one derived from the model results and this is shown in figure 5.3.3. The diagram also shows the primary beam of the source and the beam of acceptance of the detector. These beams being defined by the source and detector collimators. The significant penumbra on the detector beam of acceptance is also shown, as this was also allowed for within the model.

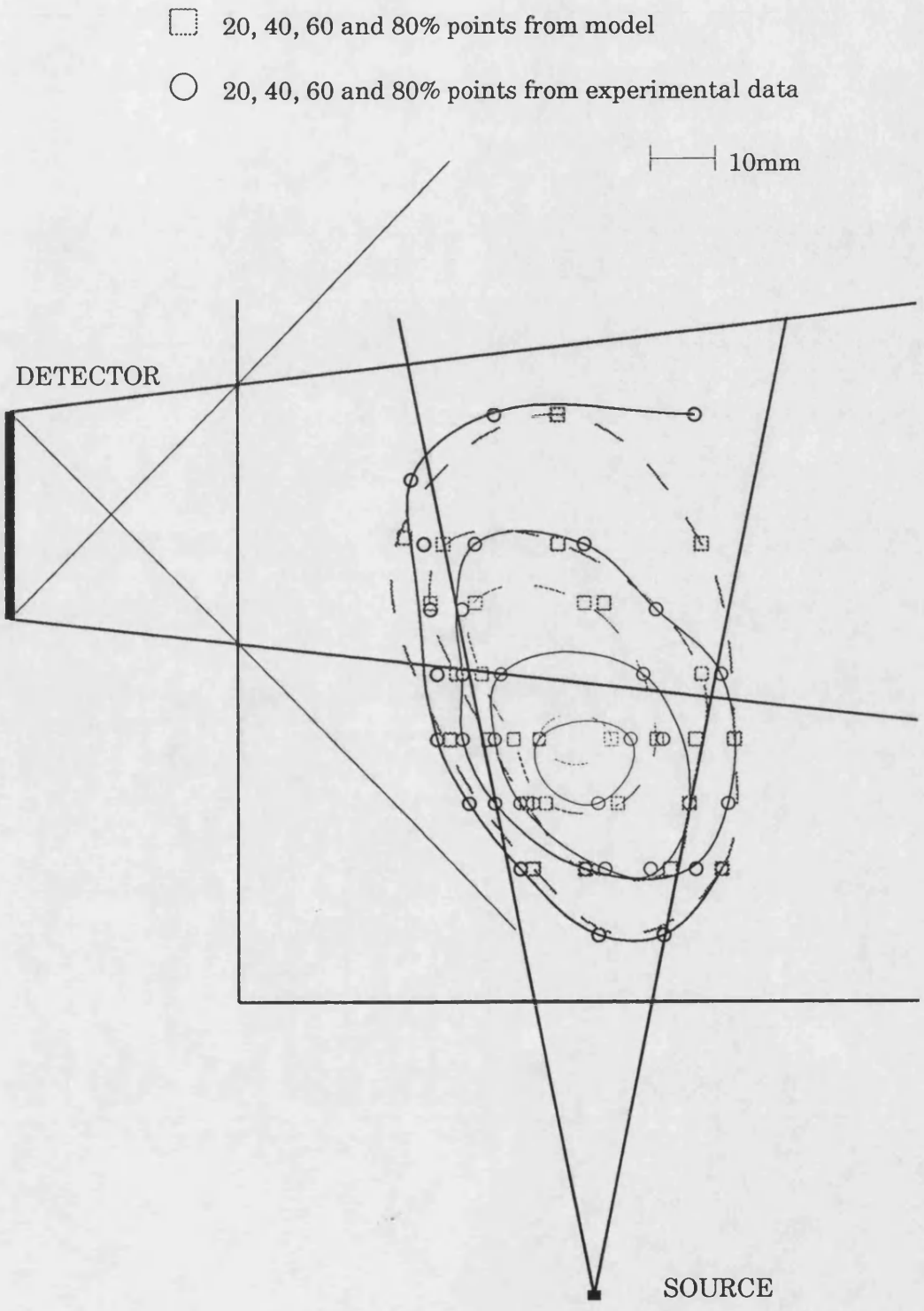

Figure 5.3.3 - Sensitivity variation in water predicted by the Monte Carlo model compared with that determined experimentally

z/mm	x/mm						
	-40	-30	-20	-10	0	10	20
70	0	777±346	314±336	0	364±339	1115±355	878±324
	0±0	*3±1*	*35±4*	*225±11*	*415±16*	*372±14*	*167±8*
80	0	1106±341	0	620±340	952±342	1463±334	1564±340
	14±5	*28±7*	*107±12*	*233±21*	*544±24*	*418±19*	*198±11*
90	300±346	802±340	4151±344	5230±348	3739±347	3822±348	2027±330
	57±18	*99±18*	*213±23*	*473±30*	*538±28*	*387±20*	*203±12*
100	2239±336	7501±346	5995±349	6291±351	4680±350	3601±335	2489±343
	131±37	*127±28*	*274±32*	*530±36*	*472±28*	*322±19*	*185±12*
110	4803±342	5506±344	6695±350	5403±350	3545±348	2651±349	2088±329
	206±50	*136±31*	*345±34*	*513±37*	*385±26*	*254±18*	*154±11*
120	4312±343	4975±346	3922±347	3648±349	3765±351	2278±333	1647±342
	83±42	*158±32*	*258±33*	*273±32*	*279±22*	*194±16*	*115±10*
130	546±351	2543±328	3714±348	2718±328	1959±344	1908±327	898±325
	34±28	*99±30*	*180±31*	*187±27*	*138±19*	*81±13*	*59±9*

Table 5.3.1 - Experimental and model results for sensitivity variation in water (*Monte Carlo model results in italics*)

5.3.4 Discussion and Conclusions

It is clear from figure 5.3.3 that the model fits the recorded experimental data fairly well, although not perfectly. The reasons for this discrepancy need to be considered carefully. It should be pointed out first that the experimental data is quite noisy which is difficult to show diagrammatically.

As already mentioned, one possible reason for the discrepancies between the contours predicted by the model and those derived from the experimental data is that both the model and experimental data contain uncertainties, which in some cases are a significant proportion of the determined value. This is easily seen upon examination of table 5.3.1 which shows the raw experimental data and the data output from running the model. The uncertainties associated with the experimental data are 1 standard deviation as returned by the fitting program. However there will also be some uncertainty associated with the positioning of the gold chain links (approximately ±2mm in all three dimensions). During the experimental procedure there would also have been some uncertainty in the alignment of the source/detector collimators, and also in the position of the scattering medium. The reason for this is that the tank in

which the water was contained had polythene sides which tended to bow when it was full. This meant that the tank sides were not perfectly vertical (as modelled) and therefore it was not possible to push them hard up against the collimators.

5.4 Monte Carlo Model in Use

The fact that both models discussed in the preceding sections predict the experimentally determined sensitivities with a good degree of accuracy shows that all the significant physical processes are well understood.

5.4.1 Sensitivity variation with different kidney position

Now that the Monte Carlo model has been shown to work, it is clear that it can be used to make some predictions. For example the model can be used to predict how the sensitivity to gold in the kidney would vary with position. This could be easily achieved by summing the sensitivities returned by Monte Carlo model over the volume of a kidney. This process could then be repeated with the source and detector collimators modelled in different positions such as might be used with different kidney positions in a clinical situation. And thus the relative sensitivities to gold with the kidney in various positions could be predicted. The results of using the model in this way for a number of different kidney positions are given in table 5.4.1. The volume summed over was a cuboid with a 60 x 60mm base in the x-z plane, which was 100mm high and centred on the intersection of the source and detector axes. These results show that there will be a strong fall off in sensitivity with depth, and therefore an accurate depth determination will be important.

Kidney Phantom Depth (Source/Detector) /mm	Monte Carlo Photoelectric Contribution per incident Photon
50/30	0.029
60/40	0.021
70/50	0.014

Table 5.4.1 - Relative sensitivities to gold in a 60x60x100mm volume for various phantom positions

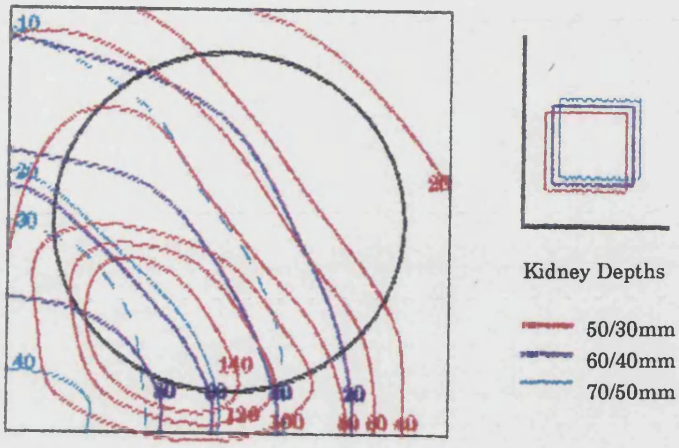

Figure 5.4.1 - Sensitivity contours predicted by Monte Carlo model for different kidney positions. The black circle shows the kidney volume

The model can also be used to predict how the sensitivity will vary over the kidney volume for different kidney positions. This type of prediction of how the sensitivity varies over the kidney volume is illustrated in figure 5.4.1. The figure shows how the sensitivity varies over a 60mm square centred on the kidney for three different kidney positions. These positions are 30mm, 40mm & 50mm between the kidney surface and skin surface in the direction of the detector and 50mm, 60mm & 70mm respectively between the kidney surface and the skin surface in the direction of the source. In this diagram the contours are normalised to the maximum sensitivity found for the 60/40mm kidney position. It is clear from these results that most of the gold fluorescence signal comes from the side of the kidney nearest the source. This is an important fact that will have to be borne in mind when interpreting any clinical results.

5.4.2 Effect of increased source to skin distance

Another use that can be made by the Monte Carlo model is to predict how the sensitivity will vary with an increased source to skin distance. An increased source to skin distance would need to be used if a more active source were used, since otherwise the detection system would saturate with the increased count rate. In order to evaluate the effect of increased source to skin distance the

SSD / m	X_SKIN / m	Z_MIN	DETECT_Z / m	SOURCE_ANG / °
0.045	0.055	4	(SSD+0.075)	12.0
0.125	0.055	12	(SSD+0.075)	6.4

Table 5.4.2 - Different parameter settings in the Monte Carlo model to assess the effect of increasing the source to skin distance

model was run twice with parameters set as shown in table 5.4.2. The difference between the two runs was an increase in source to skin distance from 45mm to 125mm. However in order that only the kidney volume was 'irradiated' the collimation angle of the source collimator also needed to be reduced from 12.0° to 6.4°. The sensitivity variation with position, within a 60mm square centred on the centre of the kidney volume is shown as a contour plot in figure 5.4.2. The contours shown are normalised to 100% on the maximum sensitivity (in counts) for the 45mm source to skin distance.

An examination of figure 5.4.2 leads to the conclusion that the difference in sensitivity variation across the kidney between these two different source to skin distances is small. From inverse square fall off alone it would be expected that the fall off in sensitivity across the kidney would be less rapid with an increased source to skin distance. However most of the photons reaching the

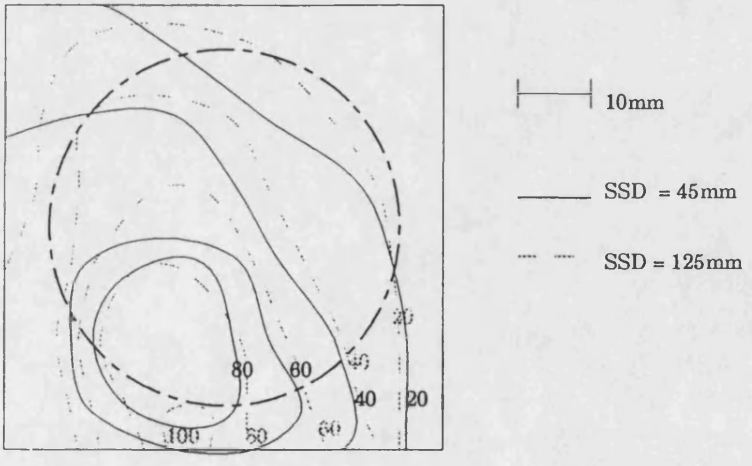

Figure 5.4.2 - The effect of increasing source to skin distance on the sensitivity contours within the kidney volume

kidney (around 70% for a depth of 50mm) will have undergone some interaction and therefore the observed effects will not necessarily be intuitive. As already mentioned, those photons undergoing a Compton scattering interaction have a large probability of being scattered in the forward direction when they have an energy of 100keV (section 2.2). Obviously sensitivities for the various kidney positions actually found in practice would need to calculated as described in section 5.4.1, however this does show that a relatively large error in determining source to skin distance would lead to a small error in determined gold concentration.

5.5 Conclusions

It is clear, from the work described above, that the Monte Carlo model works well and can be used in a predictive way to find the relative sensitivities at various kidney positions. This will obviously be very useful when it comes to undertaking clinical work. Using the model it will now be possible to tabulate the relative sensitivities for different kidney positions that might be found in practice. However if an atypical kidney position were found in a clinical situation it would be possible to run the model on a personal computer to find the relative sensitivity for that position.

Chapter 6

In situ radiation source

6.1 Introduction

In the work discussed in earlier chapters the radiation source used to excite the fluorescence was external to the body. There is however another possibility which is to use a source of radiation that is in the kidney. The method of getting this radiation source to the kidney is to use a radio-labelled drug, that when injected intravenously into the body, will end up in the kidney. This technique will have two advantages over the method using ^{153}Gd described in chapter 4. Firstly the source will be in the kidney and therefore will be unattenuated by overlying tissue. Secondly there will be greater uniformity of the radiation dose over the kidney volume, thus overcoming some of the large sensitivity variation discussed in chapter 5. A number of suitable drugs already exist and are used for studies in nuclear medicine departments. The two drugs that are in use regularly locally are diethylenetriamine penta-acetic acid (DTPA) and dimercapto succinic acid (DMSA). The former is used for dynamic (renogram) studies and the latter for imaging studies. DMSA is therefore designed to remain in the kidney for a longer period of time, and consequently gives a higher absorbed dose to the kidney than DTPA. The possibility of using either of these drugs as a radiation source in the kidney *in situ* in the kidney is discussed in this chapter. The questions that are addressed are whether sufficient activity of $^{99}Tc^{m}$ is found in the kidney for a sufficient period of time to give the required detection limit of 40μg gold (g tissue)$^{-1}$.

6.2 Activity of $^{99}Tc^{m}$ actually found in the kidney

In order to establish the activity of $^{99}Tc^{m}$ during a typical nuclear medicine study, the scans of patients stored on the computer at Royal United Hospital, Bath were re-examined. A phantom study was also undertaken, so that the count rate from a known activity of $^{99}Tc^{m}$ could be assessed for differing kidney depths.

Patient Number	Right Kidney 5mins*	40mins*	Left Kidney 5 mins*	40mins*
1	450	220	500	240
2	810	200	570	150
3	1070	250	990	250
Average	780	220	690	210

* Time after injection

Table 6.2.1 - Count rates (s^{-1}) from patients undergoing renogram (DTPA) studies

6.2.1 Re-examination of patient scans

The count rate variation over the region of interest of one kidney could be extracted from all renogram (DTPA) and some DMSA studies performed locally. It should be noted that in all these studies, the gamma camera was set to count over an energy window with a mean energy of 140keV ($^{99}Tc^{m}$ emission line) and (full) width of 28keV. This relatively large window width was required so that all the unattenuated 140keV photons would be detected due to the poor resolution of sodium iodide detectors.

In the case of renogram studies, there existed a well defined analysis protocol on the computer attached to the gamma cameras. Firstly the counts in several frames were summed so that the kidney could be easily identified. Secondly a region of interest was drawn around both left and right kidneys by hand using the joystick on the computer terminal. A background region of interest that was approximately kidney sized was also constructed. The computer then counted the number of counts in each of these regions on every frame. A graph of count rate against time was then presented. Figure 6.2.1 is a diagram taken from a typical display. Count rates at two different times after injection from a number of reportedly normal patients are given in table 6.2.1. The injected activity for all these studies was 185MBq.

A similar procedure was adopted for DMSA scans. However in this case, the count rate was calculated from a single frame. DMSA studies were imaging studies and therefore contained pictures taken from different positions around the abdomen of the patient. The posterior view was selected and a region of

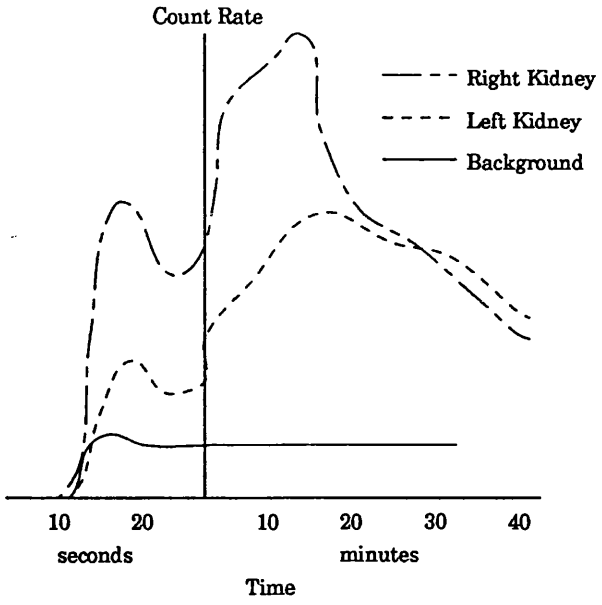

Figure 6.2.1 - Diagram taken from a typical display from the nuclear medicine computer showing count rate from the kidneys as a function of time

interest was drawn around both kidneys. The computer then summed the number of counts in each of these regions separately. The total number of counts in each region of interest was then divided by the time of exposure to give the count rate from each of the kidneys. Count rates deduced in this way from apparently normal patients are given in table 6.2.2. It should be noted that the pictures from which these count rates were derived were taken approximately three hours after the injection of the DMSA, and therefore the $^{99}Tc^{m}$ had decayed by half a half-life. The injected activity for all these results was 185MBq; this is the same as for the DTPA scans.

In order to relate the count rates reported above to activities in the kidney a phantom study was undertaken. In this study a kidney phantom was filled

Patient Number	Right Kidney	Left Kidney
10	1330	1480
11	1520	1510
12	1525	1580
Average	1460	1520

Table 6.2.2 - Count rates (s^{-1}) from patients undergoing imaging (DMSA) studies

Depth / mm	Count Rate / s^{-1}
30	2100
40	2000
50	1900
60	1700

Table 6.2.3 - Summary of results from gamma camera phantom study

with a solution containing 20MBq of $^{99}Tc^{m}$. This phantom was a 150ml, 47mm diameter polythene bottle, similar to those filled with chloroauric acid and used in the experiments described in previous chapters. The kidney phantom was then placed at various depths in a water bath. Pictures were taken with the gamma camera in a position similar to that used for renal studies. The count rate over the region of interest of the bottle was calculated in a similar manner to that described for the DMSA studies above. The results for various depths, representing the range of kidney depths that would be found in practice, are given in table 6.2.3 and a diagram of the experimental arrangement is shown in figure 6.2.2.

From these results it was concluded that the count rate recorded by the gamma camera is not very sensitive to kidney depth. This is important since kidney

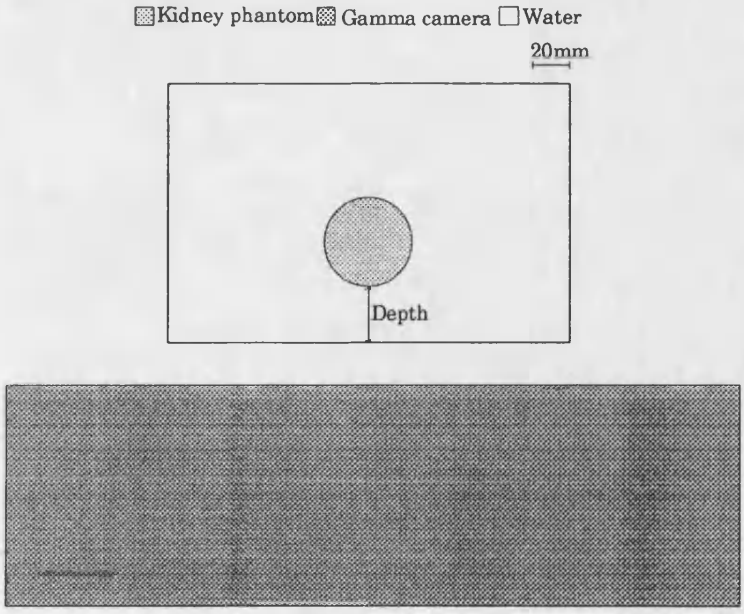

Figure 6.2.2 - Diagram showing experimental arrangement for phantom study with gamma camera

depth was not recorded in the patient records, and therefore an average kidney depth would have to be assumed in order to estimate the activity in the kidney. From the phantom data it was concluded that the uncertainty in this activity was not likely to exceed ±10% from the mean, as the count rate only fell from 2100cs^{-1} at a phantom depth of 30mm to a rate of 1750cs^{-1} at a depth of 60mm. This represents a fall in count of only 17%. An average count rate of 1925cs^{-1} from the phantom was assumed, this corresponds to 96cs^{-1} MBq^{-1}.

Averaging the data in table 6.2.1 over reportedly healthy kidneys of patients undergoing renogram studies gives a count rate of 740±240cs^{-1} 5 minutes after injection falling to a rate of 220±35cs^{-1} 40 minutes after injection. Thus the activities that are to be found in the kidney, allowing for both the range of recorded count rates and uncertainty in kidney depth, are 7.7±2.6MBq 5 minutes after injection and 2.3±0.8MBq 40 minutes after injection. Most of the uncertainty in these estimated activities is due to the physiological variation from patient to patient rather than the uncertainty due to an average kidney depth being assumed.

Averaging the data in table 6.2.2 over apparently healthy kidneys of patients undergoing DMSA scans gives a count rate of 1490±80cs^{-1} approximately three hours after injection. The biological half-life of DMSA is much longer than the physical half-life (Maisey, 1980) and therefore the count rate variation with time is small. Using the phantom calibration described above, this count rate, of 1490±80cs^{-1} corresponds to an activity of $^{99}Tc^{m}$ in the kidney of 15.5±1.8MBq, again allowing both for the spread in count rates recorded and uncertainty in kidney depth. In this case the uncertainty due to the assumed average kidney depth is more significant due to the small variation in count rate over the three patients in table 6.2.2. This is probably due to the physiological variation in the uptake of DMSA being less than for DTPA, which is consistent with the different uses of the two drugs: DTPA is used when a severe renal failure is suspected, and DMSA is used when the suspected pathology is impaired renal

function from small isolated parts of the kidney. It is therefore expected that with DMSA studies the variation in uptake of the drug would be smaller than with DTPA.

The conclusion from the above study is that for the same injected activity (in this case 185MBq) a higher activity is found in the kidney with DMSA than with DTPA over the time period available for the patient measurement. Additionally for the same injected activity the estimated effective dose is approximately the same for both pharmaceuticals.

When examining the pictures of both phantom and patient studies, there was a region of lower intensity surrounding the kidneys/phantom. In a patient this could be due to uptake of the radio-pharmaceutical in the surrounding tissue, low angle Compton scatter in the tissue of the 140keV photons, or penetration of the gamma camera collimator by photons. If this phenomenon was due to uptake of the radio-pharmaceutical by the surrounding tissue the magnitude of this effect would vary between the phantom and patient studies. A region of interest close to, but not overlapping, the kidney/phantom from a number of scans was analysed for count rate using a similar method to that described for DMSA scans above. This area was rectangular and was approximately one quarter of the area of the region of interest covering the kidney/phantom. The results are summarised in table 6.2.4. From these results it can be clearly seen that the intensity of the background in both cases is similar and is therefore due primarily to collimator penetration or low angle Compton scatter in the tissue. The gamma camera is an array of hexagonal holes in a 41mm thick sheet of lead with septal thickness of 0.3mm and hole diameter (side to side) of 2.5mm. A simple calculation based on equation 6.2.1 indicates that septal

Study	Kidney (N_K) / Cts Pixel^{-1}	Background(N_B) / Cts Pixel^{-1}	N_K/N_B / %
Patient	64	4	6
Phantom	332	21	6

Table 6.2.4 - Background count in patient and phantom studies

penetration is going to be a very small effect, contributing a background of much less than 1% of the image intensity. Therefore this background was attributed to low angle scatter.

$$I = I_0 e^{-\mu x} \qquad (6.2.1)$$

6.2.2 Phantom study using HPGe detector

A study was also undertaken using the hyperpure germanium detector to establish the activity of $^{99}Tc^m$ that would be required in the kidney to obtain the required detection levels. The experimental arrangement for this study is shown in figure 6.2.3. The detector collimator is the one that has already been described (section 3.4). Therefore it is clear that collimation was only optimum for a kidney depth of 30mm, however this was considered not to be important since the study was only to assess the feasibility of the technique, and detection levels would vary little due to under collimation as long as the whole kidney is seen by the detector (section 3.4). The kidney was represented as in previous experiments by 150ml, 47mm diameter, polythene bottle containing chloroauric acid with a concentration of gold of 500μg (g solution)$^{-1}$. The uptake of the radio-pharmaceutical was represented by a small (4.5ml) polythene tube, containing approximately 20MBq of $^{99}Tc^m$, placed down the centre of the bottle.

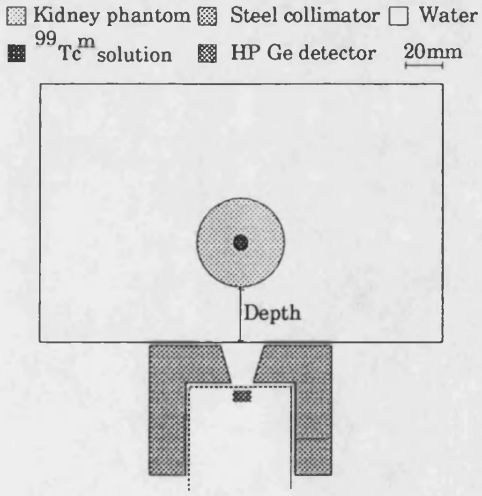

Figure 6.2.3 - Diagram of apparatus for phantom study with HPGe detector

This kidney phantom was placed in a water bath at a range of depths which may be found in practice. The wall of the water bath was positioned against the surface of the detector collimator. For an initial activity of 20MBq the resultant spectra were recorded over a period of 30 minutes, this represents the maximum acceptable time for patient studies. In practice the actual irradiation times were adjusted to compensate if the initial activity was different from 20MBq, using the following method. It is the total number of decays, P, that should remain constant between experiments. If the initial activity of the $^{99}Tc^{m}$ is A_0 and the decay constant is Λ, the total number of decays in a time period T is given by equation 6.2.2.

$$P = A_0 \int_0^T e^{-\Lambda t}\, dt = \frac{A_0(1 - e^{-\Lambda T})}{\Lambda} \qquad (6.2.2)$$

This equation can then be rearranged to give the time, T, required for a given number of decays, P. This is given by equation 6.2.3.

$$T = \frac{1}{\Lambda} \ln\left(\frac{A_0}{A_0 - \Lambda P}\right) \qquad (6.2.3)$$

The number of decays, P, from an initial activity of 20MBq of $^{99}Tc^{m}$ over a period of 30 minutes is easily calculated from equation 6.2.2, given that the decay constant, Λ, for $^{99}Tc^{m}$ is $0.115h^{-1}$. This value (of $P=9.71\times10^{6}$) can then be inserted into equation 6.2.3 to calculate the scan time required for other initial activities, A_0. This was the method used to calculate the scan time required for alternative kidney depths, so that all scans were equivalent to an initial activity of 20MBq scanned for 30 minutes.

A summary of the results from the scans at different depths is given in table 6.2.5. These results look very promising, with detection levels fairly close to the required $40\mu g\, g^{-1}$, for kidney depths of less than 30mm. These results do however require that 20MBq of $^{99}Tc^{m}$ is taken up in the kidney. This is clearly not the case for normal diagnostic injected activities (from the results in section

6.2.1).

6.3 Dosimetry

With this sort of experimental arrangement, the measurement of dose is considerably more difficult. It would be possible to measure the skin dose of a patient/phantom by attaching TLD chips to the skin surface. However since the radiation source is within the body, the skin absorbed dose will be small compared with the absorbed dose received by the kidneys. There are published figures for absorbed dose to different organs from standard injections used in nuclear medicine (ICRP, 1988). These values, for the kidney, for an injected activity of 185MBq of both DMSA and DTPA are given in table 6.3.1, together with the effective doses calculated using the weighting factors given in ICRP publication 60 (ICRP, 1990). With DTPA the absorbed dose to the kidney is much smaller than with DMSA. The reason for this is that with DTPA the bladder wall receives a considerable dose, contributing around 62% of the effective dose (ICRP, 1988).

The absorbed doses may also be calculated, if the activity in the kidney and other organs is known as a function of time (Snyder *et al*, 1975). Such a calculation is outlined below for DMSA which has the major uptake of $^{99}Tc^{m}$ into the kidney.

Scan Time / s	Activity / MBq	Phantom Depth /mm	$K_{\alpha 1}$ Peak / Counts	DL / $\mu g\ g^{-1}$
2280	15.9	20	3860±212	55
1800	20.0	30	3305±201	61
2028	17.8	40	2481±182	73
2979	12.3	60	1516±153	100

Table 6.2.5 - Summary of results from HPGe detector phantom study

Drug	Kidney Dose Dose /mGy	Effective Dose / mSv
DMSA	31	1.1
DTPA	0.9	0.8

Table 6.3.1 - Doses from 185MBq injected activity of DMSA and DTPA

In a calculation of this nature, the accumulated activity of the isotope under consideration in each organ in the body must be known. The absorbed dose to the target organ is then given by equation 6.3.1:

$$D = \sum_j S_j \tilde{A}_j \qquad (6.3.1)$$

where $\tilde{A}_j$ is the accumulated activity of the isotope in organ j, and S_j is the weighting from the organ j to the target organ. These 'S' values are given in MIRD pamphlet Nº11 for a number of commonly used isotopes. For the calculation of kidney dose from intravenously injected DMSA, the only 'S' value other than kidneys to kidneys that is significant is spleen to kidneys. However the amount of DMSA taken up in the spleen is small (ICRP,1988) and therefore the only significant contribution to absorbed dose in the kidney is from $^{99}Tc^m$ taken up in the kidneys themselves. It has already been found that 24% of the injected activity is taken up in the kidneys and stated that it stays there indefinitely. Therefore the effective decay constant, Λ, of $^{99}Tc^m$ in the kidneys is the physical decay constant of $^{99}Tc^m$, that is $0.115h^{-1}$. The accumulated activity is given by equation 6.3.2. (This expression can be derived from equation 6.2.2 by setting $T = \infty$, and Λ is the effective decay constant.)

$$\tilde{A} = \frac{A_0 T_{½}}{\ln 2} = \frac{A_0}{\Lambda} \qquad (6.3.2)$$

where A_0 is the initial activity in the kidney. The appropriate kidneys to kidneys 'S' value is 5.1×10^{-2}mGy MBq^{-1} h^{-1}. Therefore the absorbed dose for the kidneys for an injected activity of 185MBq is 19mGy.

6.4 Clinical system performance: predictions

As has already been mentioned, the results from the phantom study looked very promising, particularly at shallow kidney depths. These results did however rely on there being 20MBq of $^{99}Tc^m$ in the kidney, which clearly is not the case from the results in section 6.2.1, where a maximum activity of about 15MBq was detected. However if the detector size was increased to a diameter of 32mm, as is anticipated for a clinical system, these detection limits would be

Kidney Depth /mm	AAR /MBq	Absorbed Dose to Kidneys /mGy
20	4.2	5.3
30	5.1	6.2
40	7.3	14.7
60	13.9	17.5

Table 6.4.1 - Predicted performance of clinical system

reduced by approximately a factor of three (as discussed in section 3.5), thus bringing the sensitivity well within the useful range even for kidney depths of 60mm. It is clear from the results in section 6.2.1 that DMSA will be the optimum drug for this type of study, since for similar injected activities and effective doses a higher activity remains in the kidney for a longer period of time. Assuming that the detection limit will increase with decrease in square root of activity of $^{99}Tc^{m}$ in the kidney, and that the detection limit decreases with increase in detector diameter, for the same reasons as discussed in section 4.6, the anticipated activities that would be required (AAR) in each kidney to give a detection limit of 40μg g^{-1} are given in table 6.4.1. The absorbed dose to the kidney for the activity required in the kidney is also given (these were calculated using the MIRD 'S' value calculation outlined in section 6.3 and equation 6.4.1).

$$H = w_R D \qquad (6.4.1)$$

Chapter 7

X-rays as an excitation source

7.1 Introduction

In the previous chapter a proposal of using intravenously injected radio-labelled pharmaceuticals was discussed. The reason for this proposal was to give better uniformity of irradiation of the kidney than when using external radio-isotope sources. Another way of giving better uniformity of irradiation of the kidney might be to place the radiation further from the skin, thus reducing the effect of the inverse square law. However when using a radio-isotope source, there is a point where it impossible to obtain a source of sufficient activity to maintain the photon flux to keep the measurement time within acceptable limits. If an X-ray machine source could be used then, providing the tube rating is sufficient, much higher photon fluxes can be obtained. However an X-ray source is far from ideal in terms of its photon energy spectrum, as it contains large numbers of photons with insufficient energy to excite fluorescence in the gold. These low energy photons will give an absorbed radiation dose with no benefit. In fact the X-rays with energy just below the K absorption edge of gold will lead to an increased scatter background beneath the fluorescence peaks in the detected spectrum, with no benefit in terms of fluorescence yield.

An X-ray spectrum consists of two components, the bremsstrahlung and the lines characteristic of the target. If these characteristic lines are to be utilised, then they must have greater energy than the K absorption edge of gold (80keV). For the K_α radiation to have an energy greater than 80keV, a target with an atomic number, Z, greater than 86 (radon) is required. The only elements which fulfil this requirement and are stable are thorium (Z=90) and uranium (Z=92). There are no commercially available X-ray generators that have a target with such a high atomic number, and therefore the bremsstrahlung radiation must be utilised to cause fluorescence. It is, however,

possible to filter the beam of X-rays to increase the proportion of high energy X-rays. This is discussed further in section 7.2.

It has been demonstrated by Jonson *et al* (1988) that improved detection limits can be achieved by the use of partially polarized X-rays. The reasons for this are that if a 90° geometry is used the number of incoherently scattered photons entering the detector can be reduced by a suitable choice of axes, since plane-polarized X-rays will not scatter at 90° in the plane of polarization. However since the published results from this group in Göteburg indicate that polarization only leads to an improvement in detection limit by a factor of less than two, initial experiments were carried out using unpolarized X-ray source, using an old 100kV screening X-ray machine with a tungsten target. This machine had all filtration removed and had an unsmoothed half wave rectified power supply. The inherent filtration on the tube was 0.7mm aluminium.

7.2 Spectral measurements

As already mentioned in order to reduce any unnecessary absorbed dose to the patient due to low energy photons, it is necessary to filter the X-ray beam. It is obviously possible to calculate the effect of any filtration using tables of linear attenuation coefficient (for example Hubbell, 1982). However in order to do this it is necessary to know the spectrum of the unfiltered beam. A number of these spectra have been tabulated by Birch *et al* (1979). Therefore firstly an experiment was undertaken to check that the spectrum from our X-ray machine corresponded well to the appropriate one of these tabulated spectra.

In principle, the output spectrum of the X-ray machine could be measured by simply irradiating the hyperpure germanium detector with the X-ray generator, and comparing the recorded spectrum with the tabulated one. However in practice it was necessary to filter the X-ray beam emerging from the generator with an extra 1.7mm of aluminium so that it could be compared directly with the 2.5mm aluminium 100kV$_P$ tungsten target spectrum given by Birch *et al* (1979). It was also necessary to take precautions so that any X-rays

scattered from the head of the X-ray generator did not enter the detector and distort the recorded spectrum. The proportion of scatter entering the detector could be reduced by placing the X-ray generator at a large distance from the detector or by arranging collimation of source and detector so that only photons emerging from the tube entered the detector. Therefore three experiments were carried out. In the first the output from the X-ray generator was highly collimated as was the input to the detector. These were then aligned using a small HeNe laser. In the second experiment the X-ray generator was placed at a large distance from the detector (~3m) and in the third experiment both collimation and a large distance were employed. The results from these experiments are given in figure 7.2.1.

An examination of figure 7.2.1 leads to the conclusions that all three methods give similar spectral shape, and that there is considerable mismatch between the recorded and tabulated spectra at the low energy end. One possibility is that the low energy distortion is a side effect of incomplete charge collection in the detector. This phenomenon has been discussed already (section 2.4.1): For

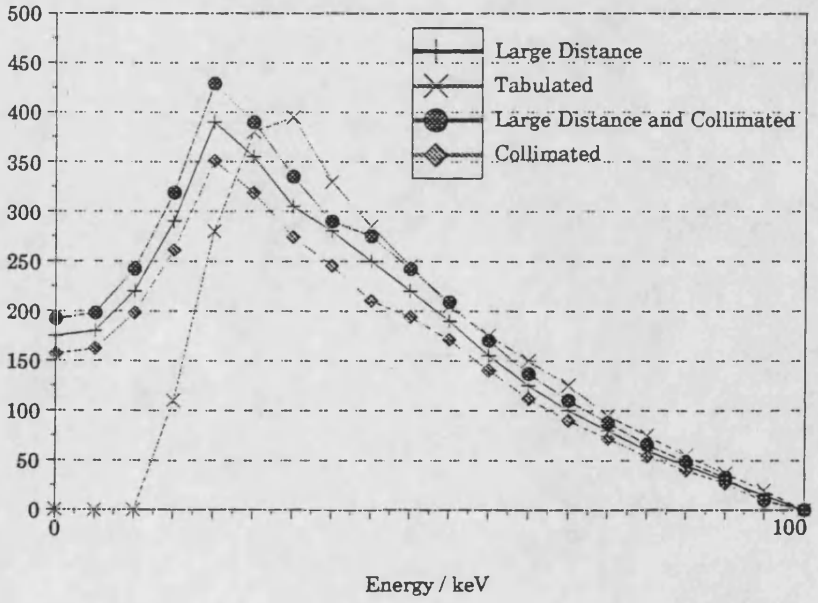

Figure 7.2.1 - Results of experiments to record X-ray spectra with reduced scatter effects

each photon energy that is detected, there will be a small number that will be assigned an energy below their real energy due to incomplete collection of the charge generated. A shelf is therefore seen on the low energy side of a monochromatic peak, of approximately 1% of the peak height. The accumulation of this effect over all the photons above 40keV, say, could well lead to the sort of distortion that is seen in these spectra. It is clear that at energies greater than 40-50keV a relatively good fit can be obtained.

In order to ascertain whether incomplete charge collection was responsible for the distortion of spectra at the low energy end of the spectrum, it would be necessary to deconvolve the recorded spectrum with the response function of the detector, which includes any incomplete charge collection effects. The recorded spectrum, $h(E)$, is the convolution of the real spectrum, $f(E)$, with detector response function, $g(E)$. and is therefore given by equation 7.2.1.

$$h(E) = f(E) * g(E) \tag{7.2.1}$$

Taking the Fourier transform of equation 7.2.1, equation 7.2.2, is obtained by the convolution theorem; where $H(t)$ is the Fourier transform of $h(E)$.

$$H(t) = F(t) \times G(t) \tag{7.2.2}$$

Therefore the real spectrum may be obtained by dividing the Fourier transform of the recorded spectrum by the Fourier transform of the detector response function and taking the inverse transform. Unfortunately the response function of this type of detector is not independent of energy. However the response function of the detector varies relatively slowly and smoothly with energy, it was therefore decided to attempt to deconvolve a real spectrum with the detector response function at an average energy. The energy chosen was that of the ^{241}Am photo-peak at 59keV since the response function of the detector could easily be measured at this energy, due to the very simple emission spectrum of ^{241}Am. The result of this deconvolution is shown in figure 7.2.2, together with the 'large distance' raw data, shown in figure 7.2.1, and the data tabulated by

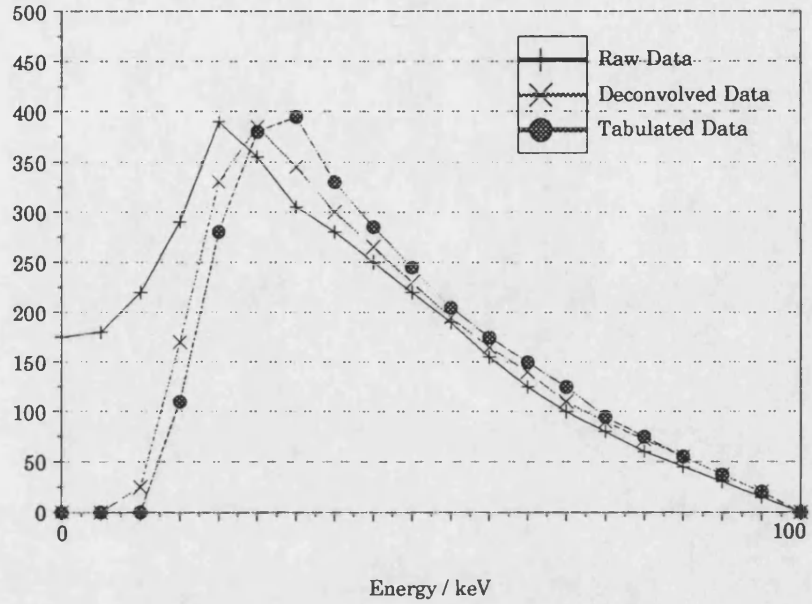

Figure 7.2.2 - Effect of deconvolution

Birch *et al* (1979). The deconvolution was performed using the a computer program based around the routine given by Press *et al* (1988). From this figure it can be clearly seen that this deconvolution process removes the low energy shelf from recorded spectra, and therefore it is incomplete charge collection that is the cause of the low energy shelf.

The next stage was to ascertain whether the effect that filters had on the output could be predicted by using the linear attenuation coefficients such as those tabulated by Hubbell (1982) together with the unattenuated spectrum. In order to do this the output of the X-ray generator was filtered with 6mm of iron and the pulse height spectrum was recorded and corrected using the deconvolution method described above. This spectrum was then compared with those predicted theoretically, using the data tabulated by Birch *et al* (1979) and Hubbell (1982) in equation 7.2.3. The result, shown in figure 7.2.3, clearly indicates that the effect of filtration can be predicted from available data on linear attenuation coefficients.

$$I = I_0 e^{-\mu x} \qquad (7.2.3)$$

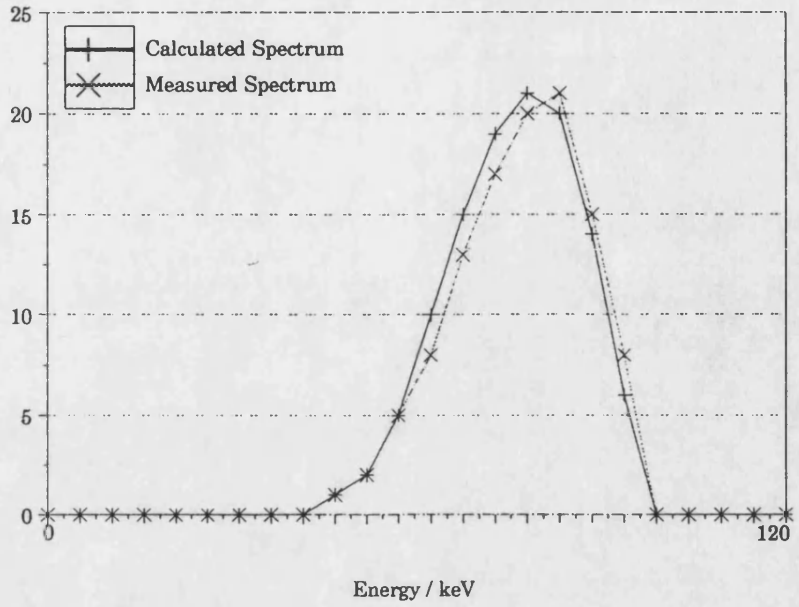

Figure 7.2.3 - Comparison of measured and calculated filtration effects

7.3 Unpolarized X-ray system

7.3.1 Incident spectrum

In the work described in the previous section a method of measuring spectra from X-ray sources was devised and demonstrated to be valid. It was also demonstrated that the effect of filtration with different filters of differing elements could be successfully calculated. For an X-ray fluorescence system with optimum fluorescence yield per unit absorbed dose it is obviously important to have a spectrum with a large proportion of photons with energy above the K absorption edge of gold incident on the patient. This leads to the conclusion that the beam should be heavily filtered. However if the beam is too heavily filtered then there will be insufficient photon flux to give the required detection levels due to the tube current limitations of the X-ray generator being used. The predicted result of filtering an unsmoothed 100kV spectrum from a tungsten target (characteristic lines omitted) with various filters is given in figure 7.3.1. From this figure it can be seen that the effect of filtering with 0.35mm of uranium (as used by Jonson *et al* (1988)) is similar to that of filtering with 5mm of iron. Since an appropriate thickness of uranium filter does not give a significantly improved spectral shape to iron, and iron is much

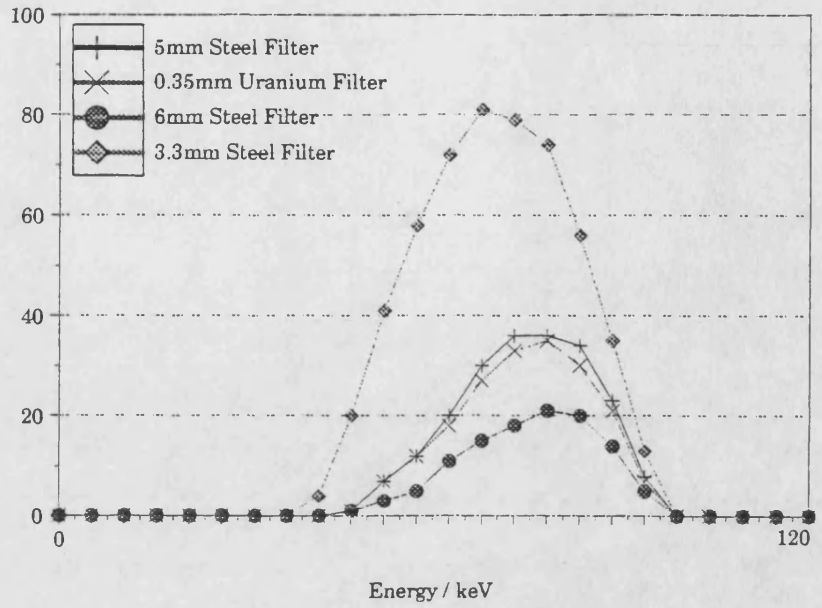

Figure 7.3.1 - Spectral output of X-ray generator with different filters

Filter	Proportion of photons able to excite fluorescence / %	
	100kV Spectrum	110kV Spectrum
8mm Steel	55	84
6mm Steel	41	71
5mm Steel	37	67
4mm Steel	30	56
3.3mm Steel	25	52
0.35mm U	39	68

Table 7.3.1 - Proportion of spectral output able to excite fluorescence in gold

easier to handle, the other spectra are for various thicknesses of iron filter. The proportion of radiation with energy above the K absorption edge of gold (81keV) (i.e. the useful radiation for X-ray fluorescence production) is tabulated in table 7.3.1. As expected the proportion above the K edge falls with decrease in thickness of filter for a given element.

7.3.2 Phantom study

In order to assess the detection levels that might be achieved with this type of filtered X-ray system a phantom study was undertaken. A diagram of the experimental arrangement is given in figure 7.3.2. The head of the X-ray generator was covered with 2mm lead sheeting to help prevent any leakage. Collimation, so that the kidney phantom was just irradiated, was achieved

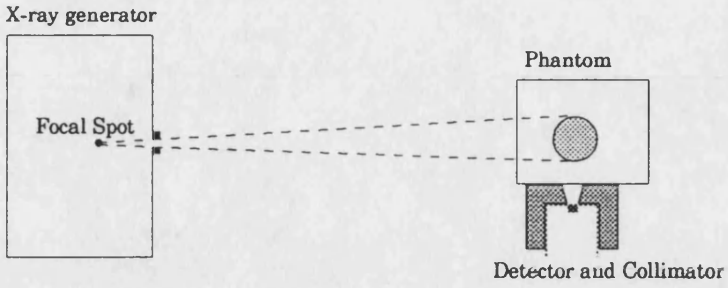

Figure 7.3.2 - Diagram of experimental apparatus for unpolarized X-ray system

using a small block of lead, 10mm thick, with a 10mm diameter hole drilled through it. In order that a good photon flux could be maintained with the limited tube current available on the X-ray equipment a 3.3mm steel filter was employed. An experiment was also undertaken using a 6mm steel filter to assess the improvement that could be achieved with a beam with a higher proportion of photons that could cause fluorescence. The filter was placed between the X-ray source and the collimator, so that scatter from the filter was largely eliminated. The detector collimator, kidney and body phantoms were those identical to those used to evaluate the ^{153}Gd system (chapter 4). Correct alignment of the phantoms was achieved using the image intensifier on the C-arm of the X-ray machine: thin strips of lead were temporarily placed down the side of the kidney phantom so that it could be distinguished from the water bath on the image intensifier display.

So that comparison could be made with the systems described in previous chapters, a similar kidney phantom position was adopted, that is 50mm lateral depth and 30mm posterior depth. Two tube potentials were used, the 100kV as already mentioned and one of approximately 110kV. This latter potential was achieved by adjusting the control on the X-ray generator that allowed adjustment for slight variation in mains supply voltage so that the maximum possible tube potential was achieved. A summary of the results collected from these phantom studies is given in table 7.3.2. These results clearly indicate that an X-ray source could be used as a source for X-ray fluorescence, but in

Tube Potential /kV	Filter Current / mA	Tube	Irradiation Time / min	$K_{\alpha 1}$ Peak / Counts	DL / $\mu g\ g^{-1}$
100	3.3mm Steel	45	60	936±198	281
110	3.3mm Steel	30	60	1454±203	184
110	6.0mm Steel	125	60	2179±210	127

Table 7.3.2 - Summary of results from X-ray system phantom experiments

order to compare these results with earlier systems some dosimetric information must first be obtained.

7.3.3 Dosimetry

In order to compare the results obtained above with other systems, such as the one based on ^{153}Gd it is obviously necessary to know the absorbed dose that is being received by the various organs. A dose determination was therefore carried out using TLD chips (section 4.4), for different degrees of filtration. The experimental arrangement consisted of a 180x140mm water bath, the surface of which was placed 300mm from the focal spot of the X-ray generator. Sachets containing three TLD chips were then stuck to the surface of this water bath. Calibration of the TLD chips in this case was carried out using the 250kV X-ray generator described in chapter 4 which had been calibrated from an NPL secondary standard dosimeter. The uncertainty in the resulting absorbed doses is expected to be less than 5%. A summary of the results is given in table 7.3.3. From these results it is possible to calculate the absorbed dose to the skin for other focal spot to skin surface distances using the inverse square law, and for alternative tube currents by linear scaling. However absorbed doses due to alternative filtration schemes and/or tube voltage need to measured directly.

Tube Potential /kV	Filter	Tube Current /mA	Irradiation Time / min	Skin Dose / mGy
100	3.3mm Steel	0.5	30	27
110	3.3mm Steel	0.5	30	42
110	6.0mm Steel	0.5	30	13

Table 7.3.3 - Summary of Dosimetry results for X-ray system

7.3.4 Beam Uniformity

To test the uniformity of the irradiation a piece of film was attached to the front face of the image intensifier. This was then exposed and developed. This was repeated for two different exposure times, with fixed tube current. When both films were scanned using a densitometer, the variation in optical density was less than 1% across the field. One had an optical density of 0.80 (8.4mA s) and the other an optical density of 2.85 (30mA s). From this it was concluded that there was very good uniformity of exposure over the irradiated area.

7.3.5 Conclusions from unpolarized X-ray system

From the work described above it is clear that it would be possible to use a heavily filtered X-ray source for XRF studies. If the fluorescence yield per unit dose is similar or greater than for the other systems described in chapters 4 and 6, then an X-ray system would be the system of choice, since the extra expense of replacing an isotope source at intervals would not be incurred. A summary of results allowing the X-ray systems described in this chapter to be compared with the isotope systems proposed in previous chapters is given in table 7.3.4. The results given in the table are a combination of those given in tables 7.3.2 and 7.3.3, and have been scaled in a similar way to those in previous chapters for a 32mm diameter detector and a source to skin distance of 500mm.

The results for the 100kV and 110kV tube potentials with 3.3mm steel filtration compare as expected. Since an examination of table 7.3.1 leads to the conclusion that the 110kV spectrum will contain approximately twice as many useful photons as the filtered 100kV. Therefore when using 100kV, it would be

Tube Potential / kV	Filter	Skin Dose for DL of 40μg g^{-1} / mGy	Tube Current 30min Irradiation Time / mA
100	3.3mm Steel	9.5	490
110	3.3mm Steel	4.2	125
110	6.0mm Steel	1.9	280

Table 7.3.4 - Prediction of clinical system performance

expected that just over twice the dose would be required to give a similar sensitivity (assuming dose is independent of photon energy over this relatively narrow energy range). This is indeed observed in table 7.3.4. Using a similar argument it would be expected that using 6mm rather than 3.3mm steel filtration would only reduce the required dose by a factor of 1.4, whereas a factor of 2.2 is observed. This can, at least in part, be explained by that with 6mm steel filtration the average photon energy is greater. Therefore a greater proportion of the photons are still able to excite fluorescence after having been scattered through a small angle. Since such large improvement in terms of sensitivity per unit dose can be achieved by increasing from 100kV to 110kV, it is obvious to consider whether a further improvement could be achieved using a 120kV X-ray generator. Using a similar argument based on the proportion of photons above the K absorption edge of gold in the incident spectrum, the conclusion is that there would be little anticipated improvement for 3.3mm steel filtration. As the proportion of useful photons would only increase from 52% to 61% and as the peak energy moves away from the absorption edge the cross-section for absorption falls off.

From the results in table 7.3.4 it can be concluded that an unpolarized X-ray source would be a suitable source for the determination of gold *in vivo*. There is a clear advantage of increasing the tube potential to 110kV and increasing in terms of reduction of skin dose. The latter is limited by the rating of the tube with regard to sustainable tube current. Although there would probably be some improvement in increasing the tube potential still further (our tube was designed for 100kV only) it is not anticipated that significant reductions in skin dose per unit sensitivity would be obtained.

7.4 Polarized X-ray source

As has already been mentioned, it has been reported that using a plane-polarized X-ray source reduces the background below the fluorescence peaks and therefore the detection limit is decreased. The background is decreased

since polarized photons will not scatter through 90° in the plane of polarization. It was therefore decided to attempt to verify this effect experimentally. In our experimental arrangement, the method employed to plane-polarize the photons was to scatter them off an aluminium target. The target was 25mm in diameter and cut off at the end at an angle of 45° to the axis. Unfortunately an X-ray source of 155kV$_P$, such as that used by the group in Göteburg, was not available to us. Therefore any polarized system that was evaluated was not actually going to be suitable for X-ray fluorescence studies of gold. However it would be possible to get an idea of the effect of polarization.

Therefore in the experimental arrangement, the scattering target was irradiated with a collimated beam of X-rays. The X-rays were collimated using a steel tube which had an internal diameter of 20mm and a wall thickness of 3mm. The two ends of the tube were placed against the X-ray generator and the sharpened end of the scattering target respectively. The distance between the X-ray generator head and scattering target was 300mm. The partially polarized X-rays were then used to irradiate a 150 × 200mm polythene container filled with water. The scattered radiation was then detected using our new 32mm diameter germanium detector. The detector and the polythene container were surrounded by 2mm lead sheet except for a small area through which the container was irradiated. Completely surrounding the apparatus was found to be necessary in order to reduce the background scatter from the surroundings to acceptable levels. The experimental arrangement is illustrated in figure 7.4.1.

The resultant spectra were recorded with the X-ray generator and the scattering target in two different orientations. One so that the amount of scatter from the water bath was a theoretical maximum and the other a minimum. Two spectra were also recorded without the aluminium scattering target present so that any part of the recorded spectrum that was due to 'background' effects other than partial polarization could be subtracted from

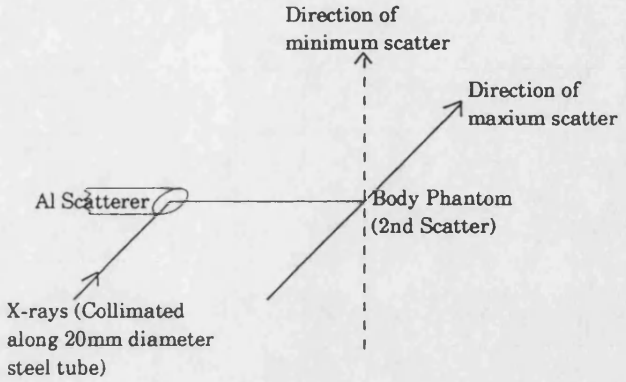

Figure 7.4.1 - Schematic diagram of experimental arrangement for polarized X-ray studies

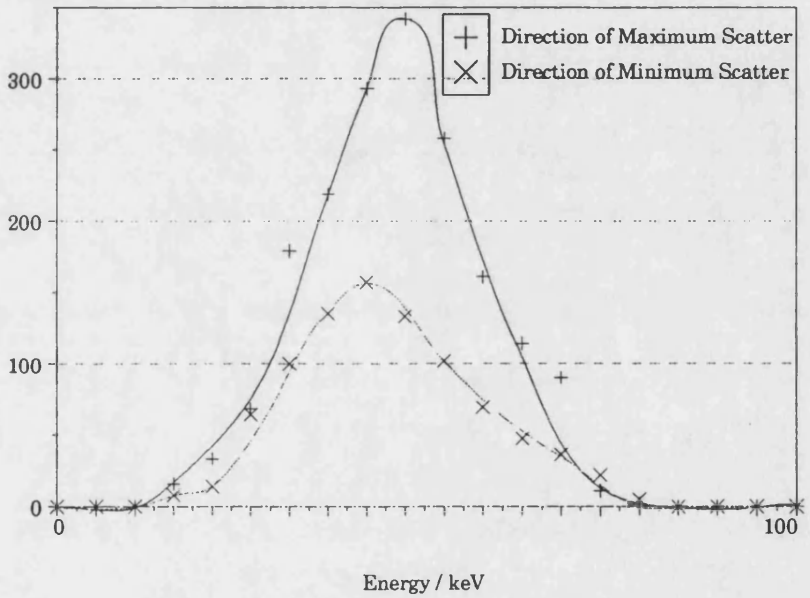

Figure 7.4.2 - Compton background in directions of minimum and maximum scatter

the recorded spectrum. All recorded spectra had a constant current-time product, and were recorded at sufficiently low count rates such that system dead-time was insignificant. The results from these experiments are shown in figure 7.4.2. From this figure it is clear that partial plane polarization does reduce the detection rate of Compton scattered photons. However the 'background' that had to be subtracted from the spectra shown in figure 7.4.2 was of similar magnitude to the spectra themselves. Because of this large 'background' and the fact that the experiments were carried out at lower energy than would be required in a clinical situation, it is impossible to

quantitatively predict the effect of polarization. However it is possible to confirm that it is a real effect. It is also clear from these experiments that if such a partially polarized X-rays were to be used in a clinical environment shielding of unwanted scattered 'background' radiation would be a problem, probably requiring a customised X-ray generating system surrounded by shielding, the rating of the tube would also have to be similar to those used in radiotherapy machines. Therefore setting up such a system would be a (prohibitively) costly procedure and may not give significantly improved detection limits, as compared to a radio-isotope system due to the 'background' scatter.

7.5 Conclusions

It is clear from the results using the unpolarized system that X-ray sources are a possible source of radiation for X-ray fluorescence studies of gold *in vivo*. It is also clear that a carefully constructed partially polarized system would give improved detection limits. However, X-ray systems are not without disadvantages. The main problems are that the large source to skin distances used lead to alignment problems and that a significant amount of scattered radiation from the intense primary beam can enter the detector if suitable precautions are not taken. In the phantom studies described above, thin strips of lead on the kidney phantom and the image intensifier on the C-arm of the X-ray generator were used to aid alignment. In an *in vivo* this would obviously not be possible, and an alternative alignment system would need to be sought. The scatter problems could easily be overcome with a purpose built system with shielding in suitable places, this would require a dedicated X-ray generator and would therefore not be a cheap alternative.

Chapter 8

Clinical System

8.1 Introduction

Now that all the various excitation possibilities have been evaluated (chapters 4, 6 and 7) and an understanding of the effect of other parameters has also been gained (chapter 3), it is possible to design a clinical system. The main design criteria are that the system should deliver the smallest possible radiation dose to the patient with the shortest possible irradiation time to achieve a detection limit of 40μg g^{-1}. The system must also not saturate any of the detection system components: the detector, pulse-shaping amplifier or the multi-channel analyser (MCA).

8.2 Optimum design parameters

8.2.1 New detector and Electronics considerations

In order that a larger number of counts could be collected per unit time/dose, a larger hyper-pure germanium detector was purchased. This detector was 32mm in diameter and 10mm thick with a resolution of 740eV (FWHM) at the ^{57}Co 122keV emission line. The new detector therefore had an area ten times greater than the old one, and thus would yield ten times the count rate for a given experimental arrangement. The new detector was designed to handle an energy throughput of 5000MeV s^{-1}, that is around 70 000cs^{-1} with an average photon energy of 70keV. This had throughput implications for the electronics following the detector preamplifier.

In the experiments described in previous chapters a shaping time of 6μs had been used on the pulse-shaping amplifier. If this practice were continued, the maximum frequency that could be handled by the pulse-shaping amplifier would be around 25 000cs^{-1} (or more realistically 6000cs^{-1} with a 25% dead-time), since the pulse length is approximately 6.6 times the shaping time. However at this counting frequency a significant amount of information would

be lost due to the irregular nature of the counting process involved. Therefore if significant losses of information were not to occur due to amplifier dead-time, a significantly shorter shaping time would be required. Thus a shaping time of 1μs was adopted for future work with the new detector, as recommended by EG&G Ortec (the suppliers of the detector). This gave a theoretical maximum count rate for the pulse shaping amplifier of around 160 000cs^{-1}, (40 000cs^{-1} with a 25% dead-time).

The final component in the detection equipment was the MCA. This had a fixed dead-time of 25μs per pulse. Therefore the theoretical maximum count rate was around 40 000cs^{-1} (10 000cs^{-1} with a 25% dead-time). This would seem to be the limiting factor, but the MCA had a low level discriminator (LLD) which could be varied between 0 and 50% of the full scale. Since in this type of X-ray fluorescence study, there is no reason for retaining the spectrum below the fluorescence peaks, much of the spectrum could be removed using the LLD. Thus the count rate that the MCA needed to handle could be greatly reduced by using the LLD such that only the portion of the spectrum above 60keV was collected by the MCA. This, for most excitation sources, effectively almost doubles the count rate that can be handled by the MCA to around 80 000cs^{-1} (20 000cs^{-1} with a 25% dead time).

All the stated limitations on count rate above, assume that the incoming photons are, on average equally spaced. This is obviously true for a radio-isotope source, however for an X-ray generator this is not always the case. If the X-ray generator does not have a constant potential power supply, photons of a given energy, E, can only be produced when the potential across the tube is greater than E/e, where e is the elementary charge. Therefore if the X-ray generator is unsmoothed such as the one used in the experiments described in chapter 7, the higher energy photons are produced in bursts. This is illustrated in figure 8.2.1 which shows the output of the pulse shaping amplifier recording a spectrum with the X-ray generator in an experimental arrangement similar

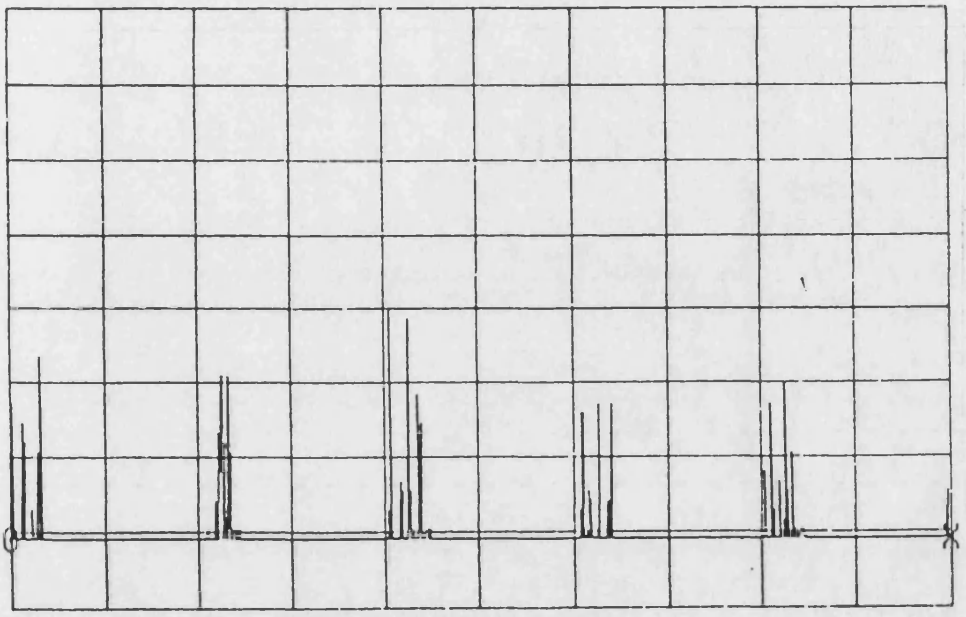

Figure 8.2.1 - Output of pulse shaping amplifier while recording an X-ray spectrum (The oscilloscope settings were 2V div^{-1} and 10ms div^{-1})

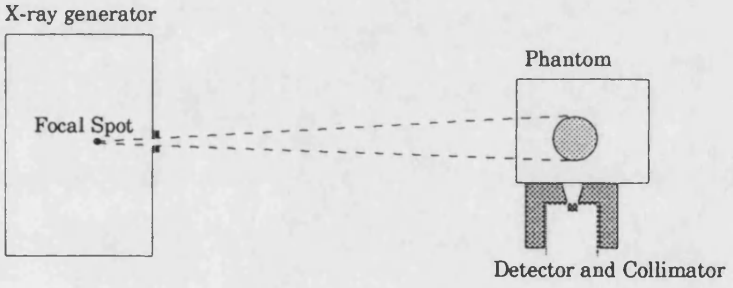

Figure 8.2.2 - Experimental arrangement for X-ray experiments

to that illustrated in figure 8.2.2 with 6mm steel filtration. From figure 8.2.1 it can be seen that the photons arrive at the detector in bursts, the frequency of these bursts being 50Hz. This is due to the fact that the X-ray generator used was only half-wave rectified and unsmoothed. Using this type of generator it would be the frequency of pulses within these bursts, rather than the frequency of the pulses averaged over 20ms, that would provide the count rate limitation. Therefore since the bursts of high energy pulses occupy less than one sixth of the total period of a 50Hz cycle, the total throughput of the system will be over

six times less than might otherwise have been expected.

8.2.2 Optimum excitation source

In previous chapters, when using the smaller 10mm diameter detector, three excitation sources have been considered. These were ^{153}Gd as the preferred external isotope source; $^{99}Tc^{m}$ radio-labelled pharmaceuticals; and X-ray sources. As previously stated the best excitation source will give the required sensitivity with the minimum radiation dose to the patient with the minimum exposure time. A summary of the best results predicted for the 32mm diameter detector from the results of previous chapters is given in table 8.2.1. In the first five columns, this table shows the resulting absorbed doses and activity/current required for a 30 minute counting time to achieve a detection limit of 40μg g^{-1}. The sixth column of the table gives the counting time that would be required to achieve a detection limit of 40μg g^{-1} with a count rate of 10 000cs^{-1} after the LLD on the MCA, which is the count rate that would give a dead-time of 25% with our MCA. The final column shows the corresponding required activity/tube current. Using the above criteria, it is clear that radio-labelled pharmaceuticals give larger doses of radiation to the kidney than external sources. Coupled with this the radio-pharmaceuticals give significant doses to other organs as well (ICRP, 1988), thus leading to an effective dose that is significantly greater than for the external sources. Therefore the optimum system is going to be based around an external source. Whether, for reasons

System	Peak Skin Dose /mGy	Kidney Dose /mGy	ED⁺ /μSv	Activity/Curr. /GBq or μA	Minimum Time$ / min	Activity/Curr. for $ /GBq or μA
DMSA	0.0	6.2	160	0.06	25	0.12
^{153}Gd#	3.1	0.4	11	2.2	12	8.1
X-ray1*	4.2	3.1	80	120	62	95
X-ray2°	1.9	1.3	30	280	30	420

⁺ ED - Effective Dose, due to skin and kidney doses only
Source to Skin Distance (SSD) = 45mm
* 3.3mm steel filtration, SSD = 450mm, Tube potential = 110kV
° 6mm steel filtration, SSD = 450mm, Tube potential = 110kV
$ Time required with count rate of 10 000 cs^{-1} at the MCA with LLD at 60keV

Table 8.2.1 - Predicted system performance with new 32mm diameter HPGe detector, all predictions for DL of 40μg g^{-1} in 30 minutes

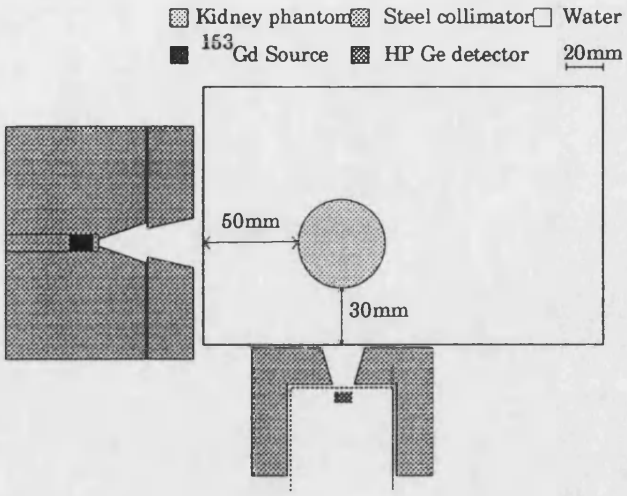

Figure 8.2.3 - Experimental arrangement for ^{153}Gd source

which will be discussed below, an X-ray source or a ^{153}Gd source is preferable as an excitation source is less clear.

Since the results in table 8.2.1 involve a considerable amount of extrapolation, it was decided to verify them experimentally with the new detector. The experimental arrangements used were those illustrated in figures 8.2.2 and 8.2.3, it should be noted that the 10mm diameter hyper-pure germanium detector has been replaced by one that is 32mm in diameter. Due to the increase in diameter of the detector a new detector collimator was required. This is illustrated in figure 8.2.4 and was designed such that the whole kidney phantom would just be seen at a depth of 30mm. The results from this experimental evaluation are given in table 8.2.2.

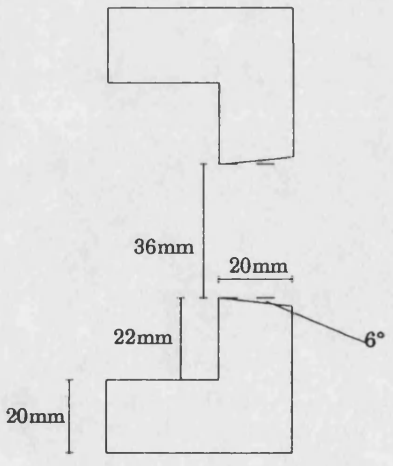

Figure 8.2.4 - New detector collimator

As table 8.2.2 shows the predicted detection limit of 40μg g^{-1} was not achieved with the 32mm diameter detector with either the filtered ^{153}Gd source or the X-ray sources. The main reason for this is that the larger detector was used with a shorter shaping time leading to a poorer resolution than the

System	Activity/Current /μA or GBq	Irradiation Time / min	DL /μg g^{-1}	Dead Time / %
$^{153}Gd^{\#}$	1.6	30	57	12
X-ray 1*	20	120	68	5
X-ray 2¤	65	80	64	6

#,*,¤ See caption for table 8.2.1
Table 8.2.2 - Experimental results with the 32mm diameter detector

smaller diameter detector with a longer shaping time: 550eV at the 60keV ^{241}Am emission line (compared with 380eV for the smaller detector). This leads to a predicted 20% increase in detection limit (from the square root of the ratio of resolutions). The system dead-times also were not allowed for in the extrapolations. The results for the filtered ^{153}Gd source were obtained with a slightly more active source (1.6GBq) than the source activity predicted (1.4GBq) to achieve 40μg g^{-1}. This leads to an expected 6% decrease in the detection limit over that predicted (from the square root of the ratio of activities). When the above factors are considered the measured performance of the 32mm diameter detector system agrees well with the performance predicted from the results obtained with the smaller detector.

It is clear from table 8.2.2, that of the three experimental systems examined, the ^{153}Gd system will give potentially the lowest detection limit, as it requires the lowest count rate to achieve 40μg g^{-1}. However, as already mentioned, the X-ray sources used were not ideal. It is possible to make some predictions, from the results of table 8.2.1, concerning the minimum detection limits that could be achieved with our current detection system and other X-ray sources. Table 8.2.3 gives the result of these predictions for all source types for a count rate of 10 000cs^{-1} at the MCA, corresponding to an MCA dead-time of 25%.

For the X-ray sources the result of using a constant potential generator is predicted, assuming a six-fold increase in the number of counts collected in 30 minutes, for the reasons already mentioned. A further improvement has been reported by Jonson *et al* (1988) using a partially polarized X-ray source. For their partially polarized X-ray system (155kV_P, 0.35mm uranium) with a

System	Detection Limit in 30 minutes at 10 000cs^{-1} /μg g^{-1}	ED /μSv
DMSA	36	270
Half-wave rectified X-ray/110kV/6mm steel	65	12
Const. Potential X-ray/110kV/6mm steel	26	75
Polarized X-ray/155kV/6mm steel*	15	75
Filtered ^{153}Gd	25	27

* Assuming a 1.75 fold decrease in DL, due to the partial polarization of the X-ray source
Table 8.2.3 - Predicted detection limits achievable with our current detection system

kidney depth of 40mm to the kidney centre, they reported a factor of 1.75 improvement in detection limit over a 100kV$_P$ unpolarized system. This improvement factor has been assumed for the comparison in table 8.2.3. Some of this improvement, however, may have been due to an increase in average energy of the incident photons as it has already been found by ourselves that an increase from 100kV$_P$ to 110kV$_P$ gives a dramatic improvement in detection limit using our half-wave rectified generator.

The predictions in table 8.2.3 would indicate that the highest sensitivity would be achieved using a partially polarized X-ray source. The filtered ^{153}Gd source produces a slightly poorer sensitivity for a similar effective dose. The advantage of an administered radio-pharmaceutical as an exciting source is its cheapness, but it does result in a higher effective dose for a poorer sensitivity than achievable with the other sources.

In conclusion it appears that a partially polarized X-ray system would give the best detection limits. However, for a partially polarized X-ray system, high tube potentials and currents must be used, which calls for a more heavily shielded room than for a ^{153}Gd source, also a suitable X-ray generator is required. Since we do not have access to a suitable X-ray generator or heavily shielded room, a system based around ^{153}Gd is best suited to our local circumstances and is proposed for clinical studies.

8.3 The prototype clinical system

8.3.1 Clinical system with old MCA

Having decided that a ^{153}Gd source was the optimum source, a more active (37GBq) source was purchased. This source was then incorporated into a prototype clinical setup which is shown in figure 8.3.1. This system was on a table that could be adjusted in height. On the table were arrangements to keep the axis of the source and the detector perpendicular. These arrangements allowed the source to be moved both perpendicular and parallel to its axis. The detector also could be moved on rails perpendicular to its axis. The position of the detector was arranged such that the front surface of the collimator was flush with the table. A chair with a modified back position was also made, in order to allow a patient to be seated with back support during a measurement.

In order that a significantly more active ^{153}Gd source would not saturate the detection electronics it would need to be moved away from the body (phantom). With the collimation used in previous experiments this would mean that an area greater than necessary would be irradiated. The work described earlier (section 3.4) indicated that if too great an area were irradiated the detection limit would be reduced. Therefore extra collimation plates were made that

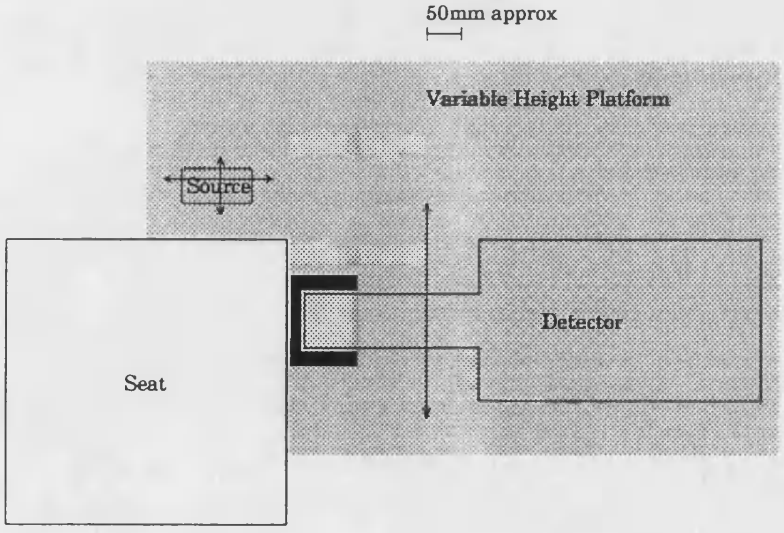

Figure 8.3.1 - Schematic diagram of the prototype clinical system

could be bolted on to the front of the source collimator in order to reduce the beam angle. These extra collimation plates are illustrated in figure 8.3.2.

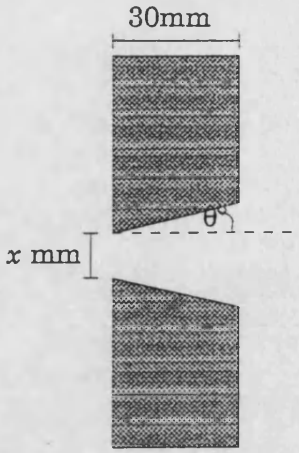

x =	θ =
5.0mm	6°
6.5mm	8°
8.0mm	10°

Figure 8.3.2 - Illustration of extra collimating plates

These collimation plates gave a discrete number of source to kidney distances for which the whole kidney volume would just be irradiated. In order to give extra flexibility an extra collimating 'leaf' was attached to the collimating plate, on the detector side of the source beam. This 'leaf' (which was mounted on a 0.5mm/turn screw thread) could then be moved parallel with the detector axis, so that no tissue between the kidney and skin surface closest to the detector would be irradiated. The extra collimation that the 'leaf' afforded, reduced any unnecessary background under the fluorescence peaks.

The above prototype was then evaluated using a very large tank of water (570 × 300 × 300mm), with the kidney phantom suspended in it, placed on a trolley in the position where the patient would sit. The kidney phantom was placed at the standard lateral depth of 50mm and posterior depth of 30mm used in previous evaluations. The detector with collimator was aligned with the kidney, and placed against the surface of the tank. The 6° extra collimating plate was attached to the front of the source collimator and the extra collimating leaf was moved in seven turns from the edge of the beam. The source to kidney surface distance (SKD) was 275mm.

With this experimental arrangement a detection limit of 40μg g^{-1} was achieved, as compared with 57μg g^{-1} with the previous source at a source to skin distance of 45mm, with a measurement time of 30 minutes. By using the count rate at the MCA and the MCA dead-time, a calculation of the expected difference in

the detection limit can be made. The count rate with the new source was 25 000 cs^{-1} (at the amplifier) as opposed to 8000 cs^{-1} with the old source. The dead-time on the MCA had increased from around 10% to around 32%. Multiplying the MCA live-time by the count rate, leads to the conclusion that the expected number of total counts recorded in the spectrum would have increased by a factor of 2.25, for the new source as compared with the old source. Since the detection limit is approximately inversely proportional to the square root of the total number of counts (section 3.2), it would be expected that the detection limit would have decreased by a factor of 1.5, which would give an expected detection limit of 38μg g^{-1}, which is close to the observed value of 40μg g^{-1}.

It was therefore concluded that the prototype system was performing as expected from previous results, and that measurements with a detection limit of around 40μg g^{-1} could commence on patients. With the source at such a large distance from the skin, sensitivity could be dramatically improved, probably by at least a factor of 2.5 to 16μg g^{-1} in 30 minutes by purchasing a new ADC with a reduced dead-time per pulse, such as the Canberra model 582 which has a fixed dead-time of 1.5μs per pulse (an improvement on the 25μs we are currently using). Alternatively the time required to achieve a detection limit of 40μg g^{-1} would be reduced to around 5 minutes with this new ADC.

8.3.2 Clinical system with new ADC/MCA

Therefore a Canberra model 582 ADC was purchased together with an Accuspec B MCA to work in conjunction with the analogue to digital converter. The new detection system was tested for resolution at various count rates. The results are given in table 8.3.1. Examining the table leads to the conclusion that the detector resolution falls off quite quickly at high count rates. Therefore the detection limit does not fall as quickly as predicted above. However, the detection limit at high count rate is still below that at low count rate. If a higher count rate is used, this increases the effective dose to the patient.

Count Rate /kHz	System Resolution at Gold $K_{\alpha 1}$ peak /eV
10	320
15	350
20	380
25	400
30	440

Table 8.3.1 - Resolutions of the new detection system at various count rates with a shaping time of 1μs on the pulse shaping amplifier

However since the dose using the old MCA was around 48μSv, even a ten fold increase in dose would still put the dose within category I of the WHO guidelines, and within the range of doses given for a chest X-ray (10μSv - 1.3mSv, NRPB (1986)).

Due to the fact that the resolution of the detector decreases at high count rates it was necessary to rewrite the analysis program such that it could allow for different detector resolutions. (It is this version of the program that is given in appendix A.) At very high count rates a pulse-shaping time of 1μs would be too great, due to amplifier saturation and therefore the pulse -shaping time would need to be reduced; this would lead to further decreases in detector resolution, and consequently detection limit.

8.4 Sensitivity variation with position

It is clear that the sensitivity predicted for 50mm lateral depth and 30mm posterior depth will not be the same for all kidney positions. The lateral depth is the distance between the kidney surface and skin surface in the direction of the source, and the posterior depth is the distance between the kidney surface and skin surface in the direction of the detector. Therefore it was necessary to carry out an evaluation of sensitivity variation with phantom position. To obtain some indication of the sensitivity variation the experiment described below was carried out. However in the clinical situation the source would need to be brought closer as the source decayed. Therefore a calibration would need to be carried out for the collimating plate and skin to kidney distance being used.

Lateral* Depth / mm	Posterior* Depth / mm 30	50	70
30	34652	16065	
	31	*65*	
	31995	18295	
50	26074	14751	8695
	37	*68*	*83*
	26074	15821	9634
70	16974	9362	6127
	56	*84*	*98*
	18189	11639	7052

* Posterior depth: Depth from skin surface to kidney surface in the direction of the detector.
* Lateral depth: Depth from skin surface to kidney surface in the direction of the source.
Table 8.4.1 - Sensitivity variation with kidney position using a 24GBq source with an irradiation time of 20 minutes, in terms of experimental $K_{\alpha 1}$ peak counts, Monte Carlo $K_{\alpha 1}$ peak counts (shown condensed), and detection limit (shown in *italics*)

To evaluate the sensitivity variation with the prototype clinical system a kidney phantom containing 500μg g^{-1} of gold was placed in a very large tank of water (570 × 300 × 300mm) at the position where the patient would sit. The 8° collimating plate shown in figure 8.3.2 was always used with the 'leaf' 11 turns in from the edge of the beam. A source to kidney surface distance (SKD) of 200mm was used. However the source and detector positions were adjusted so that the field of view was aligned with the kidney phantom positioned at different depths. Spectra were recorded over a period of 20 minutes and the activity of the ^{153}Gd source at the time of the experiment was 24GBq. The results given in terms of both $K_{\alpha 1}$ peak counts, and detection limit with this source are given in table 8.4.1. The table also shows the relative sensitivities predicted by the Monte Carlo model for the different kidney positions shown. These agree well with those obtained experimentally and so the model could be used for interpolation of different calibration factors in a clinical situation. (The Monte Carlo model results are normalised to the sensitivity recorded for the 50mm lateral depth / 30mm posterior depth experimental result.)

The results also show that the detection limit increases with depth, and rapidly with posterior depth. Therefore accurate calibration and kidney position

determination are important for measurements on patients.

8.5 Conclusions

A prototype clinical system has now been constructed that gives detection limits that will be clinically useful. A table of calibration data has also been constructed (table 8.4.1) and now the system could be evaluated clinically.

Chapter 9

Clinical Results

9.1 Introduction

Now that a clinical system, with a suitable detection limit had been constructed, a clinical evaluation could be initiated. Ethical committee approval was obtained for this study, and the work carried out is outlined below, together with a discussion of possible errors.

9.2 Clinical Studies

It was suggested that a number of clinical studies should be carried out, as they might provide useful information; these were:

- To compare the level of administered gold with the detected level to assess whether there is any correlation;
- To study the variation of kidney gold with time after cessation of chrysotherapy;
- To compare the detected level in the kidney on patients with proteinuria; and
- To compare levels in the kidney for orally and intravenously administered gold, to see whether there are significant differences.

These studies would obviously require the gold level in the kidney to be measured for a large number of patients with varying clinical histories.

The protocol that was adopted for patient measurements is now described briefly. Before any measurements were performed a consent form (Appendix E) was signed by the patient. The procedure for a gold determination was that the depth of the patient's right kidney was first determined, in both a lateral and posterior direction, from an ultrasound scan with the patient in a seated position. The posterior position of the kidney was also marked on the skin of the patient at this stage. The patient was then seated in a high-backed chair and the source and detector adjusted such that their axes intersected at the

centre of the patient's kidney. The source to skin distance was always arranged such that the kidney diameter was just irradiated. A number of collimating plates were available, as described earlier, so that the source could be moved closer to the patient as it decayed in order to maintain the count rate. A spectrum was then recorded for 30 minutes on the multi-channel analyser. This spectrum was then analysed on a personal computer using the Marquadt non-linear least squares fitting algorithm to find the size of the fluorescence peaks in terms of counts (Appendix A). Measurements have now been completed on 12 patients, and the raw results are shown in table 9.2.1. The table gives the number of counts in the gold $K_{\alpha 1}$ peak found by the fitting program together with the uncertainty in this number of counts, an outline of the clinical history of the patient and the depth of the kidney. (The number of counts in the $K_{\alpha 2}$ peak would give no extra information, since the relative size of the $K_{\alpha 1}$ and $K_{\alpha 2}$ peaks was fixed in the fitting program.) It is clear that in order to convert number of counts in the fluorescence peak into a gold concentration in the kidney, a calibration factor is required. These calibration factors could be determined during phantom studies, with a kidney phantom placed at a similar position to that measured for the patient. However the Monte Carlo model (chapter 5) was used to interpolate between the limited

Patient Number	Total Gold / mg	Administration Method	Posterior Depth / mm	Lateral Depth / mm	Therapy Ceased	$K_{\alpha 1}$ Peak / Counts
1	2630	IV	36	36	2/92	859± 578
2	260	IV	31	40	9/80	NRF
3	6000	IV	47	32	8/90	1305± 891
4	6650	IV	71	64	-	2495±1335
5	1000	IV	20	21	10/90	NRF
6	4870	IV	62	60	-	559± 503
7	4500	IV	30	51	6/91	3941±1295
8	4290	IV	25	29	4/92	10326±1434
9	6320	IV	46	27	6/92	1955± 630
10	8000	IV	25	25	11/91	1381± 839
11	3750	IV	40	24	7/92	3336± 764
12	10480	IV	31	60	-	3158±1109

NRF - Peak fitting program unable to produce a reliable fit

Table 9.2.1 - Raw clinical results

number of experimentally determined sensitivities given in the last chapter.

During patient studies, it was noted that the count rate monitor attached to the pulse-shaping amplifier (part of the detection system electronics) sometimes recorded a higher count rate in the clinical measurement than during the equivalent phantom study. Experimental work was therefore carried out to establish whether this was due to the irregular shape of patients. In this experimental study, the large cuboidal body phantom (that had been used previously) was replaced by two different body phantoms in turn. The first was a large cylindrical tank of 300mm diameter and with vertical sides; the second was a bucket which had an upper diameter of 250mm and a lower diameter of 170mm, and height of 240mm. Therefore the bucket had sloping sides and it was not possible to push the detector collimator flush against the surface. The different body phantoms were placed in the middle of the clinical measurement system in the position where the patient would sit. A kidney phantom containing 500μg g^{-1} of gold was suspended in the body phantom, at a number of average depths. The 8° collimating plate was used with the 'leaf' in 11 turns from the edge of the beam. A source to kidney phantom surface distance (SKD) of 200mm was always used. The source and detector positions were adjusted so that the field of view was aligned with the kidney phantom positions. Spectra were recorded over a period of 20 minutes.

The spectra recorded were then analysed using the peak fitting program (Appendix A) and the number of counts in the $K_{\alpha 1}$ peak together with the count rate measured at the pulse-shaping amplifier are given in table 9.2.2. Table 9.2.2 also gives the results for a cuboidal body phantom (in a similar experimental arrangement to other body phantoms) taken from table 8.4.1. The results for the curved phantoms have been normalised to a source activity of 24GBq to make them comparable with the results for the cuboidal phantom. The results clearly show that the number of counts in the $K_{\alpha 1}$ peak does not vary significantly between the studies, however the count rate recorded for the

Lateral* Depth / mm	Posterior* Depth / mm 30	50	70
30	34652 (26)	15065 (19)	
	31724 (27)	*16217* (20)	
	35100 (31)	16200 (23)	
50	26074 (22)	14751 (17)	8695 (11)
	27145 (23)	*13245* (17)	*9130* (11)
	27033 (27)	14194 (19)	8344 (12)
70	16974 (17)	9362 (13)	6127 (8)
	20470 (17)	*10232* (12)	*6041* (8)
	21608 (22)	10030 (16)	6803 (9)

* Posterior depth: Depth from skin surface to kidney surface in the direction of the detector.
* Lateral depth: Depth from skin surface to kidney surface in the direction of the source.

Table 9.2.2 - Sensitivity variation with kidney position using a 24GBq source with an irradiation time of 20 minutes, in terms of experimental $K_{\alpha 1}$ peak counts. Count rates in kilohertz for these experimental results are given in parentheses. (Cuboidal tank results are shown in plain text, cylindrical tank results are shown *in italics*, and bucket results are shown in condensed text)

bucket was usually higher than that recorded for the other phantoms.

The results of this study suggest that the higher count rate recorded in some of the patient measurements is due to the fact that the detector collimator was not pushed up right against the skin of the patient. The effects of a gap between the detector collimator and the patient's skin therefore need to be considered. This gap would cause the source to irradiate a small amount of tissue between the posterior kidney surface and the patient's skin. Thus an increased count rate would probably be observed. However it is unlikely that the gap would cause a reduction in the number of fluorescence counts recorded, since the whole kidney will still be irradiated, as illustrated in figure 9.2.1. Even if the side of the kidney furthest from the detector was not completely irradiated, it is unlikely to cause a large error in the number of fluorescence counts recorded due to the significant variation in sensitivity over the kidney volume found from the results of the Monte Carlo model (chapter 5).

It is concluded that the calibration factors derived from the table in the previous chapter are accurate, and for other kidney depths (found in practice) the Monte Carlo model can be used for interpolation. Therefore the

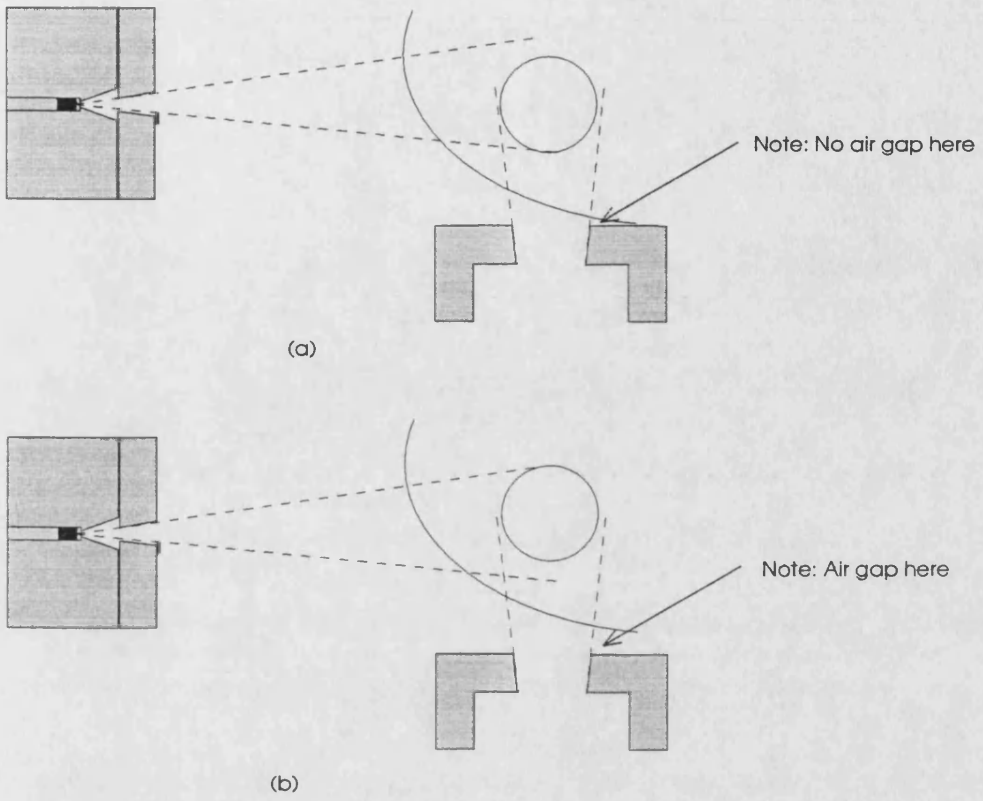

Figure 9.2.1 - Illustration of that both (a) without an air gap and (b) with a limited air gap between the detector collimator and the patient the whole kidney is still irradiated due to the absence of the extra collimating leaf on the side of the kidney furthest from the source

Patient Number	Kidney Gold Conc. / μg g^{-1}	Patient Number	Kidney Gold Conc. / μg g^{-1}
1	24± 15	2	<42
3	31± 21	4	233±125
5	<15	6	60± 55
7	81± 26	8	119± 17
9	40± 13	10	17± 10
11	82± 19	12	84± 29

Table 9.2.3 - Gold concentrations in the right kidneys of chrysotherapy patients (Where no reliable fit could be made to the fluorescence peaks a gold concentration less than the detection limit is indicated)

concentration of gold remaining in the kidneys of the patients in table 9.2.1 are given in table 9.2.3. For the patients where no reliable fit (NRF) could be made by the fitting program, a value of gold concentration less than the detection limit of the measurement system is indicated in table 9.2.3. The calibration factors used were either obtained from a phantom study, or interpolated from existing phantom study results using the Monte Carlo program. The

calibration factors were applied after the raw results had been corrected for the decay of the ^{153}Gd source.

9.3 Uncertainties in Clinical Results

It is clear that the uncertainties returned by the peak fitting program are not the only source of uncertainty in a clinical measurement. Other sources of uncertainty will now be discussed in the following sections.

9.3.1 Uncertainties in kidney depth determination

The kidney depth determination is actually prone to some error. The depth required is from the kidney surface to the uncompressed skin. The problem is that in order to produce a scan, some pressure has to be applied to the ultrasound transducer. To try and minimise this error the pressure on the transducer was gradually released, until the picture on the scanner screen began to disappear, the picture was then captured and the ultrasound scanner software was used to make a depth determination. This problem of compressing the soft tissue between the kidney and the skin may lead to around 2mm error in the depth determination. The uncertainty that this error (in depth) will give in the gold concentration depends on the calibration factor, which in turn depends on the absolute position of the kidney. For a typical kidney depth of 50mm laterally and 30mm in the posterior direction, erroneous depth determinations of 48mm and 28mm respectively would give an error in the calibration factor of 6%. (A depth determination that is too small is most probable due to tissue compression.)

9.3.2 Uncertainties due to patient movement

Unlike an inanimate phantom, a patient is bound to move at least to some extent during a measurement. This movement is of two types, firstly the whole trunk of the patient can move and secondly the kidney of the patient will move due to respiration. The movement of the kidney due to respiration was limited (this could be seen on the ultrasound scan), and an average position was taken.

Other movements of the patient had to be watched for, for example if the patient slouched, they were asked to sit up again. During the initial set up, care was taken to make sure that the detector collimator was pushed up against the patient's skin, the position of the patient could thus be easily checked from time to time during the measurement. Therefore the effects of patient movement were minimised, and it is thought that this type of error did not lead to significant errors in the final gold concentration.

9.3.3 Non-uniform distribution of gold in the kidney

It has been assumed all through the project that the distribution of gold in the kidney is uniform. However the results of Gottlieb *et al* (1972) suggest that higher concentrations of gold are to be found in the renal cortex (the outer layer of the kidney) than the medulla. It has already been shown by the Monte Carlo model, described in chapter 5, that the greatest proportion of the fluorescence signal comes from the part of the kidney nearest the surface. In fact, for a typical kidney, around 40% of the gold fluorescence comes from the 15mm closest to the detector. There is therefore a very significant contribution from other parts of the kidney, including the renal medulla. Hence the gold concentrations quoted in the results can only be seen as *an average* concentration, and as absolute values must be interpreted with some caution. However the values may be compared with each other, as relative values, with a good degree of confidence, as the proportion of signal from the cortex or medulla does *not* vary rapidly with kidney position.

9.4 Conclusions

The gold content of the kidney of a number of patients has now been determined successfully. The uncertainty in the concentration in the gold in the kidney is in most cases quite large, and the figure itself needs to be treated with some caution since a uniform gold distribution in the kidney is assumed. The range of gold concentrations found was also quite large, and perhaps reflects the wide range of clinical histories of the patients involved in the study.

It is obvious that more data still needs to be collected before any clinical conclusions can be drawn, however it is possible to make a few observations on some apparent trends, which although are far from conclusive may be reinforced by further patient measurements.

In order to look for trends the gold concentration found in the clinical studies needs to be plotted against various parameters, such as total gold administered and time since cessation of gold therapy. The level of gold in the kidneys of patients just after the onset of proteinuria also needs to be compared. The plots of gold concentration in the kidney against total gold administered and time since cessation of therapy are shown in figures 9.4.1 and 9.4.2. We still have insufficient data on the level of gold in the kidney just after the onset of proteinuria to draw even a tentative conclusion, and still have not measured the gold concentration in any patients having oral gold therapy, so it is obviously impossible to make any observation concerning the differences between oral and intravenous therapy. Figure 9.4.1 shows that there appears to be no correlation between the total gold administered and the gold concentration found in the kidney. However figure 9.4.2 shows that there is a

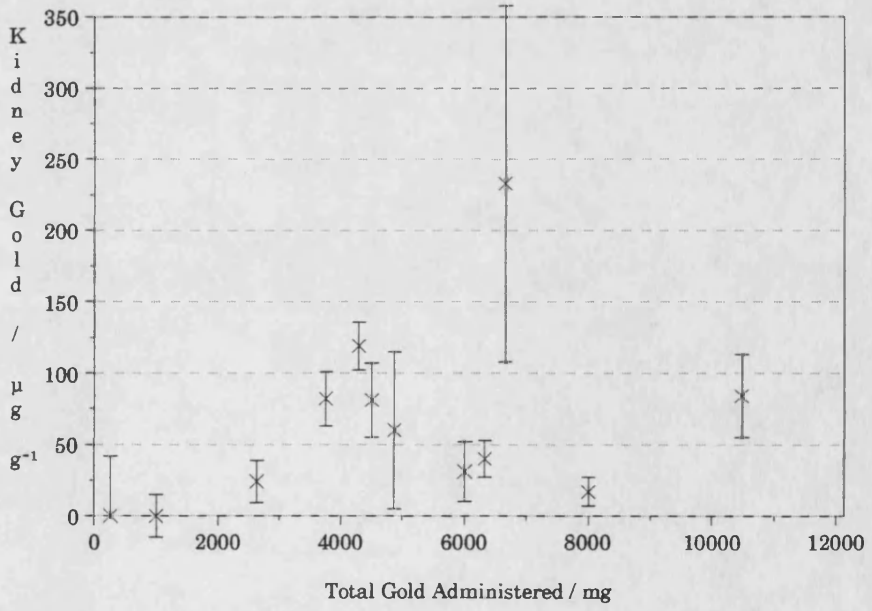

Figure 9.4.1 - Plot of total gold administered against gold concentration found in the kidney

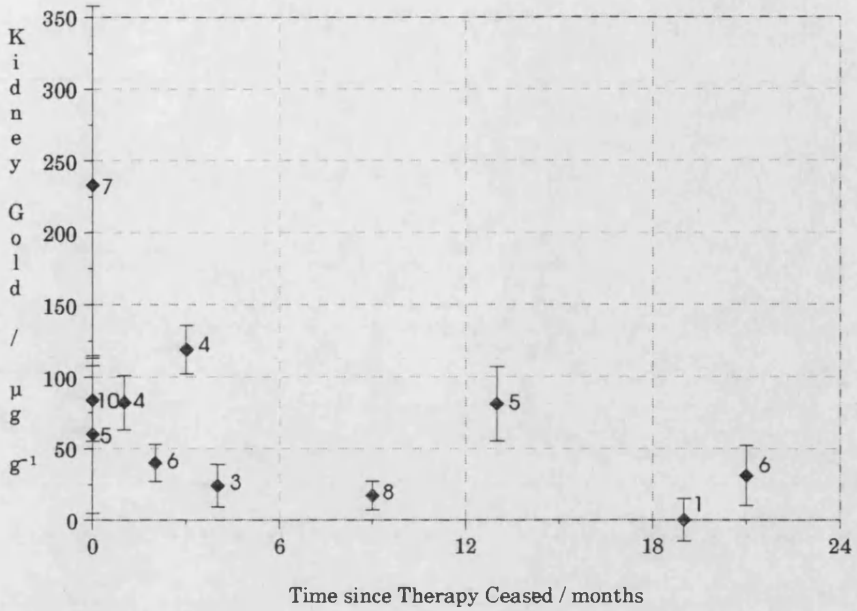

Figure 9.4.2 - Plot of time since cessation of therapy against gold concentration found in the kidney. (The figures next to the experimental points show the total amount of gold administered to the nearest gram)

possible fall off in the amount of gold remaining in the kidney with time after therapy has ceased. The figure also shows the total gold administered (to the nearest gram) next to each experimental point.

In conclusion it is clear that a mobile measurement system that is capable of determining trace levels of gold *in vivo* has been constructed; and more clinical data needs to be collected before any definite conclusions can be drawn.

Chapter 10

Conclusions and Further Work

Other uses for the gold measurement system

Now that the *in vivo* X-ray fluorescence system has been developed it could easily be adapted for the determination of other heavy metals *in vivo*. For metals of atomic number, Z, close to gold (Z=79), such as platinum (Z=78), mercury (Z=80) and lead (Z=82), it is likely that the system could be used with the same radiation source. However for lower atomic number metals, such as cadmium (Z=48), an alternative radiation source would have to be sought. It is possible that for cadmium determination ^{241}Am could be used, since it is commercially available in high activities. However it may be that the lower energy fluorescence of cadmium (~23keV) may give the system insufficient sensitivity at large kidney depth. A feasibility study into an X-ray fluorescence system for cadmium using ^{241}Am as a radiation source could be carried out either experimentally or by adapting the Monte Carlo model.

Possibilities for improving the detection limit

The current lower detection limit of the X-ray fluorescence measurement system seems to governed by the count rate/energy throughput that can be handled by the germanium detector (chapter 8). However most of the radiation entering the detector is of no assistance to the X-ray fluorescence measurement. Therefore if this radiation could be prevented from entering the detector there would be no detriment to the measurement. In fact the removal of this radiation would increase the count rate of useful photons that could be handled by the detector, and may therefore improve the detection limit that can be achieved. It is possible that some of the surplus radiation could be prevented from entering the detector by placing a metal foil across the entrance to the detector. If a metal foil with a K edge of energy just above the fluorescence peaks of interest were used, it would act as a 'bandpass' filter, as illustrated (for gold) in figure 10.1. For gold (Z=79) such a filter would be

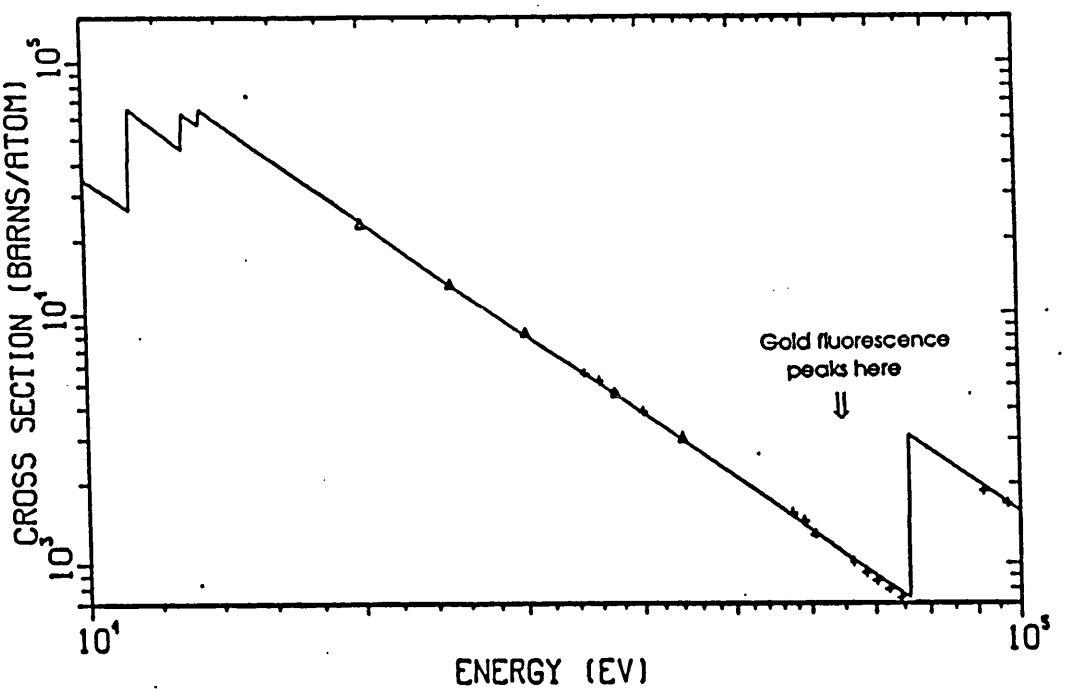

Figure 10.1 - Illustration of Iridium K edge filter for gold

iridium (Z=77). Iridium foil is very expensive (~£1000), and this experiment might not be affordable. An experiment that might be performed to evaluate the magnitude of the improvement in detection limit using this method is to look for iridium (Z=77) fluorescence from a phantom filled with iridium chloride, with and without a tungsten filter (Z=74), which is inexpensive. Using the method described above it is possible that an X-ray fluorescence system could be built which gives an improved detection limit.

Another method by which detection limits could be improved by up to around 40% (section 8.2) is by the use of a partially polarized X-ray source (chapter 7). However the use of a partially polarized X-ray source would require a 150+kVp constant potential X-ray generator, and a dedicated room. The measurement system would then no longer be mobile. It is also unlikely that the extra expense incurred in building such a system could be justified.

CONCLUDING REMARKS

A mobile system that is capable of detecting trace levels of gold *in vivo* has been designed, constructed and evaluated. The construction of such a

measurement system was the primary aim of the project. The measurement system has been designed by consideration of the underlying physical principles involved. The success of the Monte Carlo model clearly demonstrates that all the relevant interactions of ionising radiation with matter have been understood. A number of different methods of excitation have been considered, including different radio-isotope sources, radio-pharmaceuticals (Shakeshaft *et al*, 1991), and X-ray sources. Of the possible radiation sources ^{153}Gd was selected as the source best suited to local needs. The detection system has been optimised for the best detection limit with this radio-isotope source, by consideration of other parameters such as collimation. The early clinical results reported show that a wide range of gold concentrations can be found in the kidney following chrysotherapy. However more data still needs to be collected before any significant clinical conclusions can be drawn; although there are some indications that the amount of gold remaining in the kidney is not related to total dosage, and reduces with time.

Bibliography

Ahlgren L. and Mattsson S. (1979). An X-ray fluorescence technique for *in vivo* determination of lead concentration in a bone matrix, *Phys. Med. Biol.* **24** 136-145.

Ahlgren L. and Mattsson S. (1981) Cadmium in man measured *in vivo* by X-ray fluorescence analysis, *Phys. Med. Biol.* **26** 19-26.

Al-Sadhan F.A., Jones S.J., Evans C.J., Jaib M.B.M. and Morgan W.D. (1989). A comparison of ^{57}Co and $^{99}Tc^{m}$ sources for the *in vivo* measurement of platinum in tumours, *Proceedings of the 2nd International Workshop on XRF and PIXE in the Life Sciences* 29-30 June, Capri, Italy (Private Communication).

Bevington P.R. (1969) *Data Reduction and Error Analysis for the Physical Sciences*, New York: McGraw-Hill.

Bascó J., Izonyi I. and Dezsö B. (1988) Determination of gold accumulation in human tissues caused by gold therapy using X-ray fluorescence analysis, *Appl. Radiat. Isot.* **39** 323-326.

Birch R., Marshall M. and Ardran G.M. (1979) *Catalogue of Spectral Data For Diagnostic X-rays*, London:Hospital Physicists' Association.

Bloch P. and Shapiro I.M. (1981) An X-ray fluorescence technique to measure the mercury burden of dentists *in vivo*, *Med. Phys.* **8** 308-311.

Block W.D. and van Goor K. (1956). *Metabolism, pharmacology and Therapeutic uses of gold compounds*, Springfield: Charles C. Thomas.

Chettle D.R., Scott M.C. and Somervaille L.J. (1989). Improvements in the precision of *in vivo* bone lead measurements, *Phys. Med. Biol.* **34** 1295-1300.

Christofferson J-O. and Mattsson S. (1983). Polarised X-rays in XRF analysis for improved *in vivo* detectability of cadmium in man, *Phys. Med. Biol.* **28** 1135-1144.

Collins A.J. (1987). Gold treatment for rheumatoid arthritis: Reassurance on proteinuria, *Br. Med. J.* **295** 739-740.

Dutton J., Evans C.J., Samat S.B., Morgan W.D. and Sivyer A. (1985). Feasibility studies of X-ray fluorescence analysis for *in vivo* determination of platinum and other heavy metals, *Adv. X-ray Anal.* **28** 145-154.

El-Sharkawi A.M., Morgan W.D., Cobbold S., Jaib M.B.M, Evans C.J., Somervaille L.J., Chettle D.R. and Scott M.C. (1986). Unexpected mobilisation of lead during cis-platin chemotherapy, *Lancet* **ii** 249-250.

Evans R.D. (1955). *The Atomic Nucleus*, New York: McGraw-Hill.

Girdwood R.H. (1974). Death after taking medicaments, *Br. Med. J.* **i** 501-4.

Gottlieb N.L., Smith P.M. and Smith E,M. (1972). Tissue gold concentration in a rheumatoid arthritic receiving chrysotherapy, *Arth. Rheum.* **15** 16-22.

Hall C.L., Fothergill N.J., Blackwell M.M., Harrison P.R., MacKenzie J.C. and MacIver A.G. (1987). The natural course of gold nephropathy: long term study of 21 patients, *Br. Med. J.* **295** 745-748.

Hall C.L. and Tighe R. (1989). The effect of continuing penicillamine and gold treatment on the course of penicillamine and gold nephropathy, *Br.J.Rheum.* **28** 53-57.

Hubbell J.H. (1969). *Photon Cross Sections, Attenuation Coefficients, and Energy Absorption Coefficients From 10keV to 100 GeV*, NSRDS-NBS **29.**

Hubbell J.H. (1982). Photon Mass Attenuation and Energy-absorption Coefficients form 1keV to 20MeV, *Int. J. Appl. Radiat. Isot.* **33** 1269-1290.

ICRP (1988). *Radiation Dose to Patients from Radio-pharmaceuticals* **Publication 53,** Oxford:Pergamon Press.

ICRP (1990). *1990 Recommendations of the International Commission on Radiological Protection*, **Publication 60,** Oxford:Pergamon Press.

ICRU (1980). *Radiation Quantities and Units* Report **33,** Washington:ICRU.

Jeffrey D.A., Biggs D.F., Percy J.S. and Russell A.S. (1975). Quantitation of gold in skin in chrysiasis, *J. Rheumatology* **2** 28-35.

Jonson R., Mattsson S. and Unsgaard B. (1987) A method for *in vivo* analysis of platinum after chemotherapy with cis-platin, *Phys. Med. Biol* **33** 847-857.

Knoll G.F. (1979) *Radiation detection and measurement*, USA: John Wiley & Sons.

Laird E.E., Chettle D.R. and Scott M.C. (1982). The factors affecting *in vivo* X-ray fluorescence measurements of lead in bone, *Nucl. Inst. Meth.* **193** 377-382.

Landrigan P.J. (1989). The toxicity of lead at low dose, editorial. *Br. J. Indust. Med.* **46** 593.

Maisey M. (1980). *Nuclear medicine*, London: Update Books.

Marquadt D.W. (1963). An algorithm for least squares estimation of non-linear parameters, *J. Soc. Indust. Appl. Math.* **11** 431-441.

NRPB (1986) *R200 - A national survey of dose to patients undergoing a selection of routine X-ray examinations in English hospitals*, London: HMSO.

Padikal T.N. and Fivozinksy S.P. (1982). *Medical Physics Data Book*, NSRDS-NBS **138** 21.

Press W.H., Flannery B.P., Teukolsky S.A. and Vettering W.T. (1988).

Numerical Recipes in C - The art of scientific computing, Cambridge: Cambridge University Press.

Price J., Baddeley H., Kenardy J.A., Thomas B.J. and Thomas B.W. (1984). *In vivo* X-ray fluorescence estimation of bone lead concentrations in Queensland adults, *Br. J. Radiol.* **57** 29-33.

Rosenthal M.S. and Henry L.J. (1990). Scattering in uniform media, *Phys. Med. Biol.* **35** 265-274.

Salom E.B., Hubbell J.J.H. and Scofield J.H. (1988). X-ray attenuation cross sections for energies 100ev to 100keV and elements Z=1 to Z=92, *Atomic Data and Nuclear Tables* **38** 1-197.

Siemens. (1990) *Medical Engineering: Data, Formulas, Facts*, Berlin:Siemens Aktiengesellschaft.

Silverberg D.S., Kidd E.G., Shnitka T.K. and Ulan R.A. (1970). Gold Nephropathy: a clinical and pathological study, *Arth. Rheum.* **13** 812-8.

Schmidt O. (1941) Chrysiasis, *Arch. Dermatol.* **44** 446-452.

Scott J. and Lillicrap S. (1988) ^{133}Xe for X-ray fluorescence assessment of gold *in vivo*, *Phys. Med. Biol.* **33** 859-864.

Shakeshaft J., Lillicrap S. and Evans M. (1991) $^{99}Tc^{m}$ radio-pharmaceuticals for the x-ray fluorescence assessment of gold *in vivo*, *Phys. Med. Biol.* **36** 531-536.

Snyder W.S., Ford M.R., Warner G.G. and Watson S.B. (1975) *"S" absorbed dose per unit cumulated activity for selected radio-nuclides and organs*, MIRD Pamphlet N°11, New York:Society of Nuclear Medicine.

Somervaille L.J., Chettle D.R. and Scott M.C. (1985) *In vivo* measurement of lead bone using X-ray fluorescence, *Phys. Med. Biol.* **30** 929-943.

Todd A.C. (1989). Thesis for Ph.D., University of Birmingham.

Varnell L. and Trishcuk J. (1965). A peak fitting and calibration program for Ge(Li) Detectors, *Nucl. Inst. Meth.* **76** 109-114.

Vernon-Roberts B., Doré J.L., Jessop J.D. and Henderson W.J. (1976) Selective concentration and localization of gold in macrophages of synovial and other tissues during and after chrysotherapy in rheumatoid patients, *Ann. Rheum. Dis.* **35** 477-486.

Vinson J.A. (1990). A New form of gold for oral and topical treatment of rheumatoid arthritis, *Proceedings of 2nd International Conference on Gold and Silver in Medicine*, 9-11 April, Manchester, England (Private Communication).

Virgil (19BC). *Aeneid* III, 1-55.

Wielopolski L., Ancona R.C., Mossey R.T., Vaswani A.N. and Cohn S.H. (1985). Nuclear resonance scattering measurement of human iron stores, *Med. Phys.*

12 401-404.

Wielopolski L., Rosen J.F., Slatkin D.N., Vartsky D., Zhang R., Kalef-Ezra J.A., Rothman J.C., Maryanski M. and Jenks S.T. (1989). *In vivo* measurement of cortical bone lead using polarized X-rays, *Med. Phys.* 16 521-528.

World Health Organisation (1977). *Use of Ionising Radiations and Radio-nuclides on Human Beings for Medical Research, Training and Non-medical purposes*, Technical Report Series Nº 611, Geneva: WHO.

Appendix A

Peak Fitting Program

A1 analyse.c

```
/* Program for analysis of data from MCA                                    */
/* Requires files in format the same as XXX.DAT files from Canberra         */
/* Packard Accuspec control software                                        */

/* Modified 22/10/90 Re-iterate on negative amplitude                       */
/* Modified 13/12/90 Guess from Alphal Height rather than Alpha 2           */
/* Modified 05/03/91 New resolution for new detector                        */
/*                   Re-Iterate on bad position for peaks                   */

/* Major revision 04/03/92 Converted from EG&G file format to Canberra*/
/*                         format, and to Zortech C                         */
/* Modified 12/03/92 Read configuration from disk                           */
/* Modified 14/07/92 Improved date_decode routine                           */
/* Modified 15/07/92 Iteration of background first                          */

/*************************************************************************/
/* This program must be linked with a double precision version of        */
/* a library of the routines from Numerical Recipes in C - The art       */
/* of scientific computing by Press WH et al (CUP)                       */
/*                                                                       */
/* In the double precision version  float    =>    double               */
/*                                  double   =>    long double          */
/*************************************************************************/


#define TRUE -1
#define FALSE 0

#define FG_ALIGN_BL 0
#define FG_ALIGN_TL 1
#define FG_ALIGN_BR 2
#define FG_ALIGN_TR 3

#define CHANNELS 2048
#define MAX_CHN_FILE_LEN 9216
#define N_PARMS 10
#define N_BACK_FIT 35

#define SQRT_2PI 2.506628275
#define TWICE_SQRT2 2.828427125
#define SQRT2 1.414213562


#include <math.h>      /* ANSI standard */
#include <stdio.h>     /* ANSI standard */
#include <stdlib.h>    /* ANSI standard */
#include <disp.h>      /* Header for display  routines in Zortech C */
#include <fg.h>        /* Header for graphics routines in Zortech C */
#include <nr.h>        /* Numerical recipes library header */
#include <nrutil.h>    /* Numerical recipes utilities library header */


void lin_lin(double *, double *, double *, int, int, int);
int data_fetch(char *,int *,double *,char *,char *,char *,char *,double *,double *,d
ouble *,double *,double *);
void double_peak(double,double *,double *,double *,int);
float float_decode(char *);
```

```
long int_decode(char *);
short word_decode(char *);
void parms_display(double *,double **,int);
void peak_count(int,int,double *,double *,double *,double *,double *);
void text_display(char *,char *,char *,char *,char *,double,double,int);
void date_decode(int, int *, int *);

static double sqrarg;

/* Increase stack size from default of 2048 */
unsigned _stack = 32768;

void date_decode(int julian, int *mm, int *id)
{
    /* On entry: julian contains day number 1 - 366  */
    /* On exit:  mm contains the month               */
    /*           id contains the day                 */
    static int month_cuml[13] = { 0, 31, 60, 91, 121, 152, 182, 213, 244, 274, 305,
335, 366};
    int i;

    if (julian > month_cuml[12]) nrerror("Bad date in date_decode");
    i = 0;
    while (julian > month_cuml[i+1])
        i++;
    *id = julian-month_cuml[i];
    *mm = i+1;
}

void fg_puts_x(fg_color_t color, int mode, int mask, int rotation, fg_coord_t x, fg_
coord_t y, char *out_string, fg_pbox_t clip, int align)
{
    fg_coord_t sx, sy, nx, ny;

    sx = 0, sy = 0;
    fg_adjustxy(rotation, strlen(out_string), &sx, &sy, fg_charbox);
    nx = x, ny = y;
    switch (align) {
      case FG_ALIGN_BL:
        switch (rotation) {
          case FG_ROT90:
            nx += fg_charbox[FG_X2];
            break;
          case FG_ROT180:
            nx -= sx;
            ny += fg_charbox[FG_Y2];
            break;
          case FG_ROT270:
            ny += sy;
            break;
        }
        break;
      case FG_ALIGN_TL:
        switch (rotation) {
          case FG_ROT0:
            ny -= fg_charbox[FG_Y2];
            break;
          case FG_ROT90:
            nx += fg_charbox[FG_X2];
            ny -= sy;
            break;
          case FG_ROT180:
            nx -= sx;
            break;
        }
        break;
      case FG_ALIGN_BR:
        switch (rotation) {
          case FG_ROT0:
```

```
            nx -= sx;
            break;
          case FG_ROT180:
            ny += fg_charbox[FG_Y2];
            break;
          case FG_ROT270:
            nx -= fg_charbox[FG_X2];
            ny += sy;
            break;
        }
        break;
      case FG_ALIGN_TR:
        switch (rotation) {
          case FG_ROT0:
            nx -= sx;
            ny -= fg_charbox[FG_Y2];
            break;
          case FG_ROT90:
            ny -= sy;
            break;
          case FG_ROT270:
            nx -= fg_charbox[FG_X2];
            break;
        }
        break;
    }
    fg_puts(color, mode, mask, rotation, nx, ny, out_string, clip);
}

void lin_lin(double *x,double *y1, double *y2, int npts, int roi1,int roi2)
{
    double x_scale, y_scale, y_max, y_min;
    int i;
    fg_coord_t xs, ys, x11, y11;
    fg_box_t box_coord;
    fg_line_t line_coord;
    char temp_ch, *tempbuf;

    /* Free space for temporary string buffer */
    tempbuf=(char *)malloc(80*sizeof(char));
    if (!tempbuf) nrerror("allocation failure in lin_lin()");
    /* Set up variables */
    y_min=1.0E38;
    y_max=-1.0E38;
    for (i=1; i<=npts; i++) {
        if (y1[i]<y_min) y_min=y1[i];
        if (y2[i]<y_min) y_min=y2[i];
        if (y1[i]>y_max) y_max=y1[i];
        if (y2[i]>y_max) y_max=y2[i];
    }
    /* Select graphics mode */
    fg_init();
    xs = (fg_coord_t)(((long)(fg_displaybox[FG_X2]-fg_displaybox[FG_X1])*80L)/100L);
    ys = (fg_coord_t)(((long)(fg_displaybox[FG_Y2]-fg_displaybox[FG_Y1])*68L)/100L);
    x_scale=(double)(xs)/(roi2-roi1);
    y_scale=(double)(ys)/(y_max-y_min);
    /* Axes lower left */
    x11 = fg_displaybox[FG_X1]+(10*(fg_displaybox[FG_X2]-fg_displaybox[FG_X1]))/100;
    y11 = fg_displaybox[FG_Y1]+(16*(fg_displaybox[FG_Y2]-fg_displaybox[FG_Y1]))/100;
    /* Now draw axes */
    sprintf(tempbuf, "%.1f", y_min);
    fg_puts_x(FG_WHITE, FG_MODE_SET, 0, FG_ROT0, x11-1, y11, tempbuf, fg_displaybox
, FG_ALIGN_BR);
    sprintf(tempbuf, "%.1f", y_max);
    fg_puts_x(FG_WHITE, FG_MODE_SET, 0, FG_ROT0, x11-1, y11+ys, tempbuf, fg_display
box, FG_ALIGN_TR);
    sprintf(tempbuf, "%.1f", x[roi1]);
    fg_puts_x(FG_WHITE, FG_MODE_SET, 0, FG_ROT0, x11, y11-1, tempbuf, fg_displaybox
, FG_ALIGN_TL);
```

```
    sprintf(tempbuf, "%.1f", x[roi2]);
    fg_puts_x(FG_WHITE, FG_MODE_SET, 0, FG_ROT0, xll+xs, yll-1, tempbuf, fg_display
box, FG_ALIGN_TR);
    box_coord[FG_X1] = xll, box_coord[FG_Y1] = yll;
    box_coord[FG_X2] = xll+xs, box_coord[FG_Y2] = yll+ys;
    fg_drawbox(FG_CYAN, FG_MODE_SET, 0, FG_LINE_SOLID, box_coord, fg_displaybox);
    /* Now plot data */
    line_coord[FG_X1] = xll, line_coord[FG_Y1] = yll+((y1[roi1]-y_min)*y_scale);
    for (i=roi1+1;i<=roi2;i++) {
        line_coord[FG_X2] = xll+(i-roi1)*x_scale, line_coord[FG_Y2] = yll+((y1[i]-y_
min)*y_scale);
        fg_drawline(FG_BLUE, FG_MODE_SET, 0, FG_LINE_SOLID, line_coord);
        line_coord[FG_X1] = line_coord[FG_X2], line_coord[FG_Y1] = line_coord[FG_Y2]
;
    }
    for (i=roi1;i<=roi2;i++)
        fg_drawdot(FG_GREEN, FG_MODE_SET, 0, xll+(i-roi1)*x_scale, yll+((y2[i]-y_mi
n)*y_scale));
    fg_puts(FG_WHITE, FG_MODE_SET, 0, FG_ROT0, 0, 0, "Please press SPACE BAR to con
tinue.", fg_displaybox);
    do {
        temp_ch=getch();
    } while (temp_ch != ' ');
    fg_term();
    free(tempbuf);
}

/*Service routine for read_config - reads an item from file */
/*========================================================== */
int read_item(double *p, FILE *fp, int parm_number)
{
    int n_items;

    n_items = fscanf(fp, "%lf", p);
    if (n_items != 1) {
        fprintf(stderr, "Error in reading parameter %d from configuration file\n", p
arm_number);
    } else
        return FALSE;
}

/*Routine to extract configuration from disk */
/*========================================*/
int read_config(double *p1, double *p2, double *p3, double *p4, double *p5, int *ite
r, int list[])
{
    FILE *fp;
    int i, n_items;

    if ((fp = fopen("ANALYSE.CFG","r")) == NULL)
        return FALSE;
    if (read_item(p1, fp, 1)) return FALSE;
    if (read_item(p2, fp, 2)) return FALSE;
    if (read_item(p3, fp, 3)) return FALSE;
    if (read_item(p4, fp, 4)) return FALSE;
    if (read_item(p5, fp, 5)) return FALSE;
    n_items = fscanf(fp,"%d", iter);
    if (n_items != 1) {
        fprintf(stderr, "Error in reading number of parameters to iterate from confi
guration file\n");
        return FALSE;
    }
    for (i=1; i<=N_PARMS; i++) {
        n_items = fscanf(fp, "%d", &list[i]);
        if (n_items != 1) {
            fprintf(stderr, "Error in reading list item %d from configuration file\n
", i);
            return FALSE;
        }
```

```
    }
    fclose(fp);
    return TRUE;
}

/*Routine to extract data from DATA file on disk */
/*============================================*/
int data_fetch(char *file, int *nofchans, double chan_data[], char desc[], char dete
ct[], char date[], char time[], double *live_time, double *real_time, double *cal_qu
ad, double *cal_slope, double *cal_int)
{
    FILE *filep;
    char buffer[MAX_CHN_FILE_LEN];
    int noread, hh, mm, yy, ss, i;
    long ll;

    if ((filep = fopen(file,"rb"))== NULL) {
      disp_printf("File not found\n");
        return NULL;
    }
    noread = fread(&buffer[0], sizeof(buffer[0]), MAX_CHN_FILE_LEN, filep);
    disp_printf("%d bytes read from file.\n",noread);
    if (((int)buffer[0]!=0x00) || ((int)buffer[0]!=0x00)) {
      disp_printf("This is not a Accuspec data file");
        return NULL;
    }
    /* Set up time */
    ll = int_decode(&buffer[84]);
    hh = (int)(ll/3600L), ll-= (long)(hh)*3600L;
    mm = (int)(ll/60L), ll-= (long)(mm)*60L;
    ss = (int)(ll);
    time[0] = (hh/10) | 0x30;
    time[1] = (hh%10) | 0x30;
    time[2] = ':';
    time[3] = (mm/10) | 0x30;
    time[4] = (mm%10) | 0x30;
    time[5] = ':';
    time[6] = (ss/10) | 0x30;
    time[7] = (ss%10) | 0x30;
    time[8] = (char)(0);
    /* Set up date */
    date_decode(word_decode(&buffer[80]), &mm, &hh);
    date[0] = (hh/10) | 0x30;
    date[1] = (hh%10) | 0x30;
    date[2] = '/';
    date[3] = (mm/10) | 0x30;
    date[4] = (mm%10) | 0x30;
    date[5] = '/';
    yy = (int)(word_decode(&buffer[82]));
    yy %= 100; /* Make the year two digits only */
    date[6] = (yy/10) | 0x30;
    date[7] = (yy%10) | 0x30;
    date[8] = (char)(0);
    *nofchans = (int)(word_decode(&buffer[36]));
    if (*nofchans>CHANNELS) *nofchans = CHANNELS;
    *live_time = int_decode(&buffer[48]) + (double)(word_decode(&buffer[20]))/100.0;
    *real_time = int_decode(&buffer[56]) + (double)(word_decode(&buffer[22]))/100.0;
    *cal_quad = (double)float_decode(&buffer[116]);
    *cal_slope = (double)float_decode(&buffer[112]);
    *cal_int = (double)float_decode(&buffer[108]);
    /* Copy detector description */
    for (i=0;i<15;i++)
       detect[i] = buffer[476+i];
    detect[15] = (char)0;
    /* Copy sample description   */
    for (i=0;i<63;i++)
        desc[i] = buffer[332+i];
    desc[63] = (char)0;
    /* Decode the actual channel data */
```

```
    for (i=1;i<=*nofchans;i++)
      chan_data[i]=(double)(int_decode(&buffer[1020+i*4]));
    if (fclose(filep) != NULL) disp_printf("Unable to close file!");
      return -1;
}


void double_peak(double x, double a[], double *y, double dyda[],
                 int na)
{
    /* Fn is a1*(exp((((x-a2)/a3)^2)/2)+a6*erfc((x-a2)/sqrt2/a3))          */
    /*    +a4*a1*exp((((x-(a2+a5))/a3)^2)+a6*erfc((x-(a2+a5))/sqrt2/a3))   */
    /*    +a7+a8*x+a9*x^2+a10*x^3                                          */
    double e1,e2,ex1,ex2,ef1,ef2;

    if (na != 10) nrerror("Invalid number of args in DOUBLE_PEAK");
    ex1=-(x-a[2])*(x-a[2])/a[3]/a[3]/2.0;
    ex2=-(x-(a[2]+a[5]))*(x-(a[2]+a[5]))/a[3]/a[3]/2.0;
    e1=a[1]*exp(ex1);
    e2=a[4]*a[1]*exp(ex2);
    ef1=a[1]*a[6]*erfcc((x-a[2])/SQRT2/a[3]);
    ef2=a[1]*a[4]*a[6]*erfcc((x-(a[2]+a[5]))/SQRT2/a[3]);
    *y=e1+e2+a[7]+a[8]*x+a[9]*x*x+a[10]*x*x*x+ef1+ef2;
    dyda[1]=(e1+e2+ef1+ef2)/a[1];
    dyda[2]=((x-a[2])/a[3]-2*a[6]/SQRT_2PI)/a[3]*e1+((x-(a[2]+a[5]))/a[3]-2*a[6]/SQR
T_2PI)/a[3]*e2;
    dyda[3]=((x-a[2])/a[3]+2*a[6]/SQRT_2PI)*(x-a[2])/a[3]/a[3]*e1+((x-(a[2]+a[5]))/a
[3]+2*a[6]/SQRT_2PI)*(x-(a[2]+a[5]))/a[3]/a[3]*e2;
    if (a[4]==0.0)
        dyda[4]=0.0;
    else
        dyda[4]=(e2+ef2)/a[4];
    dyda[5]=((x-(a[2]+a[5]))/a[3]-2*a[6]/SQRT_2PI)/a[3]*e2;
    dyda[6]=(ef1+ef2)/a[6];
    dyda[7]=1.0;
    dyda[8]=x;
    dyda[9]=x*x;
    dyda[10]=x*x*x;
}

long int_decode(char *coded)
{
    unsigned short *word;
    long decoded, high_word;

    word = (unsigned short *)coded;
    decoded = (long)word[1];
    decoded |= ((long)word[0])<<16;
    return decoded;
}

short word_decode(char *coded)
{
    short *word;

    word = (short *)coded;
    return word[0];
}

float float_decode(char *coded)
{
    /* This is only correct if compiler uses IEEE floats */
    float decoded;
    char *coded_copy;
    int j;
    short *i, iexp, itmp;

    coded_copy = (char *)&decoded;
    for (j=0; j<4; j++)
```

```
        coded_copy[j] = coded[j];
    i = (short *)coded_copy;
    if (i[0] == 0)
        i[1] = 0;
    else {
        iexp = i[0] & 0x7f80;
        iexp -= 256;
        i[0] &= 0xffff807f;
        i[0] |= iexp;
        itmp = i[1];
        i[1] = i[0];
        i[0] = itmp;
    }
    return decoded;
}

void parms_display(double parms[], double **covar, int error_display)
{
    disp_move(13,0);
    disp_setattr(DISP_NORMAL);
    disp_printf("Parameters:\n");
    if (error_display) {
      disp_printf("K alpha 1: Pos.:  %7.2f (%6.2f) keV\n",(parms[2]+parms[5]),sqrt(c
ovar[2][2]+covar[5][5]));
      disp_printf("           Width: %7.2f (%6.2f) keV\n",parms[3],sqrt(covar[3][3])
);
      disp_printf("           Amp.:  %7.2f (%6.2f)",(parms[1]*parms[4]),sqrt(covar[1
][1]/parms[1]/parms[1]+covar[4][4]/parms[4]/parms[4])*parms[1]*parms[4]);
      disp_move(14,42);
      disp_printf("K alpha 2: Pos.:  %7.2f (%6.2f) keV\n",parms[2],sqrt(covar[2][2])
);
      disp_move(15,42);
      disp_printf("           Width: %7.2f (%6.2f) keV\n",parms[3],sqrt(covar[3][3])
);
      disp_move(16,42);
      disp_printf("           Amp.:  %7.2f (%6.2f)\n",parms[1],sqrt(covar[1][1]));
      disp_printf("Peak shelf ht. :  %7.2f (%6.2f) %%\n",(parms[6]*100),sqrt(covar[6
][6])*100);
      disp_printf("Background: %.2f %+.2fE %+.2fE^2 %+.2fE^3         \n",parms[7],pa
rms[8],parms[9],parms[10]);
    } else {
      disp_printf("K alpha 1: Pos.:  %7.2f keV\n",(parms[2]+parms[5]));
      disp_printf("           Width: %7.2f keV\n",parms[3]);
      disp_printf("           Amp.:  %7.2f",(parms[1]*parms[4]));
      disp_move(14,42);
      disp_printf("K alpha 2: Pos.:  %7.2f keV\n",parms[2]);
      disp_move(15,42);
      disp_printf("           Width: %7.2f keV\n",parms[3]);
      disp_move(16,42);
      disp_printf("           Amp.:  %7.2f\n",parms[1]);
      disp_printf("Peak shelf ht. :  %7.2f %%\n",(parms[6]*100));
        disp_printf("Background: %.2f  %+.2fE %+.2fE^2 %+.2fE^3         \n",parms[7]
,parms[8],parms[9],parms[10]);
    }
    disp_flush();
}

void peak_count(int mean, int extent, double x[], double roi_data[], double parms[],
double *peak, double *back)
{
    int i;
    double btemp;

    *peak=0.0;
    *back=0.0;
    for (i=mean-extent;i<=mean+extent;i++) {
        btemp=parms[7]+parms[8]*x[i]+parms[9]*x[i]*x[i]+parms[10]*x[i]*x[i]*x[i];
        *peak+=roi_data[i]-btemp;
        *back+=btemp;
```

```
    }
}

void text_display(char *filename, char *sample, char *detector, char *date, char *ti
me, double live_time, double real_time, int nofchans)
{
    disp_move(0,0);
    disp_eeop();
    disp_setattr(DISP_NORMAL | DISP_INTENSITY);
    disp_printf("Data analysis program.\n");
    disp_printf("======================\n\n");
    disp_setattr(DISP_NORMAL);
    disp_printf("File: %s\nSample: %s\nDetector: %s\n\n", filename, sample, detector
);
    disp_printf("Recorded on %s at %s.\n", date, time);
    disp_printf("Channels:  1 to %d\n\n", nofchans);
    disp_printf("Live Time: %.2lf secs.\n", live_time);
    disp_printf("Real Time: %.2lf secs.\n\n", real_time);
}

int main(int argc, char *argv[])
{
    /* Variables read in from file / used in initialisation */
    int nofchans;
    double *x, *chan_data;
    double calib_quad, calib_slope, calib_int, live_time, real_time;
    static char time[9],date[9],desc[64],detect[16];
    /* Variables used solely by Marquadt fitting routine */
    static int list_parms[N_PARMS+1];
    static double parms[N_PARMS+1], dummy[N_PARMS+1];
    double **covar,**alpha;
    double *raw_data, *model_data, *x_back, *sigma;
    double alamda,chisq,old_chisq,delta_chisq;
    /* Variables used to denote region of interest */
    int roi1,roi2,npts_roi,roi_offset;
    /* Loop or temporary variables */
    int i,result,iteration=1;
    char temp_ch;
    double d1,d2,d3,d4,d5,q1,qr,e,f,g,h,delta_x;
    /* Variables used in area calculations */
    double area_Ka2,area_Ka1,back_Ka2,back_Ka1,delta_area2,delta_area1;
    double area_Ka2P,area_Ka1P;
    int mean,extent;
    /* Configuration parameters */
    double alpha2_energy, peak_e_diff, rel_peak_height;
    double detector_resoln, shelf_height, alpha1_energy;
    int iter_parms;
    /* List of parameters to iterate with background */
    static int list_back[11] = {-1, 7, 8, 9, 10, 1, 2, 3, 4, 5, 6};
    /* Graphics system variables */
    int gerror;

    /* Declare space to put data from MCA file */
    x=vector(1, CHANNELS);
    chan_data=vector(1, CHANNELS);
    /* Check command line syntax */
    if (argc != 2) {
      fprintf(stderr, "Syntax: analyse <Data File>\n");
        exit(1);
    }
    /* Initialise graphics and display packages */
    disp_setmode(3);
    disp_open();
    disp_usebios();
    gerror = fg_init_all();    /* Set up graphics system */
    if (gerror < FG_EGACOLOR ) {
      fprintf(stderr, "Analysis program requires EGA. (%d)\n", gerror);
        /* exit(2) */;
    }
```

```
    fg_term();
    disp_setattr(DISP_NORMAL | DISP_INTENSITY);
    disp_printf("Data analysis program.\n");
    disp_printf("====================\n\n");
    if (read_config(&alpha2_energy, &peak_e_diff, &detector_resoln, &rel_peak_height
, &shelf_height, &iter_parms, list_parms) != TRUE) {
        fprintf(stderr, "Failed to read configuration from ANALYSE.CFG.\n");
        exit(6);
    }
    alphal_energy = alpha2_energy + peak_e_diff;
    disp_printf("Working on file %s\n",argv[1]);     /* Print filename      */
    disp_setattr(DISP_NORMAL);
    /* First read in data */
    result = data_fetch(argv[1], &nofchans, chan_data, desc, detect, date, time, &li
ve_time, &real_time, &calib_quad, &calib_slope, &calib_int);
    if (result == NULL) exit(3);                /* If error then exit */
    text_display(argv[1], desc, detect, date, time, live_time, real_time, nofchans);
    if (calib_slope==1.0) {
        disp_move(17,0);
        disp_printf("Please enter calibration data:\na = ");
        scanf("%lf", &calib_quad);
        disp_printf("b = ");
        scanf("%lf", &calib_slope);
        disp_printf("c = ");
        scanf("%lf",&calib_int);
    }
    /* Set up x values ready for sending to the graph */
    /* drawing routine.                               */
    for (i=1;i<=nofchans;i++)
      x[i]=(double)(i*i)*calib_quad+(double)(i)*calib_slope+calib_int;
    /* Now set up arrays containing data to be fitted */
    roi1=(int)((alpha2_energy-3.0*detector_resoln*1.0E-3-calib_int)/calib_slope-(dou
ble)N_BACK_FIT);
    roi2=(int)((alphal_energy+3.0*detector_resoln*1.0E-3-calib_int)/calib_slope+(dou
ble)N_BACK_FIT);
    roi_offset=roi1-1;
    npts_roi=roi2-roi1+1;
    fit(&x[roi1-4],&chan_data[roi1-4],8,raw_data,0,&d1,&ql,&d2,&d3,&d4,&d5);
    fit(&x[roi2-4],&chan_data[roi2-4],8,raw_data,0,&d1,&qr,&d2,&d3,&d4,&d5);
    /* Declare space to store ROI counts */
    raw_data = vector(1, npts_roi);
    /* Transfer ROI info */
    for (i=0;i<npts_roi;i++) {
        x[i+1]=x[roi1+i];
      raw_data[i+1]=chan_data[roi1+i];
    }
    roi1=1;
    roi2=npts_roi;
    /* Perform a few checks on the ROI selected */
    if (((roi2-roi1)<30) || ((roi2-roi1)>200)) {
      disp_move(21,0);
      disp_printf("Invalid number of points in ROI.\n");
        exit(4);
    }
    /* Free space used in ROI calculation */
    free_vector(chan_data, 1, CHANNELS);
    /* Now calculate terms for cubic as documented in PMB Vol 33#7 */
    /* pp847-857                                                   */
    /* e=PL f=QL g=[(-QR-2QL)/(ER-EL)+3(PR-PL)/(ER-EL)^2]          */
    /* h=[(QL+QR)/(ER-EL)^2+2(PL-PR)/(ER-EL)^3]                    */
    /* Use quadratic fitted above to find slopes                   */
    delta_x=x[npts_roi]-x[1];
    e=raw_data[1];
    f=ql;
    g=(-qr-2*ql)/delta_x+3*(raw_data[npts_roi]-raw_data[1])/delta_x/delta_x;
    h=(ql+qr)/delta_x/delta_x+2*(raw_data[1]-raw_data[npts_roi])/delta_x/delta_x/del
ta_x;
    /* Now set up parameters for fit */
    parms[1] = chan_data[(int)((alphal_energy-calib_int)/calib_slope)];
```

```
                                        /* Alpha2 amplitude            */
    parms[2] = alpha2_energy;           /* Alpha2 position             */
    parms[3] = detector_resoln*1.0E-3;  /* Alphal/2 width              */
    parms[4] = rel_peak_height;         /* (Alphal amp)/(Alpha2 amp)   */
    parms[5] = peak_e_diff;             /* (Alphal pos)-(Alpha2 pos)   */
    parms[6] = shelf_height;            /* Step height under a peak    */
    parms[7] = e-f*x[1]+g*x[1]*x[1]-h*x[1]*x[1]*x[1];
                                        /* Constant background         */
    parms[8] = f-2*g*x[1]+3*h*x[1]*x[1];    /* Linear component        */
    parms[9] = g-3*h*x[1];              /* Quadratic component         */
    parms[10] = h;                      /* Cubic component             */
    /* Declare arrays required by Marquadt routine */
    alpha = matrix(1, N_PARMS, 1, N_PARMS);
    covar = matrix(1, N_PARMS, 1, N_PARMS);
    sigma = vector(1, npts_roi);
    /* Declare space for array for initial guess  and background iteration */
    model_data = vector(1, npts_roi);
    x_back = vector(1, npts_roi);
    for (i=1; i<=N_BACK_FIT; i++) {
        x_back[i] = x[i];
        x_back[N_BACK_FIT+i] = x[npts_roi-N_BACK_FIT+i];
        model_data[i] = raw_data[i];
        model_data[N_BACK_FIT+i] = raw_data[npts_roi-N_BACK_FIT+i];
    }
    /* Set up standard deviation of all points assuming Poisson */
    for (i=1;i<=N_BACK_FIT*2;i++) {
        if (model_data[i]<1.0E-50) model_data[i]=1.0E-50;
        sigma[i]=sqrt(model_data[i]);
    }
    /* Iterate background using Marquadt */
    disp_move(23,0);
    disp_printf("Please wait - Iterating background.\n");
    /* Save peak amplitude and amplitude to zero for iteration */
    d1 = parms[1];
    parms[1] = 0.0;
    alamda=-1.0;
    mrqmin(x_back, model_data, sigma, 2*N_BACK_FIT, parms, N_PARMS, list_back, 4, co
var, alpha, &chisq, double_peak, &alamda);
    do {
        old_chisq=chisq;
        mrqmin(x_back, model_data, sigma, 2*N_BACK_FIT, parms, N_PARMS, list_back, 4
, covar, alpha, &chisq, double_peak, &alamda);
        parms_display(parms,covar,FALSE);
        delta_chisq=fabs((chisq-old_chisq)/chisq);
    } while (((delta_chisq>0.00001) || (delta_chisq<1.0E-50)) && alamda<1E15);
    alamda=0.0;
    mrqmin(x_back, model_data, sigma, 2*N_BACK_FIT, parms, N_PARMS, list_back, 4, co
var, alpha, &chisq, double_peak, &alamda);
    /* Restore original value of peak amplitude */
    parms[1] = d1;
    /* Subtract estimated background off peak amplitude */
    parms[1] -= parms[7]+parms[8]*alphal_energy+parms[9]*alphal_energy*alphal_energy
+parms[10]*alphal_energy*alphal_energy*alphal_energy;
    /* parms[1] should contain alpha 2 amplitude, was set to alpha 1 */
    parms[1] /= rel_peak_height;
    /* Set up array containing initial guess */
    for (i=1;i<=npts_roi;i++)
        double_peak(x[i],parms,&model_data[i],dummy,N_PARMS);
    /* Display data graphically */
    disp_move(23,0);
    disp_setattr(DISP_REVERSEVIDEO);
    disp_printf("Please press SPACE BAR to see display of data.");
    disp_setattr(DISP_NORMAL);
    do {
        temp_ch=getch();
    } while (temp_ch != ' ');
    lin_lin(x, model_data, raw_data, npts_roi, roi1, roi2);
    /* Reselect text display */
    text_display(argv[1], desc, detect, date, time, live_time, real_time, nofchans);
```

```
    /* Set up standard deviation of all points assuming Poisson */
    for (i=1;i<=npts_roi;i++) {
        if (raw_data[i]<1.0E-50) raw_data[i]=1.0E-50;
        sigma[i]=sqrt(raw_data[i]);
    }
    /* Maybe going round this loop a second time if fit is poor  */
    /* Therefore reset estimated peak height, peak positions and */
    /* relative peak heghts                                      */
    do {
        parms[1] = chan_data[(int)((alphal_energy-calib_int)/calib_slope)];
        parms[2] = alpha2_energy;
        parms[4] = rel_peak_height;
        parms[5] = peak_e_diff;
        parms[6] = shelf_height;
        parms[1] -= parms[7]+parms[8]*alphal_energy+parms[9]*alphal_energy*alphal_en
ergy+parms[10]*alphal_energy*alphal_energy*alphal_energy;
        parms[1] /= rel_peak_height;
        alamda=-1.0;
        mrqmin(x, raw_data, sigma, npts_roi, parms, N_PARMS, list_parms, iter_parms,
covar, alpha, &chisq, double_peak, &alamda);
        do {
            old_chisq=chisq;
            mrqmin(x, raw_data, sigma, npts_roi, parms, N_PARMS, list_parms, iter_pa
rms, covar, alpha, &chisq, double_peak, &alamda);
            parms_display(parms,covar,FALSE);
            delta_chisq=fabs((chisq-old_chisq)/chisq);
        } while (((delta_chisq>0.00001) || (delta_chisq<1.0E-50)) && alamda<1E15);
        alamda=0.0;
        mrqmin(x,raw_data,sigma,npts_roi,parms,N_PARMS,list_parms,iter_parms,covar,a
lpha,&chisq,double_peak,&alamda);
        parms_display(parms,covar,FALSE);
        if ((parms[1]<0.0) || (fabs(parms[2]-alpha2_energy)>0.5)) {
           iteration++;
         disp_setattr(DISP_REVERSEVIDEO);
           disp_move(13,42);
         disp_printf("(Iteration: %d)",iteration);
           disp_setattr(DISP_NORMAL);
        }
    } while (((parms[1]<0.0) || (fabs(parms[2]-alpha2_energy)>0.5)) && (iteration<=5
));
    /* Free temporary workspace used during Marquadt */
    free_matrix(alpha, 1, N_PARMS, 1, N_PARMS);
    free_vector(sigma, 1, npts_roi);
    /* Set up array containing fitted model */
    for (i=1;i<=npts_roi;i++)
        double_peak(x[i],parms,&model_data[i],dummy,N_PARMS);
    /* Display data graphically */
    disp_setattr(DISP_REVERSEVIDEO);
    disp_printf("\n\nPlease press SPACE BAR to see display of data.");
    disp_setattr(DISP_NORMAL);
    do {
        temp_ch=getch();
    } while (temp_ch != ' ');
    lin_lin(x, model_data, raw_data, npts_roi, roi1, roi2);
    text_display(argv[1], desc, detect, date, time, live_time, real_time, nofchans);
    parms_display(parms, covar, TRUE);
    /* Now calculate peak areas */
    mean=(int)((parms[2]-calib_int)/calib_slope-roi_offset);
    extent=(int)(2.0*parms[3]/calib_slope);
    peak_count(mean,extent,x,raw_data,parms,&area_Ka2,&back_Ka2);
    mean=(int)((parms[2]+parms[5]-calib_int)/calib_slope-roi_offset);
    extent=(int)(2.0*parms[3]/calib_slope);
    peak_count(mean,extent,x,raw_data,parms,&area_Ka1,&back_Ka1);
    area_Ka2P=SQRT_2PI*parms[3]*parms[1]/calib_slope;
    area_Ka1P=SQRT_2PI*parms[3]*parms[1]*parms[4]/calib_slope;
    delta_area2=sqrt(covar[1][1]/parms[1]/parms[1]+covar[3][3]/parms[3]/parms[3])*ar
ea_Ka2P;
    delta_area1=sqrt(covar[1][1]/parms[1]/parms[1]+covar[4][4]/parms[4]/parms[4]+cov
```

```
ar[3][3]/parms[3]/parms[3])*area_Kal2F;
    disp_move(20,0);
    if (area_Ka2>TWICE_SQRT2*sqrt(back_Ka2))
      disp_setattr(DISP_NORMAL | DISP_INTENSITY);
    else
      disp_setattr(DISP_NORMAL);
    disp_printf("K alpha 2: Area: %8.2f +/- %7.2f   Back.: %10.2f  \n",area_Ka2F,del
ta_area2,back_Ka2);
    if (area_Kal>TWICE_SQRT2*sqrt(back_Kal))
      disp_setattr(DISP_NORMAL | DISP_INTENSITY);
    else
      disp_setattr(DISP_NORMAL);
    disp_printf("K alpha 1: Area: %8.2f +/- %7.2f   Back.: %10.2f  \n\n",area_Kal2F,d
elta_area1,back_Kal);
    disp_setattr(DISP_REVERSEVIDEO);
    disp_printf("Please press SPACE BAR to exit analysis program.");
    disp_setattr(DISP_NORMAL);
    do {
        temp_ch=getch();
    } while (temp_ch != ' ');
    free_vector(x, 1, CHANNELS);
    free_vector(raw_data, 1, npts_roi);
    free_vector(model_data, 1, npts_roi);
    free_vector(x_back, 1, npts_roi);
    free_matrix(covar, 1, N_PARMS, 1, N_PARMS);
    disp_close();
    return 0;
}
```

A2 analycfg.c

```
/* Program to generate configuration file for analysis program       */
/* Original version 12/03/92                                         */
/* Modified 15/07/92: Read old CFG file from disk                    */

#define TRUE 1
#define FALSE 0

#define N_PARMS 10

/* Define defaults for parameters */
#define ALPHA2 66.990
#define DALPHA  1.814
#define RESLN   370
#define RELPK   1.69
#define SHELF   0.009

#include <stdio.h>      /* ANSI standard */
#include <stdlib.h>     /* ANSI standard */
#include <disp.h>       /* Zortech C display routines */
#include <conio.h>      /* Zortech C */

/*Service routine for read_config - reads an item from file */
/*========================================================= */
int read_item(double *p, FILE *fp, int parm_number)
{
    int n_items;

    n_items = fscanf(fp, "%lf", p);
    if (n_items != 1) {
        fprintf(stderr, "Error in reading parameter %d from configuration file\n", p
arm_number);
    } else
        return FALSE;
}

/*Routine to extract configuration from disk */
/*=========================================*/
```

```
void read_config(double *p1, double *p2, double *p3, double *p4, double *p5, char li
st[])
{
    FILE *fp;
    int i, n_items, iter, temp;

    for (i=1; i<=N_PARMS; i++)
        list[i] = 'N';
    if ((fp = fopen("ANALYSE.CFG","r")) == NULL) {
        *p1 = ALPHA2;
        *p2 = DALPHA;
        *p3 = RESLN;
        *p4 = RELPK;
        *p5 = SHELP;
    } else {
        if (read_item(p1, fp, 1)) *p1 = ALPHA2;
        if (read_item(p2, fp, 2)) *p2 = DALPHA;
        if (read_item(p3, fp, 3)) *p3 = RESLN;
        if (read_item(p4, fp, 4)) *p4 = RELPK;
        if (read_item(p5, fp, 5)) *p5 = SHELP;
        n_items = fscanf(fp,"%d", &iter);
        if (n_items != 1) {
            fprintf(stderr, "Error in reading number of parameters to iterate from c
onfiguration file\n");
            return;
        }
        for (i=1; i<=iter; i++) {
            n_items = fscanf(fp, "%d", &temp);
            if (n_items != 1) {
                fprintf(stderr, "Error in reading list item %d from configuration fi
le\n", i);
                return;
            } else {
                if (temp <= N_PARMS) list[temp] = 'Y';
            }
        }
        fclose(fp);
    }
}

void parm_iterate(char *format, double value, char old, int parm, int list[], int *t
op_set, int total_set)
{
     char response;

     disp_printf(format, value, old);
     do {
         response = (char)(getch() &0x5f);
     } while ((response != 'Y') && (response != 'N'));
     disp_putc(response);
     disp_putc('\n');
     if (response == 'Y') {
         (*top_set)++;
         list[*top_set] = parm;
     } else {
         list[N_PARMS-(total_set-*top_set)] = parm;
     }
}

void write_file(double p1, double p2, double p3, double p4, double p5, int iter, int
list[])
{
    FILE *fp;
    int i;

    if ((fp = fopen("ANALYSE.CFG","w")) == NULL) {
        disp_printf("Failed to open ANALYSE.CFG\n");
        return;
    }
```

```
    fprintf(fp,"%lf\n",p1);
    fprintf(fp,"%lf\n",p2);
    fprintf(fp,"%lf\n",p3);
    fprintf(fp,"%lf\n",p4);
    fprintf(fp,"%lf\n",p5);
    fprintf(fp,"%d\n", iter);
    for (i=1; i<=N_PARMS; i++)
        fprintf(fp, "%d\n", list[i]);
    fclose(fp);
    disp_printf("ANALYSE.CFG written to disk.\n");
}

int main()
{
    double alpha2_energy, peak_e_diff, rel_peak_height;
    double detector_resoln, shelf_height;
    char default_iter[N_PARMS+1], response;
    static int list_parms[N_PARMS+1] = {0, 1, 0, 0, 0, 0, 0, 0, 0, 0, 0};
    int iter_parms = 1;

    disp_setmode(3);
    disp_open();
    disp_usebios();
    disp_move(0,0);
    disp_eeop();
    disp_setattr(DISP_NORMAL | DISP_INTENSITY);
    disp_printf("Analysis program configuration\n");
    disp_printf("==============================\n");
    disp_setattr(DISP_NORMAL);
    read_config(&alpha2_energy, &peak_e_diff, &detector_resoln, &rel_peak_height, &s
helf_height, default_iter);
    disp_printf("Please enter the energy of the K alpha 2 peak [%.3lfkeV]:  ", alpha
2_energy);
    scanf("%lf", &alpha2_energy);
    disp_printf("\nPlease enter the energy of the K alpha 1 peak [%.3lfkeV]:  ", pea
k_e_diff+alpha2_energy);
    scanf("%lf", &peak_e_diff);
    peak_e_diff -= alpha2_energy;
    disp_printf("\nPlease enter the relative peak heights (Kal/Ka2) [%.2lf]:  ", rel
_peak_height);
    scanf("%lf", &rel_peak_height);
    disp_printf("\nPlease enter the detector resolution at %.1lfkeV [%.0lfeV]:  ", a
lpha2_energy+peak_e_diff/2.0, detector_resoln);
    scanf("%lf", &detector_resoln);
    disp_printf("\nPlease enter the shelf height under a peak at %.1lfkeV [%.2lf%%])
:  ", alpha2_energy+peak_e_diff/2.0, shelf_height*100);
    scanf("%lf", &shelf_height);
    shelf_height /= 100;
    disp_move(2,0);
    disp_eeop();
    disp_move(2,0);
    disp_setattr(DISP_REVERSEVIDEO);
    disp_printf("Do you wish to iterate the following parameters?\n");
    disp_setattr(DISP_NORMAL);
    parm_iterate("K alpha 2 energy  = %.2lfkeV? [%c]  ", alpha2_energy, default_iter
[2], 2, list_parms, &iter_parms, 1);
    parm_iterate("Kal - Ka2 energy  = %.2lfkeV? [%c]  ", peak_e_diff, default_iter[5
], 5, list_parms, &iter_parms, 2);
    parm_iterate("Detector resoln   = %.2lfeV? [%c]  ", detector_resoln, default_ite
r[3], 3, list_parms, &iter_parms, 3);
    parm_iterate("Relative peak ht  = %.2lf? [%c]  ", rel_peak_height, default_iter[
4], 4, list_parms, &iter_parms, 4);
    parm_iterate("Peak shelf height = %.2lf%%? [%c]  ", shelf_height*100.0, default_
iter[6], 6, list_parms, &iter_parms, 5);
    /* Background parameters */
    list_parms[iter_parms+1] = 7;
    list_parms[iter_parms+2] = 8;
    list_parms[iter_parms+3] = 9;
    list_parms[iter_parms+4] = 10;
```

```
    disp_printf("Background? [%c]  ", default_iter[7]);
    do {
        response = (char)(getch() &0x5f);
    } while ((response != 'Y') && (response != 'N'));
    disp_putc(response);
    disp_putc('\n');
    if (response == 'Y')
        iter_parms -= 4;
    write_file(alpha2_energy, peak_e_diff, detector_resoln, rel_peak_height, shelf_h
eight, iter_parms, list_parms);
    disp_close();
}
```

Appendix B

Monte Carlo Model

```
/* Monte Carlo Photon Tracking Model                                    */
/* Purpose: To find relative gold sensitivities in a scatter medium */
/* John Shakeshaft                                                      */
/* Sensitivity over whole kidney volume added 24/10/91                  */
/* Sensitivity uncertainties added 30/10/91                             */

/**********************************************************************/
/* This program must be linked with a double precision version of     */
/* a library of the routines from Numerical Recipes in C - The art    */
/* of scientific computing by Press WH et al (CUP)                    */
/*                                                                    */
/* In the double precision version  float    =>    double            */
/*                                  double   =>    long double       */
/**********************************************************************/


#include <stdio.h>  /* ANSI Standard */
#include <math.h>   /* ANSI Standard */
#include "nr.h"     /* Numerical Recipes Library */
#include "nrutil.h" /* Numerical Recipes Library */

/* Increase stack size in Zortech C  */
unsigned _stack = 32768;

#define PI 3.14159265358979323846264338327 9

#define TRUE 1
#define FALSE 0

/* Elementary charge over Plancks constant * speed of light *1.0e3  */
#define E_HC 8.065753E+08

/* Define Maximum and Minimum energies of interest                   */
/* Maximum energy must be maximum energy of source                   */
/* Minimum energy is minimum energy of interest                      */
#define MIN_ENERGY 65.0
#define MAX_ENERGY 105.0

/* Define constants for interpolation of scattering cross sections  */
/* These have been found by log-log linear regression of sigma      */
/* against E: ln(sigma) = A + B ln E                                */
/* Values are:      Water                    Soft tissue           */
/* Coh_A, Coh_B      5.692,  -1.876          5.659, -1.887         */
/* Incoh_A, Incoh_B  1.315,  -0.1845         1.440, -0.2124        */
/* Photo_A, Photo_B 11.549,  -3.295         10.746, -3.132         */
/* These are in barns per atom                                      */
/* RAM (average)     5.96                    6.05                  */
/* Density (kg m-3)  1000                    1000?                 */
#define COH_A 5.692
#define COH_B (-1.876)
#define INCOH_A 1.315
#define INCOH_B (-0.1845)
#define PHOTO_A 11.549
#define PHOTO_B (-3.295)
#define RAM 5.96
#define DENSITY 1000.0

/* Now define similar constants for gold. There are two values: one */
/* for below the K absorption edge (LOW), and one for above (HIGH)  */
/* Also define the value of the K absorption edge                   */
#define AU_COH_A 11.55
#define AU_COH_B (-1.620)
```

```
#define AU_INCOH_LOW_A 2.400
#define AU_INCOH_LOW_B 0.2624
#define AU_INCOH_HIGH_A 4.1577
#define AU_INCOH_HIGH_B (-0.1429)
#define AU_PHOTO_LOW_A 17.992
#define AU_PHOTO_LOW_B (-2.9262)
#define AU_PHOTO_HIGH_A 20.101
#define AU_PHOTO_HIGH_B (-2.9793)
#define AU_K_ABS 80.723
#define AU_K_ALPHA 68.804
#define AU_RAM 197.0
#define AU_DENSITY 19320.0

/* Define constants for calculating elastic scattering probabilities*/
/* Added 1/8/91                                                     */
/* Values are for use in equation                                   */
/* x2 = exp(a1 +a2x +a3x2 +a4x3 + ....                              */
/* Values are                                                       */
/*             Gold          Tissue          Water                  */
/*   a1      -7.0330e+0    -8.3705e+0    -8.3890e+0                 */
/*   a2      +1.6869e-2    +3.1323e+1    +2.8655e+1                 */
/*   a3      -1.5008e-5    -6.1247e+1    -5.1506e+1                 */
/*   a4      +5.8928e-9    +5.0721e+1    +3.9128e+1                 */
/*   a5      -1.0108e-12   -1.7804e+1    -1.2577e+1                 */
/*   a6      +6.3167e-17   +2.2099e+0    +1.4284e+0                 */
/* abs.max   +7.061e+3     3.431         3.753                      */
/* 120kVmax) +4.837e+1     1.535e-1      1.624e-1                   */
#define EL_M_A1 (-8.3890e+0)
#define EL_M_A2 (2.8655e+1)
#define EL_M_A3 (-5.1506e+1)
#define EL_M_A4 3.9128e+1
#define EL_M_A5 (-1.2577e+1)
#define EL_M_A6 1.4284e+0
#define EL_M_MAX 1.624e-1
#define EL_A_A1 (-7.0330e+0)
#define EL_A_A2 1.6869e-2
#define EL_A_A3 (-1.5008e-5)
#define EL_A_A4 5.8928e-9
#define EL_A_A5 (-1.0108e-12)
#define EL_A_A6 6.3167e-17
#define EL_A_MAX 48.37


/* Now define gold concentration by weight (%)                      */
/* 1000ug g^-1 = 0.1%                                               */
#define AU_CN 0.1

/* Define source collimator parameters                              */
/* All distances in metres, All angles in radians                   */
#define SOURCE_COLLIMATE_ANGLE (7.0/180.0*PI) /* Originally (12.0/..*/
#define SSD 0.152 /* Originally 0.045 - Now 0.2-Lat depth */

/* Define other geometrical parameters                              */
#define X_SKIN 0.053 /* Originally 0.055 - Now 0.025+Post depth */

/* Define detector collimator parameter                             */
#define DETECT_X (X_SKIN+0.035)
#define DETECT_Y 0.0
#define DETECT_Z 0.225 /* Originally (SSD+0.075) */
#define DETECT_RAD 0.016
#define DETECT_COLLIMATE_ANGLE (6.0/180.0*PI)
/* Define size of area of sensitivity interest (in size G_UNIT)     */
#define G_UNIT 0.01
#define X_MIN (-7)
#define X_SIZE 15
#define Y_MIN 0
#define Y_SIZE 1
#define Z_MIN 15 /* Originally 4 */
#define Z_SIZE 13
```

```
/* Number of photons to be considered                                  */
#define N_PHOTONS 1000000

/* Declare type for current coords of photon                           */
/* NB: Source is at x = y = z = 0                                      */
typedef struct photon_coord { double x; double y; double z; } photon_coord;
/* Declare type for direction co-sine storage                          */
typedef struct dir_cosine { double u; double v; double w; } dir_cosine;

/* Variable used by ran3 routine                                       */
static int idum = -1;

/* Variable used to store limiting cosine for photon direction         */
static double min_source_cos;
/* Variables used to store limiting tangent for detector acceptence    */
static double max_detect_tan, tan_penumbra_ang;

/*********************************************************************/
/* This routine returns the initial photon energy                      */
/* and is source specific                                              */
/*********************************************************************/

double get_photon_energy(void)
{
      if (ran3(&idum)<0.60)
          return (97.0);
      else
          return (103.0);
}


double get_ang(void)
{
      /* Returns a random angle between -PI and  PI                    */
      return ((2.0*ran3(&idum)-1.0)*PI);
}

void get_isotropic_direction(double *cos_gamma, double *phi,
                             double min_cos_gamma)
{
      /* On entry: min_cos_gamma contains the minimum value of         */
      /* cos(gamma).This allows conical collimation to be              */
      /* implemented. It should be set to -1.0 for a truly isotropic*/
      /* distribution                                                  */

      /* Returns cos(gamma) and phi                                    */
      /* Phi is angle from x axis in xy plane (longtitude)             */
      /* Gamma is angle from z axis                                    */

      /* See Cashwell & Everett Chapter 2, Page 19                     */
      *cos_gamma = 1.0 - (1.0-min_cos_gamma)*ran3(&idum);
      *phi = get_ang();
}

void get_compton(double energy_in, double *energy_out, double *cos_ang)
{
      /* On entry: energy_in contains the energy of the photon being*/
      /*           scattered                                           */
      /* On exit: energy_out contains energy of scattered photon     */
      /*          cos_ang contains the cosine of the scattering      */
      /*          angle                                              */

      /* The following routine from Cashwell and Everett Chapter 6  */
      /* can be used. But only gives a fairly approximate distrib.  */
      /*double r, s, energy;                                         */
      /*                                                             */
      /* r = ran3(&idum);                                           */
      /*energy = energy_in/510.83;    Create dimensionless parameter*/
```

```
      /* s = energy/(1.0+0.5625*energy);                              */
      /* *energy_out = energy_in/(1.0+s*r+(2.0*energy-s)*r*r*r);      */
      /* *cos_ang = 1.0+1.0/energy-510.83/(*energy_out);              */

      /* Therefore use von Neumann technique as described in          */
      /* Cashwell and Everett Chapter 1 page 9.                       */
      /* a is used to store cos_ang                                   */
      /* energy is a dimensionless parameter - energy_in/mc2          */
      /* e_1_a = energy(1 - a)                                        */
      /* e_1_a_1 = 1 + energy(1-a)                                    */
      /* a2_1 = 1 + a2                                                */
      double a, energy, y, e_1_a, e_1_a_1, a2_1;

      energy  = energy_in/510.83; /* Dimensionless parameter          */
      do {
          /* Select a random cos, can be between -1 and +1           */
          a = -1.0 + 2.0*ran3(&idum);
          /* Calculate the values used for calculating the X-section*/
          a2_1 = a*a + 1.0;
          e_1_a = energy*(1.0 - a);
          e_1_a_1 = 1.0 + e_1_a;
          /* Calculate the cross section                              */
          y = a2_1/e_1_a_1/e_1_a_1*(1.0 + e_1_a*e_1_a/a2_1/e_1_a_1);
      } while (ran3(&idum)*2.0>y);      /* Maxium value of y is 2.0 */
      *cos_ang = a;
      *energy_out = energy_in/e_1_a_1;
}

double get_x2(double energy, double perc_au)
{
      /* Returns a value of x2 for elastic scattering                 */
      /* On entry energy contains energy of photon in interaction     */
      /* Added 1/8/91                                                 */

      /* declare temporary variables                                  */
      /* x2 holds value of x^2 to return                              */
      /* x2_max contains the maximum allowed value of x^2 at the      */
      /* energy of the photon                                         */
      /* r,r2,r4 are used to store the random number etc              */
      double x2, x2_max, r, r2, r4;

      /* Calculate the maximum value of x2 allowed                    */
      /* NB: 1e-20 because x is in Angstroms                          */
      x2_max = energy * energy * E_HC * E_HC * 1.0e-20;
      /* Is it gold or medium?                                        */
      if (ran3(&idum)<perc_au) {
          /* Routine for elastic interaction with gold                */
          do {
              r = ran3(&idum)*EL_A_MAX;
              r2 = r * r;
              r4 = r2 * r2;
              x2 = exp(EL_A_A1 + EL_A_A2*r + EL_A_A3*r2 + EL_A_A4*r2*r + EL_A_A5*r4
+ EL_A_A6*r4*r);
          } while (x2>x2_max);
      } else {
          /* Routine for elastic interaction with medium              */
          do {
              r = ran3(&idum)*EL_M_MAX;
              r2 = r * r;
              r4 = r2 * r2;
              x2 = exp(EL_M_A1 + EL_M_A2*r + EL_M_A3*r2 + EL_M_A4*r2*r + EL_M_A5*r4
+ EL_M_A6*r4*r);
          } while (x2>x2_max);
      }
      return x2;
}

double get_elastic(double energy, double perc_au)
{
```

```
      /* Returns angle for Elastic scattering weighted              */
      /* appropiately for angle dependence                          */
      /* See Persliden 1983                                         */
      /* On entry:   energy contains energy of photon being         */
      /*             scattered                                      */
      /* Returns:    cos of scattering angle                        */
      /* Completely rewritten 1/8/91                                */
      /* Declare variables                                          */
      /* Variable to hold x squared (x = sin (theta/2)/wavelength)  */
      /* Wavelength is in Angstroms                                 */
      double x2;
      /* Variable to hold sin2 of (angle/2) and cos angle           */
      double sin2_ang_2, cos_ang;

      do {
          x2 = get_x2(energy, perc_au);
          /* 1.0e-20 factor because x is in angstroms               */
          sin2_ang_2 = x2/E_HC/E_HC/1.0e-20/energy/energy;
          cos_ang = 1.0-2*sin2_ang_2;
      } while (ran3(&idum)>((1+cos_ang*cos_ang)/2.0));
      return cos_ang;
}

double get_pathlength(double energy, double mean_path[])
{
      /* Gets random path length of a photon                        */
      /* On entry: energy contains energy of photon                 */
      /*           mean_path contains table of mean free paths      */
      /*           (1/abs coeff) as a function of energy            */
      /* Returns: path length of photon in scattering medium        */
      /* See Cashwell and Everett Chapter 3, pages 28-29            */
      return (-mean_path[(int)(energy)]*log(ran3(&idum)));
}

double get_dist_sq(photon_coord p1, photon_coord p2,
                   double *tan_edge_ang, double *weight)
{
      /* Returns the square of the distance between two postions    */
      /* p1 and p2. For weight and tan_edge_ang to be meaningful p2 */
      /* must be the detector position. Then the tangent of the     */
      /* the angle between the edge of the detector and p1 is       */
      /* returned in tan_edge_ang. And the proportion of the detect */
      /* that can be seen at p1 is returned in weight               */
      double dx, dy, dz, dy2, dz2;
      double perp_dist;
      double weight_temp, weight_ang;

      dx = fabs(p2.x - p1.x);
      dy = p2.y - p1.y;
      dz = p2.z - p1.z;
      dy2 = dy * dy;
      dz2 = dz * dz;
      /* Find distance of p1 from axis of detect in plane of detect */
      perp_dist = sqrt(dy2 + dz2);
      *tan_edge_ang = (perp_dist - DETECT_RAD)/dx;
      *weight = 1.0;
      if (perp_dist>=tan_penumbra_ang*dx-DETECT_RAD)
          *weight = 0.0;
      else
          if (*tan_edge_ang>max_detect_tan) {
             *weight -= (*tan_edge_ang-max_detect_tan)/(tan_penumbra_ang-max_detect_
tan-2.0*DETECT_RAD/dx);
             /* This is proportion of diameter that can be seen     */
             /* change to proportion of area                        */
             weight_temp = 2.0 * *weight - 1.0;
             weight_ang = asin(weight_temp);
             *weight = (weight_ang + sin(weight_temp)*cos(weight_ang))/PI +0.5;
          } else if (*tan_edge_ang<0.0) *tan_edge_ang=0.0;
      return ((dx*dx) + (dy2) + (dz2));
```

```
}

double get_cross2(int energy, double perc_au, double a_medium,
                  double b_medium, double a_au, double b_au)
{
      /* Does interpolation on log-log coefficients to find cross   */
      /* cross section                                              */
      /* On entry: perc_au is number percentage of gold atoms       */
      /*           a_medium, b_medium  Medium lin regress coeffs    */
      /*           a_au, b_au          Gold lin regress coeffs      */
      /*           energy is energy of photon                       */
      /* Regression done in barns per atom. Convert to m^-1 by      */
      /* * 0.06023 / ram * density                                  */
      double gold, medium, engy;

      engy = (double)(energy);
      gold = exp(a_au + b_au*log(engy)) * perc_au / AU_RAM * AU_DENSITY;
      medium = exp(a_medium + b_medium*log(engy)) * (1.0-perc_au) /  RAM * DENSITY;
      return (0.06023*(gold+medium));
}

void get_cross(double *s_elastic, double *s_compton, double *s_photoel,
               double *s_pe_gold, double *mean_path, int min_energy,
               int max_energy, double perc_au)
{
      /* Routine to calculate and store cross-sections for          */
      /* different events for all relevant energies                 */

      /* Declare counter variable                                   */
      int i;

      for (i=min_energy; i<=max_energy; i++) {
          s_elastic[i] = get_cross2(i, perc_au, COH_A, COH_B, AU_COH_A, AU_COH_B);
          if ((double)(i)<AU_K_ABS) {
              s_compton[i] = get_cross2(i, perc_au, INCOH_A, INCOH_B, AU_INCOH_LOW_A
, AU_INCOH_LOW_B);
              s_photoel[i] = get_cross2(i, perc_au, PHOTO_A, PHOTO_B, AU_PHOTO_LOW_A
, AU_PHOTO_LOW_B);
              s_pe_gold[i] = 0.06023 * exp(AU_PHOTO_LOW_A + AU_PHOTO_LOW_B*log((doub
le)(i))) * perc_au / AU_RAM * AU_DENSITY;
          } else {
              s_compton[i] = get_cross2(i, perc_au, INCOH_A, INCOH_B, AU_INCOH_HIGH_
A, AU_INCOH_HIGH_B);
              s_photoel[i] = get_cross2(i, perc_au, PHOTO_A, PHOTO_B, AU_PHOTO_HIGH_
A, AU_PHOTO_HIGH_B);
              s_pe_gold[i] = 0.06023 * exp(AU_PHOTO_HIGH_A + AU_PHOTO_HIGH_B*log((do
uble)(i))) * perc_au / AU_RAM * AU_DENSITY;
          }
          mean_path[i] = 1.0/(s_compton[i] + s_elastic[i] + s_photoel[i]);
      }
}

void first_photon(photon_coord *xyz, dir_cosine *uvw, double *energy,
                  double *mean_path)
{
      /* Routine to get initial interaction site                    */
      /* On entry: mean_path, is array of mean paths with energy    */
      /* On exit:  uvw returns initial direction cosines            */
      /*           xyz returns position of first interaction        */
      /*           energy returns the energy of the photon before   */
      /*           the interaction                                  */
      /* Declare variables for distance of travel                   */
      double total_travel, medium_travel;
      /* Declare variables for direction cos calculation            */
      /* See Cashwell and Everett Chapter 2, page 20                */
      double phi, cos_phi, sin_phi, cos_gamma, sin_gamma;
      /* First need to get a direction                              */
      /* Some angles not allowed by collimator                      */
      get_isotropic_direction(&cos_gamma, &phi, min_source_cos);
```

```
        cos_phi = cos(phi);
        sin_phi = sin(phi);
        sin_gamma = sqrt( 1.0 - cos_gamma * cos_gamma);
        /* Get energy of the photon                                    */
        *energy = get_photon_energy();
        /* Get the distance travelled in the medium                    */
        medium_travel = get_pathlength(*energy, mean_path);
        /* Will travel some distance in air before an interaction      */
        total_travel = SSD/cos_gamma + medium_travel;
        xyz->x = xyz->y = total_travel * sin_gamma;
        xyz->x *= cos_phi;
        xyz->y *= sin_phi;
        xyz->z = total_travel * cos_gamma;
        uvw->u = sin_gamma * cos_phi;
        uvw->v = sin_gamma * sin_phi;
        uvw->w = cos_gamma;
}

void get_new_pos(photon_coord *xyz, dir_cosine *uvw, double cos_psi,
                 double energy, double *mean_path)
{
        /* See Cashwell and Everett Chapter 7, page 106                */
        /* On entry: xyz and uvw are current position and direction    */
        /*           cos_psi is cosine of the scattering angle         */
        /*           energy is the energy of the photon after          */
        /*           scatter mean_path is the table of mean path       */
        /*           lengths                                           */
        /* On exit:  xyz and uvw return the new position and           */
        /*           direction respectively                            */
        /* Temporary variables used for calculating new direction      */
        /* cosines                                                     */
        double sin_w, bc, bd, bcw;
        /* Path length of photon after interaction                     */
        double path_length;
        /* Scatter angles                                              */
        double sin_psi, phi, cos_phi, sin_phi;
        /* Temporary variable for new direction                        */
        dir_cosine new_uvw;

        path_length = get_pathlength(energy, mean_path);
        sin_psi = sqrt(1.0 - cos_psi*cos_psi);
        phi = get_ang();
        cos_phi = cos(phi);
        sin_phi = sin(phi);
        bc = sin_psi * cos_phi;
        bd = sin_psi * sin_phi;
        if (fabs(uvw->w)<0.99) {
            sin_w = sqrt(1.0-uvw->w*uvw->w);
            bcw = bc * uvw->w;
            new_uvw.u = ((bcw*uvw->u - bd*uvw->v)/sin_w) + cos_psi*uvw->u;
            new_uvw.v = ((bcw*uvw->v + bd*uvw->u)/sin_w) + cos_psi*uvw->v;
            new_uvw.w = (-bc * sin_w) + (cos_psi * uvw->w);
        } else {
            new_uvw.u = bc;
            new_uvw.v = bd;
            new_uvw.w = cos_psi * uvw->w;
        }
        *uvw = new_uvw;
        xyz->x += uvw->u * path_length;
        xyz->y += uvw->v * path_length;
        xyz->z += uvw->w * path_length;
}


int main(int argc, char *argv[])
{
        /* Tables of values of absorption coefficient, mean free       */
        /* paths etc                                                   */
        double *mean_path, *s_photoel, *s_elastic, *s_compton, *s_pe_gold;
```

```
      /* Minimum and maximum energy as integer constants            */
      int min_energy=(int) MIN_ENERGY, max_energy=(int) MAX_ENERGY;
      /* Number percentage of gold atoms                            */
      double perc_au = (AU_CN/AU_RAM)/(AU_CN/AU_RAM+(100.0-AU_CN)/RAM);
      /* Direction of travel                                        */
      dir_cosine direction, old_direction;
      /* Cosine of angle through which the photon was scattered     */
      double cos_psi;
      /* Photon energy                                              */
      double energy;
      int int_energy;
      /* Photon and detector positions                              */
      photon_coord photon_xyz, old_xyz, delta_xyz, detect_xyz;
      /* Random number for interaction type                         */
      double interaction;
      /* Flag to check if photon has died e.g. By photoelectric     */
      int photon_dead = FALSE;
      /* Declare variable for calculating relative importance of    */
      /* photoelectric interaction                                  */
      double pe;
      /* Variables used when calculating the distance from the      */
      /* detector                                                   */
      double detect_dist_sq, detect_dist;
      /* Temporary variables used for checking if photon entered    */
      /* detector                                                   */
      double temp_y, temp_z, scale;
      /* Counter for number of photons                              */
      int photon_count;
      /* Counter for number of used photons                         */
      int photon_sens_count = 0, photon_spect_count = 0;
      /* Sum of sensitivity in kidney                               */
      double kid_sens_sum = 0.0;
      /* Tangent of angle between detector edge and interaction     */
      double tan_edge_ang;
      /* Proportion of the detector that can be seen by the photon  */
      double weight;
      /* Arrays for storing results                                 */
      double sens[X_SIZE][Y_SIZE][Z_SIZE];
      int uncer[X_SIZE][Y_SIZE][Z_SIZE];
      int *cspectrum;
      /* Counter variables                                          */
      int i,j,k;
      /* File pointer, used to save results                         */
      FILE *fp;

      /************************************************************/
      /*  Initialisation                                          */
      /************************************************************/
      /* Make space for table storage                               */
      mean_path = vector(min_energy, max_energy);
      s_photoel = vector(min_energy, max_energy);
      s_elastic = vector(min_energy, max_energy);
      s_compton = vector(min_energy, max_energy);
      s_pe_gold = vector(min_energy, max_energy);
      cspectrum = ivector(min_energy, max_energy);
      /* Now calculate the various values and store in tables       */
      get_cross(s_elastic, s_compton, s_photoel, s_pe_gold, mean_path, min_energy, m
ax_energy, perc_au);
      /* Initialise variable for source collimation                 */
      min_source_cos = cos(SOURCE_COLLIMATE_ANGLE);
      /* Initialise variables for detector collimation              */
      max_detect_tan = tan(DETECT_COLLIMATE_ANGLE);
      tan_penumbra_ang = 2.0*DETECT_RAD/(DETECT_X-X_SKIN) + max_detect_tan;
      /* Initialise detector position                               */
      detect_xyz.x = -DETECT_X;
      detect_xyz.y = DETECT_Y;
      detect_xyz.z = DETECT_Z;
      /* Zero sensitivity table                                     */
      for (i=0; i<X_SIZE; i++)
```

```
        for(j=0; j<Y_SIZE; j++)
            for(k=0; k<Z_SIZE; k++)
                sens[i][j][k] = 0.0, uncer[i][j][k] = 0;
    for (i=min_energy; i<max_energy; i++)
        cspectrum[i] = 0;
    /*************************************************************/
    /* Main modelling loop                                       */
    /*************************************************************/
    /* Loop for as many photons as required                      */
    for (photon_count=1; photon_count<=N_PHOTONS; photon_count++) {
        /* Now model the life history of a photon                */
        first_photon(&photon_xyz, &direction, &energy, mean_path);
        photon_dead = FALSE;
        /* Loop until photon is no longer of any interest        */
        while (!photon_dead) {
            /* Get interaction type and process                  */
            interaction = ran3(&idum);
            int_energy = (int)(energy);
            /* Save direction and position of photon             */
            old_direction = direction;
            old_xyz = photon_xyz;
            if (interaction<s_photoel[int_energy]*mean_path[int_energy]) {
                /* Photoelectric transition                      */
                photon_dead=TRUE;
                pe = 0.0;
                /* Assume photoelectric transition was with gold */
                /* and then weight accordingly                   */
                /* Firstly may have been medium that interaction */
                /* was with                                      */
                if (energy>=AU_K_ABS)
                    pe = s_pe_gold[int_energy]/s_photoel[int_energy]*1000.0;
                /* Amount of signal entering the detector will   */
                /* be reduced by attenuation, and the solid      */
                /* angle subtended by the detector. Also by      */
                /* detector collimation. Allow for this          */
                /*                                               */
                /* Firstly attenuation:                          */
                /* Calculate distance of centre of detector      */
                detect_dist_sq = get_dist_sq(photon_xyz, detect_xyz, &tan_edge_ang
, &weight);
                /* Allow for proportion of the detector that can */
                /* be seen                                       */
                pe *= weight;
                /* Check to see if photon accepted by detector   */
                /* collimator, if not ignore this interaction    */
                if ((weight>0.1) && (pe > 0.0)) {
                    detect_dist = sqrt(detect_dist_sq);
                    pe *= exp((-detect_dist)*(1.0 - (DETECT_X-X_SKIN)/(photon_xyz.
x-detect_xyz.x ))/mean_path[(int)(AU_K_ALPHA)]);
                    /* Secondly solid angle subtended            */
                    /* This falls as                             */
                    /*  (1 - 1/sqrt(1+(DETECT_RAD/detect_dist)^2))*/
                    /* Allow for off axis point by multiplying pe */
                    /* by the cosine of the angle off the        */
                    /* detector axis                             */
                    pe *= (1.0 - 1.0/sqrt(1.0 + DETECT_RAD*DETECT_RAD/detect_dist_
sq)) * (photon_xyz.x-detect_xyz.x)/detect_dist;
                    i = (int)(photon_xyz.x/G_UNIT-0.5-(double)(X_MIN));
                    j = (int)(photon_xyz.y/G_UNIT-0.5-(double)(Y_MIN));
                    k = (int)(photon_xyz.z/G_UNIT-0.5-(double)(Z_MIN));
                if ((i>=0) && (i<X_SIZE) && (j>=0) && (j<Y_SIZE) && (k>=0) && (k<Z_
SIZE)) {
                        photon_sens_count++;
                        sens[i][j][k] += pe;
                        uncer[i][j][k]++;
                    }
                    /* Now sum total sensitivity in kidney */
                    if ((photon_xyz.z>DETECT_Z-0.025) && (photon_xyz.z<DETECT_Z+0.
025) && (photon_xyz.y>DETECT_Y-0.05) && (photon_xyz.y<DETECT_Y+0.05) && (photon_xyz.
```

```
x>-0.025) && (photon_xyz.x<0.025)) kid_sens_sum += pe;
                }
            } else {
                if (interaction<(s_photoel[int_energy]+s_elastic[int_energy])*mean
_path[int_energy]) {
                    /* Elastic interaction                          */
                    /**********************************************/
                    cos_psi = get_elastic(energy, perc_au);
                } else {
                    /* Compton interaction                          */
                    /**********************************************/
                    get_compton(energy, &energy, &cos_psi);
                }
            }
            /* If photon still alive get next coords               */
            if (!photon_dead)
                get_new_pos(&photon_xyz, &direction, cos_psi, energy, mean_path);
            /* Check it still has sufficient energy to be of       */
            /* interest                                            */
            if (energy<=MIN_ENERGY)
                photon_dead = TRUE;
            /* Check that this is still within the medium on       */
            /* source side                                         */
            if (photon_xyz.z<SSD)
                photon_dead = TRUE;
            /* Check to see if photon has left the medium on the   */
            /* detector side, and if so whether it entered the     */
            /* detector                                            */
            if (photon_xyz.x<(-X_SKIN) && (!photon_dead)) {
                photon_dead = TRUE;
                /* Calculate the square of the distance from the   */
                /* centre of the detector within which the         */
                /* photon passes                                   */
                delta_xyz.x = photon_xyz.x - old_xyz.x;
                delta_xyz.y = photon_xyz.y - old_xyz.y;
                delta_xyz.z = photon_xyz.z - old_xyz.z;
                scale = (detect_xyz.x - old_xyz.x)/delta_xyz.x;
                temp_y = detect_xyz.y - (old_xyz.y + scale * delta_xyz.y);
                temp_z = detect_xyz.z - (old_xyz.z + scale * delta_xyz.z);
                /* and store it                                    */
                detect_dist_sq = temp_y*temp_y+temp_z*temp_z;
                /* Get angle bewteen interaction point and the     */
                /* edge of the detector                            */
                get_dist_sq(old_xyz, detect_xyz, &tan_edge_ang, &weight);
                /* If photon could have passed through detector    */
                /* and collimation OK then add to spectrum         */
                if ((tan_edge_ang<max_detect_tan) && (detect_dist_sq<DETECT_RAD*DE
TECT_RAD)) {
                    cspectrum[(int)(energy)]++;
                    photon_spect_count++;
                }
            }
        }
    }
    fp = fopen("spectrum","w");
    for (i=min_energy; i<max_energy; i++)
        fprintf(fp,"%d, %d\n",i, cspectrum[i]);
    fclose(fp);
    fp = fopen("sens","w");
    fprintf(fp,"Predicted sensitivities:\n");
    for (i=0; i<Z_SIZE; i++) {
        for (j=0; j<X_SIZE; j++)
            fprintf(fp, "%8.2lf, ",sens[j][-(Y_MIN)][i]);
        fputc('\n', fp);
    }
    fprintf(fp,"\nUncertainties due to counting statistics:\n");
    for (i=0; i<Z_SIZE; i++) {
        for (j=0; j<X_SIZE; j++)
            if (uncer[j][-(Y_MIN)][i]<1) fprintf(fp,"    *.**, ");
```

```
            else
                fprintf(fp, "%8.2lf, ",sens[j][-(Y_MIN)][i]/sqrt((double)(uncer[j]
[-(Y_MIN)][i])));
          fputc('\n', fp);
      }
      fclose(fp);
      fp = fopen("count","w");
      fprintf(fp,"Total number of photons = %d\n",N_PHOTONS);
      fprintf(fp,"Photons used for sensitivity data = %d\n", photon_sens_count);
      fprintf(fp,"Photons used in background spectrum = %d\n", photon_spect_count);
      fprintf(fp,"Kidney summed sensitivity = %le per incident photon\n",kid_sens_su
m/(double)(N_PHOTONS));
      fclose(fp);
      /* Free space declared for tables                                    */
      free_ivector(cspectrum, min_energy, max_energy);
      free_vector(s_pe_gold, min_energy, max_energy);
      free_vector(s_compton, min_energy, max_energy);
      free_vector(s_elastic, min_energy, max_energy);
      free_vector(s_photoel, min_energy, max_energy);
      free_vector(mean_path, min_energy, max_energy);
}
```

Appendix C

Glossary of Terms

AAS: Atomic Absorption Spectroscopy.

Agranulocytosis: A symptom complex characterised by a marked decrease in the number of granulocytes and by lesions of the throat and other mucous membranes, of the gastrointestinal tract, and of the skin.

Aplasia: Lack of development of an organ or tissue, or of the cellular products from an organ or tissue. (Adjective: **Aplastic**).

Arthritis: Inflammation of a joint.

Bacillus: A rod shaped bacterium.

Chromatin: The substance of chromosomes, the portion of the cell nucleus that stains with basic dyes.

Chrysiasis: Deposition of gold in living tissue.

Chrysotherapy: Gold therapy.

Cortex: An outer layer.

Cutaneous: Pertaining to the skin.

Cytoplasm: The protoplasm of a cell exclusive of that of the nucleus.

Dermatitis: Inflammation of the skin.

DL: Detection Limit.

Eosinophil: A granular leukocyte having a nucleus with two lobes connected by a thread of chromatin, and cytoplasm containing coarse round granules of uniform size.

Eosinophilia: The formation and accumulation of an abnormally large number of eosinophils in the blood.

Exfoliation: A falling off in scales or layers (Adjective: **Exfoliative**)

Granulocyte: Any cell containing granules. Especially a granular leukocyte.

Jaundice: A yellowness of the skin, scleras, mucous membranes and excretions due to deposition of bile pigments.

Leukocyte: A type of white blood cell.

Macrophage: Any of the large mononuclear cells derived from monocytes that occur in the walls of blood vessels and loose connective tissue.

MCA: Multi-Channel Analyzer

MDL: Minimum Detectable Limit. The minimum concentration that can be qualitatively detected.

Medulla: The innermost part.

Monocyte: A mononuclear leukocyte, 13μm to 25μm in diameter with an ovoid or kidney-shaped nucleus. Monocytes develop into macrophages.

NAA: Neutron Activation Analysis.

Nephropathy: Disease of the kidney.

Nephrosis: Any kidney disease. (Adjective: **Nephrotic**).

Nephrotoxic: Destructive to kidney cells.

NPL: National Physical Laboratory.

Nucleoplasm: The protoplasm of the nucleus of a cell.

Parenteral: Not through the alimentary canal, but rather by injection through

some other route, such as subcutaneously, intramuscularly, etc.

PIXE: Proton-Induced X-ray Emission analysis.

Proteinuria: An excess of serum proteins in the urine.

Protoplasm: Translucent colloid material, the essential constituent of the living cell, including cytoplasm and nucleoplasm.

Pruritus: Itching. (Adjective: **Pruritic**.)

RA: Rheumatoid Arthritis.

Renal: Pertaining to the kidney.

Rheumatism: Any of a variety of disorders marked by inflammation, degeneration, or metabolic derangement of connective tissue structures, especially the joints and related structures, and attended by pain, stiffness, or limitation of motion.

Rheumatoid: Resembling Rheumatism.

RNHRD: Royal National Hospital for Rheumatic Diseases.

RUH: Royal United Hospital.

Sclera: The tough white outer coating of the eyeball. (Adjective: **Scleral**.)

SIVARG: Swansea *In Vivo* Analysis Research group

Thrombocytopenia: Decrease in the number of platelets in circulating blood.

TLD: ThermoLuminescent Dosimeter/Dosimetry.

Tubercle: Any small rounded mass produced by infection with Mycobacterium tuberculosis. (Adjective: **Tubercular**).

XRF: X-ray Fluorescence.

Appendix D

Published Work

$^{99}Tc^{m}$ Radio-pharmaceuticals for the X-ray fluorescence assessment of gold *in vivo*

(Published in *Physics in Medicine and Biology* **36** Pages 531-536)

1. Introduction

The use of X-ray fluorescence (XRF) for the determination of heavy metals such as lead (Ahlgren and Mattsson, 1979; Somervaille *et al*, 1985; Price *et al*, 1984), cadmium (Ahlgren and Mattsson, 1981), platinum (Jonson *et al*, 1987), mercury (Bloch and Shapiro, 1981) and gold (Scott and Lillicrap, 1988) *in vivo* is now a fairly widespread technique. Radiation sources used to produce the characteristic fluorescence have included many radio-isotopes with low energy photons such as ^{109}Cd, $^{99}Tc^{m}$, ^{241}Am, ^{57}Co and ^{133}Xe and more recently both unpolarised and partially polarised X-ray sources.

The use of external radio-isotope sources has been very successful for the determination of metals in organs with little overlying tissue such as lead in tibia. However for organs at larger depths much higher skin doses and longer irradiation times are required for the same source activity. This has led to the use of X-ray sources which can be placed at some distance from the skin while maintaining a good photon flux, thus giving a larger absorbed dose to the organ of interest for a given skin dose. A greater sensitivity and uniformity of response is therefore achieved since the amount of fluorescence is approximately proportional to organ dose for a given radiation source.

There is, however, another possibility for organs lying at a depth, which is to use a radio-labelled pharmaceutical which is specific to the organ of interest, such as those used for imaging in nuclear medicine studies. One advantage of an internal source is that it should lead to a better uniformity of organ

irradiation than external sources, as it is distributed through the organ of interest. The questions to be considered are whether sufficient activity is present in the organ for a sufficient length of time to make a measurement, and whether the required measurement sensitivity can be achieved. The following work describes a feasibility study carried out to establish whether a $^{99}Tc^{m}$ radio-labelled pharmaceutical would be a suitable source for X-ray fluorescence studies of gold in the kidney.

There are very few quantitative data on the deposition of gold in body tissues during chrysotherapy to decide on a required measurement sensitivity. Gottlieb *et al* (1972) measured the gold concentration at autopsy in various organs from a patient who had received chrysotherapy. They found gold concentrations in the renal cortex between 120μg g^{-1} and 130μg g^{-1}. Thus to be useful for *in vivo* measurements a technique would need a detection limit below about 50μg g^{-1}.

2. Experimental Work

The experimental work was divided into two parts. Firstly, a measurement was made to establish the activity that would be required in the kidney of a patient to achieve acceptable detection levels. Secondly, typical kidney activities were estimated in patients who were undergoing nuclear medicine studies in order to assess whether sufficient activity was present for X-ray fluorescence studies.

The experimental arrangement for the first study is shown in figure 1. The detector was a high purity germanium detector, 10mm in diameter and 7mm thick with a resolution (FWHM) of 425eV at the ^{241}Am 60keV emission line. The kidney was represented by a 150ml, 45mm diameter, polythene bottle which contained a solution of chloroauric acid, with a concentration of gold of 500μg g^{-1}. This kidney phantom was placed in a water bath at various depths from the wall of the water bath to represent a range of kidney depths which may be found in practice. The detector collimator was placed against the wall of the water bath. A small (4.5ml) polythene tube containing approximately 20MBq of $^{99}Tc^{m}$ was placed down the centre of the kidney phantom to represent

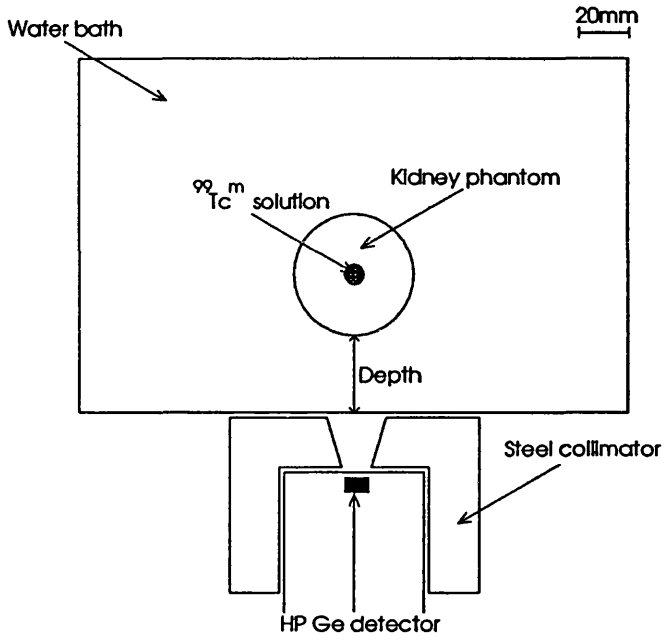

Figure 1 - Scale diagram of apparatus for HP Ge detector experiments

Scan Time / s	Activity / MBq	Kidney Phantom Depth / mm	Gold $K_{\alpha 1}$ Peak / Counts	MDL / $\mu g\ g^{-1}$	AAR[§] / MBq
2266	15.9	20	3860±212	55	2.7
1800	20.0	30	3305±201	61	3.3
2020	17.8	40	2481±182	73	4.7
2936	12.3	60	1516±153	100	8.9

[§] Anticipated Average Activity required for a MDL of 50$\mu g\ g^{-1}$ for a 32mm diameter HPGe detector
Table 1 - Summary of results using HP Ge detector

the kidney uptake of the radio-pharmaceutical. For an initial activity of 20MBq the resultant spectra were recorded over a period of 30 minutes, this represents the maximum acceptable time for patient studies. In practice the actual irradiation times were adjusted to compensate if the initial activity was different from 20MBq. The analysed results from this experiment are given in the first five columns of table 1 and a typical signal amplitude spectrum is shown in figure 2. The analysis was performed on a region of the recorded spectrum bracketing both the gold K_α peaks: this portion of the spectrum was fitted by an analytical function using a non-linear least squares fit based on the algorithm proposed by Marquadt (1963) and implemented by Press *et al* (1988).

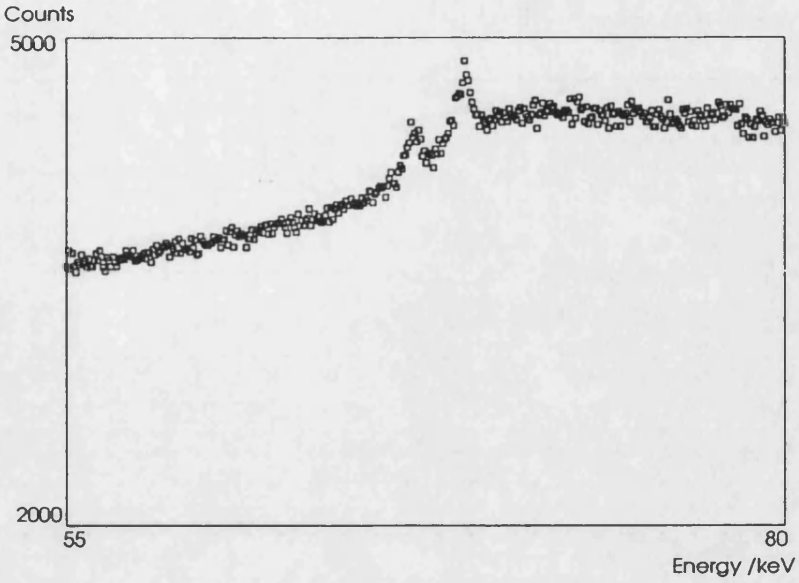

Figure 2 - Portion of the signal amplitude spectrum showing the gold K_α peaks for the 20mm depth result in table 1

With the 10mm diameter detector used minimum detectable levels (MDL) close to the target level of 50μg g^{-1} could only be achieved for kidney depths less than 30mm. The MDLs were determined to be approximately two standard deviations, as returned by the fitting program, above background.

It is possible to forecast the improvement in MDL from those achieved above if a larger diameter detector was used. The MDL will decrease approximately with the increase in the square root of the number of counts collected, due to the Poisson nature of the counting process involved. A number of predictions on how the target MDL of 50μg g^{-1} could be achieved can therefore be made. (A more rigorous discussion of the factors affecting the detection limit is given by Mattsson *et al* (1987)). If the size of the detector is increased, the number of counts collected in a given time increases with detector area and therefore the MDL decreases with increase in detector diameter. Therefore if a 32mm diameter detector were used the achievable MDL would decrease by approximately a factor of three and, from table 1, would lead to a MDL of about 30μg g^{-1} even at a kidney depth of 60mm with a measurement time of 30 minutes and 20MBq of $^{99}Tc^{m}$ in the kidney. Similarly the MDL would decrease approximately with increase in both the square root of activity found in the

kidney and with the square root of the scan time. If the maximum scan time is limited to 30 minutes but a detector of 32mm diameter is used, it is anticipated that the average activity that would be required (AAR) in the kidney under investigation to achieve a MDL of 50μg g^{-1} would be those given in the final column of table 1.

In order to establish the activity that is actually in the kidney of a patient at any one time during a nuclear medicine investigation, data from patients who had undergone investigation were re-examined. The activity found in the kidney is obviously dependent on the radio-labelled pharmaceutical used. Locally there are two $^{99}Tc^{m}$ labelled pharmaceuticals used in the nuclear medicine department for renal studies, these are diethylenetriamine penta-acetic acid (DTPA) and dimercapto succinic acid (DMSA). Maisey (1980) states that with DMSA the injected activity taken up in the renal parenchyma remains there indefinitely. However the activity variation of DTPA with time in the kidney for healthy kidneys is quite rapid. The count rate variation over the region of interest of one kidney with time could be extracted from all renogram (DTPA) studies and some DMSA studies performed locally. A selection of data from adult patients with apparently healthy kidneys is given in tables 2 (DTPA - renograms reported as normal) and 3 (DMSA imaging studies). The total activity initially administered to all these patients was 185MBq.

In order to relate these count rates to the activity of $^{99}Tc^{m}$ in the kidney, a polythene bottle identical to the one used as a phantom in the previous experiment was filled with a solution containing 20MBq of $^{99}Tc^{m}$. This was then placed in a water bath at various distances from the wall to assess the effect of kidney depth on count rate. A study was then made of this phantom using the gamma camera in the configuration used for renal studies. The count rate over the region of interest of the bottle was around 2100cs^{-1} when the surface of the bottle was 30mm from the wall of the water bath falling by 17% to 1750cs-1

Patient Number	Count Rate from ROI covering / cs^{-1}			
	Right Kidney		Left Kidney	
	5 mins[§]	40mins[§]	5 mins[§]	40mins[§]
1	450	220	500	240
2	810	200	570	150
3	1070	250	990	250
Average	780	220	690	210

[§] Time after injection

Table 2 - Results from patients undergoing DTPA studies

Patient Number	Count Rate from ROI covering / cs^{-1}	
	Left Kidney	Right Kidney
10	1330	1480
11	1520	1510
12	1525	1580
Average	1460	1520

Table 3 - Results from patients undergoing DMSA studies

when the depth was 60mm. The kidney depth was not recorded in the patient records. However from these results the uncertainty in the estimated activity because of this is not likely to exceed ±10% from the mean. Averaging the data in table 2 over apparently healthy kidneys of DTPA patients gives a count rate of $740cs^{-1}$ 5 minutes after injection falling to a rate of $220cs^{-1}$ 40 minutes after injection. Using the phantom data above these count rates are equivalent to 7-8½MBq of $^{99}Tc^{m}$ in the kidney 5 minutes after injection and 2-2½MBq of $^{99}Tc^{m}$ after 40 minutes for DTPA patients.

Averaging the data in table 3 over reportedly normal patients undergoing DMSA scans gives a count rate of $1490cs^{-1}$ over each kidney approximately 3 hours after injection. As previously stated the biological half-life of DMSA is much longer than the physical half-life and therefore the count rate variation with time is small. Allowing for the uncertainty in kidney depth this count rate is equivalent to 14-17MBq of $^{99}Tc^{m}$ in each kidney. Such activities are well above those that would be required (AAR - table 1) to reach detection levels of $50\mu g\ g^{-1}$ even for kidneys lying at a depth of 60mm. The proportion of injected DMSA reaching the patients kidneys in these studies is therefore

approximately 24%. Thus for a detection level of 50μg g^{-1} for kidneys lying at 60mm an injected activity of about 100MBq is required, much less than the 185 to 200MBq administered for imaging studies (Mistry, 1988).

3. Conclusions

From the above work it is concluded that intravenously administered $^{99}Tc^{m}$ radio-labelled pharmaceuticals would be suitable sources for XRF studies of gold in the kidney. The target MDL of 50μg g^{-1} would be achieved with a detector of sufficient area using significantly less than the activity administered to patients undergoing diagnostic renal studies. Of the two radio-pharmaceuticals in routine use locally for kidney studies, DMSA proved to be the better drug, as to obtain the same X-ray fluorescence yield higher activities of DTPA need to be administered. Although, with its rapid passage through the kidney, DTPA produces a lower kidney absorbed dose than DMSA, even with the higher initial activities required, this is more than offset by the greater absorbed dose given to the bladder wall (ICRP, 1988).

It is possible to compare the use of $^{99}Tc^{m}$ labelled DMSA with external sources for XRF studies with respect to the resulting absorbed dose estimations. With $^{99}Tc^{m}$ DMSA the kidney receives the highest absorbed dose whereas external sources deliver the highest dose to the skin. The absorbed doses will depend on the source to skin distance of external sources and on the kidney depth. For an external source, filtered ^{153}Gd has been used locally, positioned 40mm from the skin. For similar detection sensitivity (50μg g^{-1}), kidney depth (30mm) and detector diameter (32mm), the $^{99}Tc^{m}$ DMSA would deliver a kidney absorbed dose of 6mGy and a negligible skin dose (ICRP, 1988), whereas the external ^{153}Gd source would deliver 2mGy to the skin and an average kidney absorbed dose of about 0.3mGy. An X-ray source at a larger source to skin distance would reduce the skin dose further, but would be a more costly system.

Although the local interest of this work relates to the detection of gold in the kidney, similar conclusions may be drawn regarding the detection of other

heavy metals of interest such as platinum and lead which may be found in the kidney following medical or industrial exposure, although lower detection levels and high higher administered activities would probably be required.

4. Acknowledgements

J.S. is grateful for funding from the UK Medical Research Council (Grant number G78/0030). The help of all the staff in the nuclear medicine department at the Royal United Hospital, Bath is also gratefully acknowledged.

5. References

The references in this paper can be found in the main bibliography.

Appendix E

Volunteer Consent Form

Measurement Of Tissue Gold Levels In Chyrsotherapy Patients

The purpose of this study in which you are invited to participate is to measure the retention in the body of the gold that you have received / are receiving. The study should enable more information to be obtained which could be of benefit to those receiving this form of treatment in the future. Thus, the study is not likely to be of direct benefit to individual participants.

You will be asked to undergo two measurements. These will be carried out in the diagnostic centre and the Wolfson centre at the Royal United Hospital. The first of these will be a simple ultrasound scan to locate precisely the position of your kidneys and the second will be a measurement of the amount of gold in your kidney at a soft tissue site. For the gold measurement you will be exposed to a small quantity of radiation, about the amount associated with a conventional chest X-ray picture. Neither the X-ray nor the ultrasound measurement will produce sensations of discomfort.

I

of

confirm that I have had explained to me the nature of the study in which I now agree to participate and the explanations have been delivered to my satisfaction. I confirm that I have been advised of the possible adverse effects and have been given the opportunity to ask questions.

I understand that I am free to withdraw from the study at any time without the need to give reason and without prejudice to my treatment. I confirm that I am over 18 years of age. I give my consent to participate in the study here outlined and to abide by its provisions unless I should choose to withdraw before its completion. I agree that the results of my study may be used

anonymously for the purposes of the general investigation and the publication of its results.

Signed: Date: